Université de Paris

Ecole Doctorale 564 Physique en Île-de France
Laboratoire Matériaux et Phénomènes Quantiques

Electronic interaction of organic molecules with low dimensional materials: a scanning tunneling microscopy study on graphene and black phosphorus

Par Rishav Harsh

Thèse de doctorat de **Physique de la matiére condensée**

Dirigée par Jérôme Lagoute

Présentée et soutenue publiquement le **23-09-2019**

Devant un jury composé de:

Andrew Mayne, directeur de recherche, Institut des Sciences Moléculaires d'Orsay(ISMO), Rapporteur

Frank Palmino, professeur, Université de Franche-Comté, Rapporteur

Muriel Sicot, chargée de recherche, Institut Jean-Lamour, Examinatrice

Laurent Simon, directeur de recherche, Institut de Sciences des Matériaux de Mulhouse, Examinateur

Jérôme Lagoute, chargé de recherche, Laboratoire Matériaux et Phénomène Quantiques, directeur de thése

Except where otherwise noted, this is work licensed under
https://creativecommons.org/licenses/by-nc-nd/3.0/fr/

Abstract

Combining low dimensional materials with organic molecules offers promising opportunities to achieve new functionalities. Single molecule devices have received considerable attention in recent years due to the possibility of miniaturization down to nanometer regime. Two dimensional materials, and more importantly graphene, are very promising to achieve unprecedented physical properties. The molecules can be designed in terms of desired chemical properties and size while graphene can be modified, for example, by substitutional doping. This dual control of tuning the properties of host molecule and the substrate offers tremendous opportunities for applications while giving access to a variety of phenomena that can be observed at the nanoscale.

In this thesis, we study the interaction of organic molecules with multilayer graphene by means of scanning tunneling microscopy (STM) and spectroscopy at low temperature. We have studied both electron acceptor (F_4TCNQ) and donor type (porphyrin) molecules to understand charge transfer process and local band bending at the interface. In addition to graphene, we have also studied the surface properties of black phosphorus and its interaction with F_4TCNQ. The three main parts of the thesis deal with the interaction of molecules on graphene and black phosphorus.

In the first part, free base porphyrin (H_2TPP) is studied on pristine and nitrogen doped graphene that forms 2D lattice even at sub-monolayer concentrations. We have focused on the dynamics of proton exchange mechanism (hydrogen-tautomerization) inside the porphyrin inner core. The molecule can adopt two states depending on the position of the two inner hydrogen atoms, which are characterized by bright and dark contrasts in the STM topography image. The time dependent trace of the tunneling current recorded above a molecule reveal a reversible switching between the two states leading to a telegraph signal. The study of the current and bias voltage dependence of the switching frequency reveal that the excitation mechanism is a resonant excitation process, in contrast with inelastic process that have been reported for tautomerization on metallic substrates.

In the second part, the interaction of strong p-dopant F_4TCNQ molecules with pristine graphene and N-doped graphene is investigated. The organization of these molecules on pristine graphene is dictated by repulsive inter-molecular forces and weak substrate coupling. Depending on the surface concentration, they organize themselves as isolated, linear chains and double layer chains. The presence of a 2D monolayer has been observed in case of nitrogen doped graphene. Spectral features on the molecules show sharp charging/dis-charging peaks that change with respect to local environment.

In the last part, we study the surface properties of black phosphorus (BP) and the behavior of adsorbed F_4TCNQ molecules. As a basis for new 2D material, BP is explored for a range of electronic and optoelectronic applications which is why we first investigate the intrinsic properties of the material, in particular, the native defects present on the surface. Local spectroscopy techniques reveal that some of the defects can be manipulated to transform into more stable

types. While the defects don't interact with electron acceptor F_4TCNQ molecules, phosphorus atoms do provide a suitable adsorption site owing to a free lone pair of electrons. In this system, the molecules can be activated by a voltage pulse with the tip to change into a state that can diffuse on the substrate under the influence of the STM tip. With several unique features, the BP therefore offers a new playground for molecular electronics.

Keywords

Scanning tunneling microscopy and spectroscopy, graphene, black phosphorus, F4TCNQ, porphyrin, tautomerization, physisorption.

Résumé

La combinaison de matériaux de basses dimensions et de molécules organiques ouvre de nouvelles opportunités pour réaliser de nouvelles fonctionnalités. Les dispositifs moléculaires ont fait l'objet d'une attention particulière pour réaliser des composants de taille nanométrique. Les matériaux bidimensionnels, et le graphène en particulier, possèdent des propriétés physiques remarquables qui les rendent très prometteurs pour des applications dans divers domaines. Les molécules peuvent être conçues pour avoir les propriétés chimiques souhaitées, et les propriétés du graphène peuvent être modifiées par exemple par dopage substitutionnel. Ce double contrôle, des molécules, et des matériaux bidimensionnels, offre de formidables opportunités pour de nouvelles applications et donnent accès à une variété importante de phénomènes qui peuvent être observés à l'échelle nanométrique.

Dans cette thèse, nous avons étudié l'interaction de molécules organiques avec du graphène multicouche par microscopie à effet tunnel (STM) et spectroscopie à basse température. Nous avons étudié des molécules de type électroaccepteur (F4TCNQ) et électrodoneur (porphyrine). Nous avons également étudié les propriétés de surface du phosphore noir et son interaction avec les F4TCNQ. Les trois parties de la thèse traitent de l'interaction des molécules sur le graphène et le phosphore noir.

Dans la première partie, nous avons étudié des molécules de porphyrine (H2TPP) sur du graphène pur et dopé par de l'azote. Ces molécules forment un réseau 2D, même à des concentrations inférieures à la monocouche. Nous nous sommes concentrés sur la dynamique du mécanisme de migration des atomes d'hydrogène (tautomérisation) au centre de la molécule.

La porphyrine peut adopter deux états en fonction de la position des deux atomes d'hydrogène au centre de la molécule. Ces états sont caractérisés par des contrastes brillant ou sombre dans les images STM. L'évolution temporelle du courant tunnel enregistré au-dessus d'une molécule révèle un basculement réversible entre deux états conduisant à un signal de type bruit de télégraphe. L'étude de la dépendance de la fréquence d'excitation en fonction du courant et de la tension montre que le processus d'excitation est résonant, à la différence du processus inélastique décrit pour la tautomérisation sur des substrats métalliques.

Dans la seconde partie, l'interaction de molécules F4TCNQ de type accepteur avec le graphène pur et le graphène dopé par de l'azote a été étudiée. L'organisation de ces molécules sur du graphène pur est influencée par des forces répulsives inter-moléculaires et un couplage faible avec le substrat de graphène. En fonction de la concentration de molécules, elles s'organisent en chaînes isolées, linéaires et en double couche. La présence d'une monocouche 2D a été observée dans le cas du graphène dopé à l'azote. Les caractéristiques spectrales sur les molécules montrent des pics de charge / décharge qui changent en fonction de l'environnement local.

Dans la dernière partie, nous avons étudié les propriétés de surface du phosphore noir (BP) et le comportement des molécules F4TCNQ adsorbées. Le BP est étudié depuis quelques années comme nouveau matériau 2D pour des applications dans divers domaines comme l'électroniques

et l'optoélectronique. Nous avons d'abord étudié les propriétés intrinsèques du matériau, en particulier les défauts originellement présents à la surface. Les mesures de spectroscopie montrent que certains défauts peuvent être manipulés pour évoluer vers un type de défaut plus stable. Bien que les défauts n'interagissent pas avec les molécules F4TCNQ, les atomes de phosphore constituent un site d'adsorption approprié grâce à une paire d'électrons célibataires. Dans ce système, les molécules peuvent être activées par une impulsion de tension avec la pointe pour passer dans un état pouvant diffuser sur le substrat sous l'influence de la pointe du STM. Avec plusieurs caractéristiques uniques, le BP offre donc un nouveau substrat prometteur pour l'électronique moléculaire.

Mots clefs

Microscopie et spectroscopie à effet tunnel, graphène, phosphore noir, F4TCNQ, porphyrine, tautomérisation, physisorption.

Acknowledgements

I am thankful to my team members, colleagues, teachers and friends who have guided me from the beginning, and seen it to the end. First and foremost, I would like to offer my sincere gratitude to Prof. Shobhana Narasimhan for her recommendation to this PhD project, and the scholarship that followed. I am indebted to Indo-French Centre for the Promotion of Advanced esearch (IFCPAR) / Centre Franco-Indien pour la Promotion de la Recherche Avancée (CEFIPRA) for the scholarship and travel support during the project duration.

I have been really fortunate to have Jerome as my thesis supervisor, throughout my PhD he has been a patient teacher, mentor and a friend to me. I believe much of my personal and professional growth has happened because of the nurturing environment and encouraging nature of all the team members of *Equipe STM*. I am really grateful for their timely input and valuable suggestions. They have been vital to my PhD life as well as external to lab also, in particular, help with the french bureaucracy and french language. Special thanks to Cyrille in this direction and also for being a constant troubleshooter of my experiments (and others as well).

I extend my gratitude to some of the most efficient persons of Paris Diderot, Anne, Jocelyn, Sandrine and Nathalie. Time has been well spent with fruitful discussions, jokes and some interesting conversation with my colleagues in the office: Stephen, Allegra, Dong, Simon, Zahra, Tong, Azzurra and Alireza. My work-life balance has stayed well, thanks to the pack of international friends in Paris. I have been lucky to experience their company while making some lifelong friendships. With no particular order, they are Muazzam, Mircea, Carlotta, Sophie, Laura, Julie, Ahil, Nicolas, Salma, Ramona, Lavinia, Cristina, Gabriel, Elena, Nishit, Hong-Ming, Alessandra, Nasoloniaina, Ridhima, Mannel, Qing, Yara, Hela, Aicha, Ouafi, Asif and Asad.

Living in Paris has been a learning experience and would remain an unforgettable memory. I feel lucky to have taken the decision to come to Paris, to immerse in its rich culture, heritage, architecture and cuisine. Thank you Campus France for the CROUS accommodation in one of the beautiful neighborhoods with a stunning view. Due to some nice people, this city has felt like a home and I am grateful that you welcome me in your lives. Thank you Patrizia and Matteo.

The works described in this thesis has been an outcome of several collaborations. Thank you Dr Woei Wei Pai (Larry) for introducing me to the world of black phosphorus and for your hospitality during our Taipei visits. Thank you Yannick Dappe and Alexander Smogunov for running those tedious calculations on molecules. Once again, I would like to thank Shobhana and her team at JNCASR, Sukanya, Rajdeep and Sourav for performing calculations on several projects. Thank you Prof. Enrique Ortega for allowing me to join your team for Synchrotron experiments at SOLEIL. And also for sponsoring my visits to University of Basque Country at San Sebastien. Finally, thanks to my collaborators from university, Philippe Lang and Mahamadou Seydou.

It gives me immense pleasure to fulfill the expectations of my loving ones who have constantly supported me in all my endeavours and I am thankful to them for believing in me.

Contents

1 Introduction **1**
- 1.1 Interest in 2D materials . . . 1
- 1.2 Molecular thin films . . . 5
  - 1.2.1 Interfaces . . . 5
  - 1.2.2 Molecules on vdW materials . . . 7
- 1.3 Introduction to studied materials . . . 9
  - 1.3.1 Black Phosphorus . . . 13
- 1.4 Thesis Outlook . . . 17
- 1.5 Plan of the thesis . . . 17

2 Experimental Methods **19**
- 2.1 Principle of STM . . . 20
  - 2.1.1 Theoretical background . . . 20
  - 2.1.2 Scanning Tunneling Microscopy and Spectroscopy . . . 25
- 2.2 STM instrument setup . . . 27
- 2.3 Methods . . . 28
  - 2.3.1 STM tip preparation . . . 28
  - 2.3.2 Sample preparation . . . 31

3 Dynamics of proton-transfer in free base porphyrin **35**
- 3.1 Porphyrin on pristine graphene . . . 36
- 3.2 Porphyrin on N-doped graphene . . . 45
- 3.3 Control of the tautomerization process . . . 50
  - 3.3.1 Tautomers as molecular switch . . . 50
- 3.4 Conclusions . . . 52

4 Interaction of electron acceptor F4-TCNQ molecules with Graphene **55**
- 4.1 Isolated molecules at low concentration . . . 56
  - 4.1.1 On pristine graphene substrate . . . 56
  - 4.1.2 On nitrogen-doped graphene . . . 63
- 4.2 Organization and inter-molecular interaction . . . 66
  - 4.2.1 1D growth . . . 66
  - 4.2.2 Moiré influence on molecular stacking . . . 68
  - 4.2.3 Electronic structure of molecular chains . . . 72
- 4.3 Conclusion . . . 76

5 Surface studies on Black Phosphorus **79**
5.1 Introduction 80
5.2 Structural and electronic properties of pristine black phosphorus 80
5.2.1 Pristine Surface 80
5.3 Native defects 83
5.4 Manipulation of point defects 89
5.5 Air induced changes 91
5.6 F4TCNQ on Black phosphorus 94
5.6.1 Activated molecules 96
5.6.2 Dynamics of charged molecules 98
5.7 Conclusion 101

6 Conclusion **103**

Bibliography **107**

Chapter 1

Introduction

1.1 Interest in 2D materials

Theoretical discussions on graphite layer was put forward by P. R. Wallace in 1947,[1] which describes the electronic structure of the carbon atoms in hexagonal lattice arrangement. It took more than 50 years and a scotch-tape to successively exfoliate atomically thin sheets of graphite, popularly known as graphene.[2] Contrary to the contemporary belief, this 2D crystal was thermodynamically stable with a strong in-plane tensile strength that rivaled steel, among other extraordinary properties. The significance of this discovery was immediately recognized by the scientific community, earning Geim and Novoselov the Nobel Prize in Physics for 2010.

Having a thickness of just one carbon atom, graphene can be considered as a strictly two-dimensional (2D) material.[3] In the last decade, there have been several additions to the 2D family and the repertoire continues to grow.[4] The field of 2D materials is intriguing as the physical and chemical properties change drastically going from the bulk form to the single layer.[5,6] For example, in graphene, the electronic dispersion of states is linear near the Fermi level and the electrons behave as massless dirac Fermions. These unique properties are absent in graphite.

Layered 2D materials can be obtained from the parent bulk crystal by mechanical cleaving such as the scotch-tape method. The ease of extracting single layer comes from the fact that the constituent layers are bonded by weak van der Waals type interaction thus preserving the in-plane structural integrity during the cleaving process. For this reason they are also referred to as van der waals layered materials. In this family, single layer transition metal dichalcogenides (TMDs) are the most popular after graphene.[7] Most of them are semiconducting in nature with an indirect band gap while an optically active band gap exists just in the limit of a monolayer.[8] The field of TMDs itself has grown into a separate domain of research with particular focus on optoelectronic and transistor applications.[9]

Most recent and popular addition to van der waals materials family is phosphorene which is

Name	Element/s	Bonding / Lone pair	Electronic Character
Graphene[2]	C	sp^2 / one (p_z)	semi-metallic, gapless
h-BN[16,25]	B, N	sp^2 / one (p orbital on N)	insulating
Phosphorene[26]	P	sp^3 / one (sp^3)	semiconductor, optically active
(Chalcogens)	S, Se, Te	polar (-2) / two	
(Metals)	Ti, Hf, Zr	polar (+4)	Semiconducting. Diamagnetic.
	V, Nb, Ta	"	Semimetallic. Superconducting. Charge density wave. Paramagnetic, anti-ferromagnetic, or diamagnetic.
TMDs[27,28]	Mo, W	"	Semiconducting (S, Se). Semimetallic (Te). Diamganetic.
	Tc, Re	"	Semiconducting. Diamagnetic
	Pd, Pt	"	Semiconducting (S, Se). Diamagnetic. Metallic, Paramagnetic (Te). Superconducting ($PdTe_2$)

Table 1.1: Electronic properties of some van der Waals materials

obtained from black phosphorus and has even been referred to as "new graphene".[10] Black phosphorus is a semiconductor with optically active band gap of around 0.3 eV which increases monotonically with decreasing number of layers,[11] and predicted to have an energy gap of around 2.0 eV for its monolayer derivative. Other 2D materials that are actively studied include borophene,[12] germanene,[13] stanene,[14] silicene,[15] hexagonal boron nitride (h-BN),[16] graphitic carbon nitride (g-C_3N_4),[17] layered metal oxides,[18] 2D-Metal organic frameworks (MOFs),[19] covalent organic frameworks (COFs),[20] etc.[21] The library of 2D materials now almost spans over half of the periodic table, including theoretical predictions for several elements and compounds that can be stable in single or fewl layer phase.[6,22–24]

As a single layer, 2D materials can be used as substitutes for thin film version of the bulk materials to keep the same functionality. As an insulator, h-BN can be used on semiconducting substrates like n-doped silicon or MoS2 where it can function as a dielectric due to its wide band gap of 6 eV.[29] Conventionally, thin films of silicon oxide, and other materials such as aluminium oxide or hafnium oxide, are grown on top of doped silicon wafers for making an insulating layer in transistor devices. Further, they also work as an excellent encapsulating material to improve performance. Among many other applications, graphene shows promising results as a transparent conducting material in gas sensors, photovoltaic devices, etc.[30] Thin films of indium tin oxide (ITO) are conventionally used as transparent conductive coatings but are costly due to limited availability of indium. Graphene on the other hand is very cheap and serves the same functionality with competing optical transparency or transmittance.[31] With h-BN or graphene, one needs to just transfer a single (or few) layer of the material onto the supporting substrate, thereby reducing the complexity in the fabrication process while keeping

the same functionality.

At this point, we make an important distinction between different types of 2D materials. It is to be noted that not all 2D materials are van der Waals type and thus cannot be extracted by micro-mechanical cleavage. In other words, these materials do not have a naturally occurring solid crystal from which individual layers can be obtained. Typically, they are epitaxially grown on substrates with matching lattice parameters, for example boronene, germanene, silicence and stanene. In some cases, they are also difficult to transfer to other substrates owing to buckling of atomic arrangement in the absence of matching substrate, like borophene.[12] In this thesis, we focus on the category of van der Waals (vdW) type 2D materials for their versatility and ease in utility with different substrates.

While continuous efforts are being invested in the growth, characterization, and application of 2D materials, there is a parallel research domain dedicated towards the design of stacked vdW/2D materials. A concise review on this topic is presented by Geim et. al. that details the fundamental concepts, advancements and perspectives on vdW heterostructures.[32] As heterostructures, they have been successfully implemented in different device configurations, such as PN junctions,[33,34] schottky diodes,[35,36] tunnel diodes,[37,38] field effect transistors,[39–41] photovoltaic devices,[42] light emitting devices,[33,43–45] detectors,[46,47] electrocatalysts,[48] chemical and biological sensors,[49,50] etc.

Stacked vdW heterostructures comprise of layers that act as the bulk as well as the interface. Due to their large surface-volume ratio, 2D materials have an entire plane of atoms (on either side) at their disposal for physical and chemical interaction. Weak van der Waals forces hold the layers in heterostructures but do little to modify the intrinsic properties of individual layers. The heterostructures are well suited to study and engineer interface properties. However, it is often desirable to tune the electronic, optical and mechanical properties of the materials themselves, to broaden their range of application and improve functionality. There are different methods to modify the intrinsic properties of 2D materials that can be broadly summarized (but not limited to) in the following categories:

- Doping of the 2D crystal by substitution.
- Chemical modification or derivatives.
- Surface adsorption of molecules, or molecular functionalization.

Substitutional doping is, as the name suggests, substitution of parent atom with some foreign elements (dopants) in the 2D lattice. This methods has been widely used to modify electronic and/or transport properties of graphene. The Fermi level and band gap of graphene can be tuned by use of dopants such as B, N, or Si.[51–54] Similarly, the electronic and optoelectronic properties

of Phosphorene doped with cationic (Li, Na) and anionic dopants (O, S) is predicted to tune it's electronic and optoelectronic properties.[55] In the TMD family, both metal and chalcogen atoms can be substituted to tune exciton binding energies.[56]

2D materials with available π bonds or lone pair of electrons can be used to produce derivatives by the addition of certain elements which also changes the hybridisation of the parent element. Once again, graphene provides an excellent example for this transformation. The sp^2 bonded carbon atoms upon hydrogenation or flourination (halogenation) produce sp^3 hybridized *graphane*[57] and fluorographene,[58,59] respectively. Phosphorene derivatives obtained by the addition of O, S, and N atoms, in a controlled manner, are predicted to improve it's photocatalytic properties.[60]

Molecular functionalization are used for the modification and tuning of the electronic structure by means of charge transfer with the 2D substrate.[61] The interaction between molecule and substrate can be non-covalent in the case of physisorption. Molecular bonding in the case of chemisorption (formation of covalent bonds) is excluded here since this would be similar to derivatives of the 2D material. In case of physisorption, the molecules are weakly bound in such a way that the hybridization of 2D substrate doesn't change. This method offers great flexibility in modifying the substrate properties since we have a huge library of compounds to our disposal and can be chosen accordingly to meet specific requirements or functionalities. Further, one can progress with synthetic chemistry methods to improve for a specific molecule-substrate system.

Above mentioned methods have their advantages and disadvantages, and can be employed depending on the requirement. The first two procedures, substitutional doping and chemical modification, irreversibly modify the 2D lattice structure as well as the intrinsic electronic properties.[(a)]Further, the options are limited with the choice of heteroatoms/compounds that can be used. On the other hand, non-covalent molecular functionalization keeps the 2D crytal structure without drastically modifying the electronic structure. The non-covalent interaction at substrate-molecule interface has effect on both graphene and the molecule entities. The 2D layer can be doped due to charge transfer with molecules and the energy level of molecular orbitals shift depending on the nature and strength of interaction. The study of molecule and the substrate in this case are complementary to each other.

In this thesis, we study interaction of molecules with vdW materials by means of scanning tunneling microscopy and spectroscopy. Here the actual interface is inaccessible to the local probe and much of the information is obtained by tunneling spectroscopy on the adsorbed molecules, in an indirect manner. In the next section, the topic of molecule-substrate interaction is presented in more detail including some STM related studies.

[(a)] Here, graphane is a special case where the graphene hydrogenation is reversible[57]

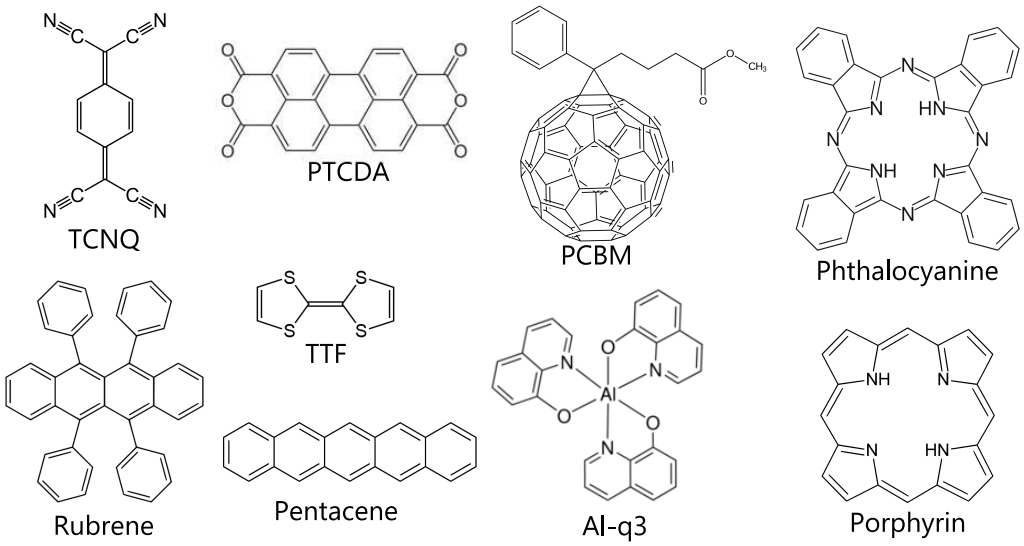

Figure 1.1: Semiconducting organic molecules

1.2 Molecular thin films

In the category of 2D or quasi-2D functional materials, thin film devices made from solution processed semiconducting polymers/molecules were the first to demonstrate feasibility for practical applications. Interest in organic semiconductor based devices gained popularity strating from mid- 80s with the fabrication of thin film organic solar cells (1986),[62] field effect transistors (1987)[63] and light emitting diodes (1990).[64] Since then there has been tremendous growth in the field of molecular electronics with commercially available products that use this technology.

Both single molecules as well as polymers can be used as active semiconducting material for electronics and optoelectronics applications. There exists a vast library of organic molecules that have been used for solar cells, transistor, LEDs, sensing and several other applications. Some of the most common and widely studied molecules are shown in fig-1.1. In this figure, most of the molecules have their derivatives that improve on existing properties to meet specific requirements.

1.2.1 Interfaces

Molecular thin films when used in a device structure form different kinds of interface with adjacent layers. To get a perspective on this aspect, typical schematic of common devices based on organic materials such as FETs, Solar cells and LEDs are shown in fig-1.2. In these devices, the active material (molecules or polymers) form interface with surfaces having different electronic properties. For example, in an OFET structure (1.2a) molecule-metal interface (organic : metallic) is formed for the source-drain contacts. On the dielectric side, use of oxides

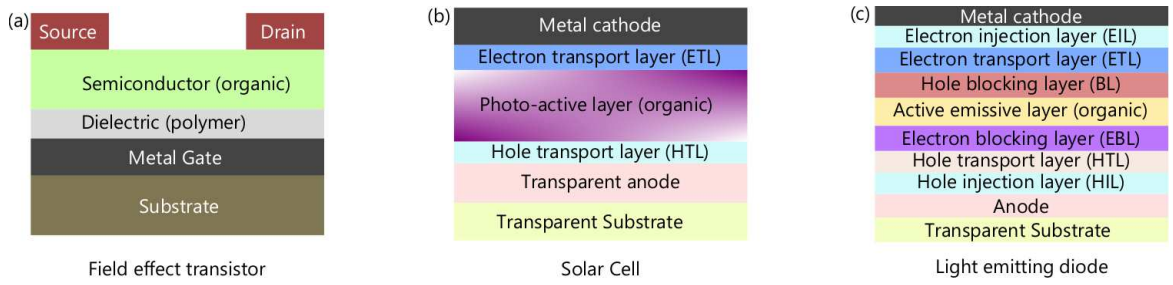

Figure 1.2: Schematic of common organic thin film devices

such as SiO2, Al2O3, HfO2 are very common whereas in an all organic thin film transistor, polymer dielectrics such BCB, PVDF are used frequently. Thus, we have a molecule-oxide (organic : insulating-inorganic) as well as molecule-polymer (organic : insulating-organic) interfaces for FET devices. The classification for interface here is kept simple and identified as organic, inorganic and metallic, in a broader sense.

With more complex device configurations such as solar cells (1.2b) and LEDs (1.2c), this classification becomes increasingly difficult. For example, in the OLED structure (organic LED), we find electron and hole blocking layers (EBL/HBL) on either of the active emissive layer. These are functional names that are defined on the basis of misalignment of molecular HOMO-LUMO levels with the conduction or valence band edge. Similarly, electron or hole transport layer (ETL/HTL) are used for thin films that are aligned with HOMO -LUMO levels.

From this discussion, we get an idea of the complexity involved in the interface physics with molecular films or even single molecules. The final position of molecular levels as well as the nature of interaction is required for tuning of electronic properties. It is well known that molecular frontier orbitals are modified after coming in contact with a surface. The degree of shift, broadening, lift of degeneracy, modification depends on the nature of interaction and charge transfer which can form dipoles at the interface or induce gap states near the Fermi level. The conventional description of band bending used for inorganic solids fails to describe energy level alignment for molecular interface. A complete understanding of the interface physics related with organic semiconductors is still an active field of research.

In this direction, various studies related to molecular thin films have been performed on insulating and metallic substrates. The properties of the interface or molecular layer can be probed by photoemission techniques such ultraviolet photoemission spectroscopy (UPS), X-ray photoemission spectroscopy (XPS), Inverse photoemission spectroscopy (IPES) and angle resolved photoemission spectroscopy (ARPES), two-photon photoemission (2PPE), and near-edge X-ray absorption fine structure (NEXAFS). These techniques provide averaged data over large ensembles of molecules. On a local level, scanning probe technique such as scanning tunneling

microscopy/spectroscopy (STM/S) and conductive atomic force microscopy (C-AFM) are quite useful which provide information with sub-molecular resolution.

STS on single molecular layers has produced good results in agreement with UPS/IPES measurements.[65] The benefit of using STM/S is that one obtains spatial electronic mapping with submolecular resolution. We focus on STM based studies on molecules which help understand the molecule properties and the underlying interaction with the substrate.

1.2.2 Molecules on vdW materials

STM on molecules

The first ever molecule to be imaged by high resolution STM was benzene in 1988, and co-adsorbed with carbon monoxide (CO) on Rh(111) surface.[66] In the following year, the first STM observation to reveal *internal structure* of an isolated molecule was performed on copper phthalocyanine (CuPc) adsorbed on Cu (100) surface.[67] Apart from metallic substrate, CuPc has been widely studied on semiconducting substrates such GaAs(110)[68] and Si(111).[69] Several other molecules were also studied. Initally, most of STM studies on molecules were performed on metallic or semiconducting surfaces.[70,71] This series of experiments followed until the end of 20th century. Later on, it was realized that the electronic structure of the molecule is strongly perturbed due to the presence of substrate electrons and prohibts to observe the unperturbed nature of molecules. In 2005, Jascha Repp et. al. worked around this problem by depositing few layers of NaCl on copper surface to image pentacene molecules.[72] Ultrathin film of insulating NaCl allowed observable tunneling of electrons through molecular orbitals on copper surface, while electronically decoupling it at the same time. With insulating layers, high resolution topography images for HOMO and LUMO orbitals of single molecules were recorded for the first time.

With progress in STM technologies, it is possible to obtain sub-atomic resolution and manipulate atoms/molecules with the tip. In the last decade, our understanding of single molecules/ films has advanced significantly. However, much of the attention has been dedicated towards the understanding of electronic structure of molecules on metallic and insulating surfaces. Concerning 2D or vdW materials, there are very few STM studies with molecules on them, including parent crystal such as HOPG or MoS2 for substrate.

We already see the trend these days where vdW materials are replacing their inorganic thin film counterpart. Graphene is being used as conducting and transparent electrode, which can function as contact electrodes and also substitute ITO in organic solar cells. For dielectric or insulating layer, h-BN has proved quite effective and very often used in transistor configuration. Further, h-BN can also be used as an encapsulation layer. MoS2 and black phosphorus are

optically active semiconductors that are being developed for opto-electronics. Combined with various functionality of semi-conducting molecules, functionalized vdW materials holds great potential for nanotechnology and also provides an accessible playground for quantum physics.

Case of van der Waals materials

Most popular and commonly studied vdW materials have been shown in the table-1.1. Graphene, MoS2, h-BN and Black Phosphorus show promising results for non-covalent functionalization. For this thesis, we have chosen graphene (semimetallic behavior)and black phosphorus (semiconducting behavior) as model substrates for molecular studies while also investigating the electronic properties of the substrate.

Graphene

In terms of molecular studies on graphene, some of the commonly used molecules are phthalocyanine, PTCDA,[73] PTCDI,[74] fullerene (C_{60})[75] and TCNQ[76](structure shown in fig-1.1). Each of these molecules are well studied organic semiconductors and used in thin film devices. These molecules are made of one or aromatic rings with delocalised π electrons, largely having a planar sp^2 bonded structure. This provides optimal configuration for molecules to have efficient $\pi - \pi$ interaction with underlying graphene substrate.

With increasing interest towards molecules on 2D materials, the properties of semiconducting molecules have been studied actively on metals, graphene and h-BN, in the last decade. Combined measurements of photoemission techniques and STM reveal common trends of the molecule-substrate interaction. In the case of graphene, it has been observed that the substrate beneath plays an important role on the molecule-graphene interaction. Typically, graphene substrate that are used for STM experiments are (1) epitaxial graphene grown in SiC(0001), (2) epitaxial graphene on metals such as Ir(111) and Rh(111), (3) vdW heterostructure of Gr/ h-BN, and (4) HOPG. The physisorbed molecules exhibit different structural and electronic properties depending on the substrate beneath graphene. These differences can be understood from the following examples-

- **PTCDA:** On bilayer graphene (BLG) / SiC(0001), molecules arrange in 2D herringbone structure while on HOPG, a "brickwall" arrangement is found.[77]
- **F4-TCNQ:** On single layer graphene (SLG) epitaxially grown on Ir(111), single molecules adsorb only on the *fcc sites* of the Gr/Ir moiré showing some charging behavior.[78] On the other hand, 2D molecular islands are formed on graphene/h-BN surface.[79]

The intrinsic properties of molecules are well observed on insulating surfaces when electronically decoupled whereas metallic surfaces interact very strongly with molecules. Also, it is

desired to avoid the strong moiré effects of graphene on metals. For these reasons, we choose a multilayer graphene substrate for studying electronic and structural behavior of physisorbed molecules. Further, we compare the results on pristine and nitrogen-doped graphene as well in order to better understand molecule-substrate interactions.

We have chosen two organic molecules to investigate the interface properties of functionalized graphene. The first one is a free base derivative of porphine called tetraphenyl porphyrin (H_2TPP) and acts an electron donor with respect to graphene. The second molecule is a fluorinated derivative of a strong electron acceptor TCNQ, called F_4TCNQ.

Black Phosphorus

For black phosphorus, studies with non-covalent functionalisation are very few. We find one study on wet chemical treatment of BP with perylene bisimides (PDI) and TCNQ where the charge transfer is observed through combined UV/Vis, FTIR and raman spectroscopy measurements.[80] Using combined photoemission techniques and DFT calculations, PTCDA-BP,[81] CuPC-BP,[82] C60-BP interfaces[83] and very recently, F16CuPc-BP[84] have been studied. We also find some theoretical work with physisorbed molecules on BP, *He et. al* have compared the charge transfer doping of BP with F4TCNQ, NO2 and MoO3 molecules using DFT and green function's approach.[85] A STM based measurement for molecules on BP has not been reported so far, i.e to the best of our knowledge, and we make progress in this direction. With some insight on molecular functionalization on BP from the literature, we study electronic properties of F4TCNQ on BP using STM and STS.

In the following sections, a short introduction on the materials such as H_2TPP, F_4TCNQ and black phosphorus is presented.

1.3 Introduction to studied materials

Tetra phenyl porphyrin (H_2TPP)

Chemical structure

Tetraphenyl porphyrin is an aromatic macrocyclic compound which is formed of four pyrrole groups linked by four methine (=CH–) bridge groups. This compound is a phenyl derivative of family of porphyrin compounds where porphine is the parent member comprising of just the macrocycle. The chemical structure of porphine and its derivatives are shown in figure-1.3(a). The porphine macrocycle is aromatic following Huckel's rule (4n+2) with n=4 comprising of 18π conjugated electrons. It is to be noted that there are 22 π electrons in the macrocycle but only 18 are delocalized. The conjugation can be observed in fig-1.3(a) with a blue outline on the chemical structure. The derivatives of porphine are obtained by following methods-

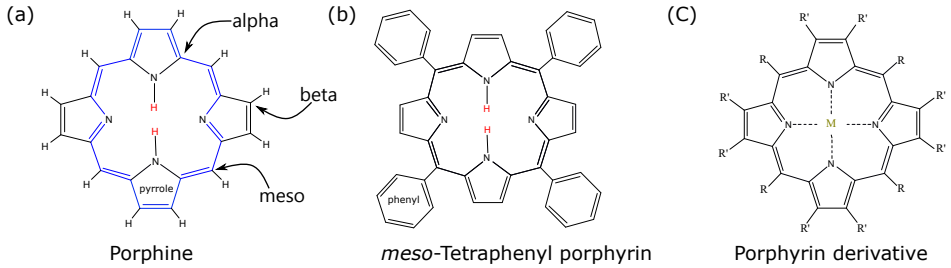

Figure 1.3: Porphyrin: (a) Parent member also known as porphine (b) Free base or hydrogenated derivative with four phenyl groups

1. metallation of the tetradentate core, usually with transition metal ions.

2. substitution at α, β and *meso*- positions (as shown in 1.3a)

A generic representation of a porphine derivative is shown in fig-1.3(c) where 'M' is any metal atom. Tetraphenyl porphyrin or meso-substituted tetra phenyl porphine (fig-1.3b), here, is the free base form with no metal ions in the inner core.

Several porphyrin derivatives are found in nature that serve important biological functions. A derivative of iron-porphyrin serves a very important function in the human biochemistry, in the form of *haem* which is the non-protein part of *haemoglobin*. The magnesium derivative forms the chlorophyll in plants which is responsible for light harvesting and also acts as charge separation system.[86] It can be aptly said that life wouldn't exist on Earth without the support of porphyrin compounds. Inspired from nature, porphyrins have witnessed their participation in a wide range of applications in various fields such as photovoltaics, artifcial photosynthesis, photodynamic therapy, sensors, catalysis, and enzymatic systems.[87,88] It is widely studied for its potential use in molecular electronics devices.[89,90]

Tautomerization in porphyrin compounds

Free base porphyrins exhibit a form of isomerism which is related to the position of hydrogen-atoms in the macrocycle.[91] These isomers which differ due to relative position of atoms in chemical structure, are identified as tautomers. Tautomerism proceeds because π electrons can reorganize in the chemical backbone. In porphyrin, 4 localized π electrons are available to assist with this process. The two H-atoms in free base tetraphenyl porphyrin (here onwards porphyrin) can switch to adjacent pyrrole groups attaching with nitrogen atom giving two tautomer forms. Quite similar to porphines is the phthalocyanine (Pc) family which is obtained by replacing the mething bridge group with nitrogen atom. Phthalocyanines have also been observed to show this form of isomerism.

Molecule	Substrate	References	Mechanism
Phthalocyanine (H_2Pc)	NaCl (bilayer)/Cu(111)	[93]	inelastic
H_2Pc	Ag(111)	[95–97]	inelastic
H_2Pc (theory)	NaCl (bilayer)	[98]	inelastic
CuPc	Cu(111)	[99]	inelastic
FePc / MnPc	Bi_2Te_3 / Sb_2Te_3	[100]	inelastic
Porphycene	Cu(111)	[101–105]	inelastic
Porphycene	Cu(110)	[106–108]	inelastic

Table 1.2: Summary of STM based studies on tautomerism in single molecules

In STM experiments, the tautomers can be distinguished by change in the conductance[92] or a rotation in the orbital shape of the molecule.[93] A concept of molecular switch has been proposed based on distinct conductance states of free base porphyrin molecule related to different tautomeric states.[94]

Associated changes in conductance can be understood by examining the atomic configuration of the two tautomers.

The molecular geometry of porphyrin deviates from a strictly planar arrangement and has been shown to adopt a saddle type configuration on Au(111) surface.[[109]] In this work, the molecular conformation has been explained on the basis of relative orientation of the pyrrole groups. The adjacent pyrroles are found to have a twist of around 60∘ between the plane of the five membered ring. With reference to the Au substrate, the C—C bond of two pyrrole groups are identified to be pointing away (α pyr.) from the surface, and the C—C bond of other two pyrroles being closer (κ pyr.)to the surface. In a 3D cartesian cordinate system, if the molecule lies in the $x-y$ plane and the Au surface extends from $z=0$ to $z=-\infty$ then α pyr. would point towards $+z$ direction while κ pyr. would point in the $-z$ direction. Correspondingly, the hydrogen atoms attached to α pyrrole, are referred as H_α and those attached to κ pyr. as H_κ. The switching of H-atoms from H_α to H_κ position is the underlying process of tautomerization here.

The apparent shape of H_2TPP molecule, as observed in STM, are different for two tautomers due to differences in the local density of state following the change in position of H-atoms in the cavity. The tautomers can be switched into one other by applying a voltage pulse with the STM tip. Such kind of manipulation on single molecules have been explored on similar systems as well. Few examples of tautomerization in single molecules as observed and manipulated with STM tip (or temperature, light, etc) is presented in the table -1.2

At low temperatures, the tautomeric conversion, which can be understood in terms of a chemical reaction, is thermally restricted due to comparatively large difference in the total en-

ergy of the intermediate and ground states of molecule. In case of tip induced tautomerization, the activation energy is provided by the tunneling electrons which can overcome the activation barrier. For the studies mentioned in the table, it has been found that the electrons exchange energy inelastically with the vibrational states of the molecule in order to switch the tautomers. With inelastic coupling, a low bias voltage provides sufficient energy to couple with the vibrational modes of the molecule which is typically of the order of few hundred milli-Volts (meV for energy). The other mechanism for excitation is the elastic coupling of electrons that occurs only at resonant conditions. However, there has not been any experiment that identifies elastic tunneling of electrons to be responsible for tautomerization, irrespective of the substrate used in the experiment.

We study tautomerization process in porphyrin to investigate the switching mechanism on pristine and N-doped graphene.

Electron acceptor F_4TCNQ

F_4TCNQ is a fluorinated derivative of TCNQ (7,7,8,8-tetracyanoquinodimethane). The TCNQ is well studied electron acceptor molecule[110] displaying a variety of properties such as metal–insulator transition,[111] Peierls metal–insulator transition,[112] etc. TCNQ and its derivatives are known to form organic charge transfer salts when combined with electron acceptor molecules due to their strong electrophilic nature.[110,113,114] The chemical structure of the molecule can be seen in fig-1.4(a) along with calculated orbital shape for HOMO and LUMO. Having a deep LUMO level of 5.2 eV, significant amount of charge transfer is expected with low work function materials such as graphene, energy level comparison for separated molecule and graphene is visualized in fig-1.4(b).

F_4TCNQ effectively dopes epitaxial graphene through electron transfer at the interface, as demonstrated through ARPES measurements.[115] It is also predicted to open a band gap in graphene through non-covalent interaction.[116] From DFT calculations, it can be seen that F_4TCNQ provides more charge transfer as compared to TCNQ molecules.[117,118] Through STM measurements at 5K, it has been found that TCNQ adsorbs on graphene substrate forming 2D molecular islands.[119] As interaction of F_4TCNQ is predicted to be higher than TCNQ, we are interested in exploring physisorbed F_4TCNQ molecules on graphene.

Recent studies with F_4TCNQ on single layer graphene show diverse behavior for electronic and adsorption properties on the surface. Most relevant works from the literature are presented in fig-1.4(c), in this direction. In these measurements, we find that the molecular assembly changes with the nature of substrate beneath graphene. The image in left and middle show molecules adsorbed on metallic substrates, such as Ir(111)[78] and Ru(0001),[120] which form moiré pattern with top graphene lattice. Typically we observe single molecules adsorbed on selective

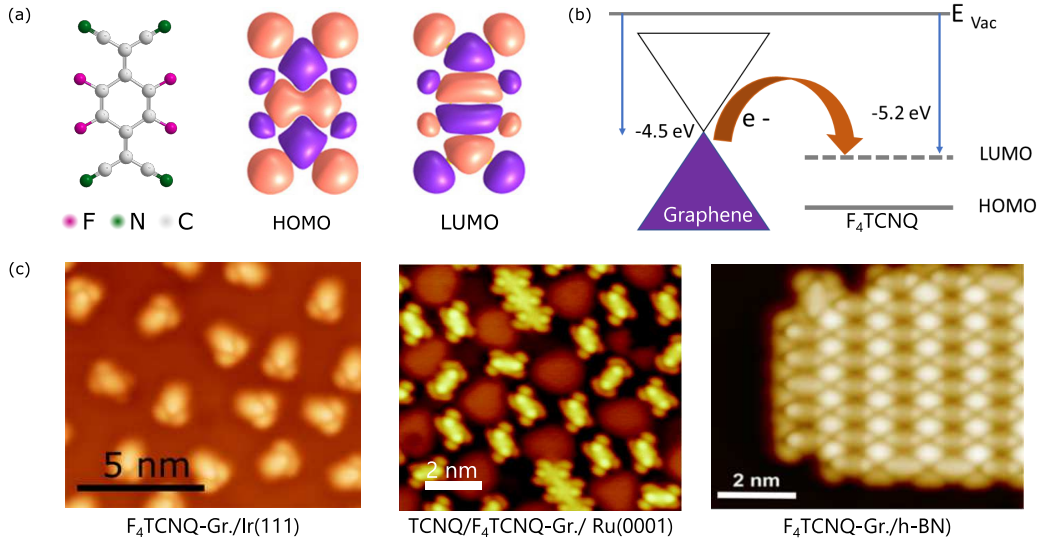

Figure 1.4: F_4TCNQ (a) Chemical structure of F_4TCNQ molecule (left), HOMO and LUMO of the molecule calculated in gas phase (middle and right). (b) Energy level schematic of separated graphene and F_4TCNQ molecule depicting p-doping of graphene through charge transfer. (c) STM topography image of F_4TCNQ molecules studied on graphene. *Left* shows single molecules on Gr/Ir(111) moire , *Middle* shows linear chains of TCNQ and single F_4TCNQ molecules on Gr/Ru(0001) moire , and *Right* Self-assembled 2D rectangular lattice of F_4TCNQ on Gr/h-BN substrate

sites of moiré cell depending on the charge transfer with the substrate (below graphene). Differences in the adsorption behavior for TCNQ and F_4TCNQ can be seen Gr/Ru(0001) system (middle image). Here, TCNQ forms small range linear chains in the low lying regions of moiré while F_4TCNQ co-exists as single molecules. Having an insulating substrate (or layer) beneath graphene, such as h-BN, leads to the formation of packed 2D assembly (right image).[79]

In the present work, we utilize a multilayer graphene substrate in pristine and N-doped forms. Since graphene is semimetallic, somewhere between metallic and semi-conducting, the influence of graphene layers below graphene on physisorbed molecules provides a unique perspective to understand the interface physics. The extension of the study with N-doped graphene further simplifies the understanding of molecules on low dimensional materials.

1.3.1 Black Phosphorus

After graphene, the most studied 2D material in its **elemental form** is black phosphorus. Black phosphorus is the most stable and dense allotrope of phosphorus under normal conditions. The crystal structure of black phosphorus is similar to graphite wherein the in-plane atoms have strong covalent bonds while in the perpendicular direction these layers are held together by weak van der Waals interaction. Monolayer of BP crystal having P-atoms in a puckered honeycomb

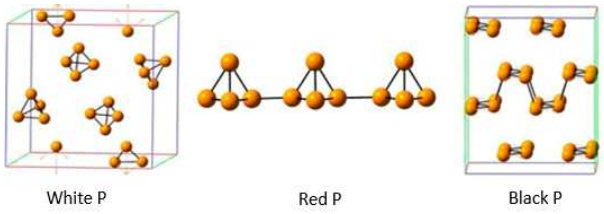

Figure 1.5: Common allotropes of Phosphorus

lattice is commonly referred to as phosphorene. Owing to its unique puckered structure, phosphorene demonstrates various novel anisotropic properties, mechanical flexibility, integer quantum hall effect, negative Poisson's ratio, and promising applications in gas sensors, electronics, photovoltaics, and energy storage.[121]

The weak coupling between phosphorene layers facilitates mechanical exfoliation which makes it possible to obtain few or even single layer phosphorene, just as graphene can be obtained from graphite (or HOPG). However, unlike graphene, black phosphorus is an optically active semiconductor[122] whose band gap increases with decreasing number of Phosphorene layers.[123] It is observed that the bulk black phoshorus has a band gap of around 0.3 eV[124] while that for phosphorene may go upto 1.6 eV.[125] Black phosphorus combines the flexibility of a two dimensional material with semiconducting properties which make it an interesting choice for electronics applications.[26]

Structure

Phosphorus exists in two major allotropic forms - white phosphorus and red phosphorus. The building block for all major forms of phospshorus is the P_4 unit. In fig-1.5, the arrangement of phosphorus atoms for most common and stable allotrope forms are shown. A P_4 molecule is formed from four covalently bonded P-atoms in a tetragonal arrangement. Since the bonds are formed by unhybridized $3p$-orbitals which prefer to stay at 90∘ to each other, it puts the molecule in a strained envrionment, imparting an unstable character . White phosphorus (1.5 a) is composed of tetrahedral P_4 molecules and exists in two crystalline forms- cubic crystal structure (α form) which is stable at room temperature, and hexagonal crystal structure (β form) which is stable upto 195 kelvin.[126] Red phosphorus, on the other hand, is an interlinked structure of P_4 units in a polymeric fashion(1.5b) formed by breaking a single P-P bond to link with the neighboring units.[127]

Black phosphorus is obtained from white or red phosphorus under high pressure. The constituent P_4 molecules form a two dimensional puckered honeycomb structure by breaking three bonds connecting with other units to form phosphorene layers held together by van der Waals

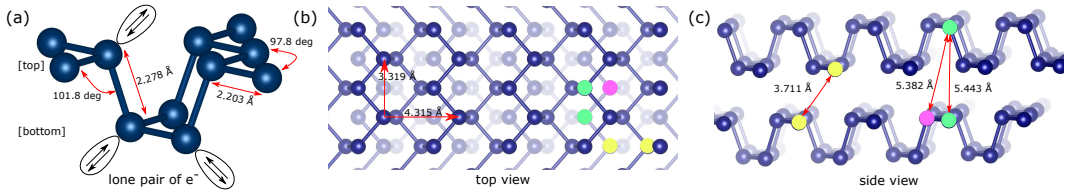

Figure 1.6: Atomic arrangement in black phosphorus lattice (a) A segment of phosphorene lattice showing the bond length, bond angle and lone pairs for P-atoms. (b) Top view of black phosphorus crystal showing the *in-plane* lattice vectors. Colored circles serve as visual guide to observe the atoms in top and bottom layers. (c) Side view of the BP crystal corresponding to **b** with colored circles.

interaction(fig-1.5c). The crystal structure of black phosphorus is orthorhombic having a space group $Cmca(64)$ with eight phosphorus atoms in the unit cell. This unique structure ensures that BP is the most thermodynamically stable form among all the phosphorus allotropes, in ambient conditions. In one way or another, it is the rearrangement of P_4 molecules that can be grown into 2D layers stacked along a crystallographic direction to produce black phosphorus or even blue phosphorene, very recently.[128]

In the phosphorene layer, phosphorus atoms are covalently bonded in sp^3 configuration. Within a single layer, they adopt a puckered honeycomb structure resulting in top and bottom layers of atoms to accommodate the bond angle required for this hybridization, as indicated in fig-1.6(a). This is in contrast to honeycomb lattice of graphene where all atoms are sp^2 bonded with lone pair of electrons pointing perpendicular to the plane of atoms. Owing to this puckered arrangement, the lone pair of electrons of the phosphorus atoms point with an inclination of approx. 45 degrees with the plane of atoms. A schematic for the atomic arrangement in bilayer phosphorene is shown in fig-1.6 from top-view (b) and side-view perspective (c). In this diagram, the lattice vectors and inter-layer distances are marked alongside their corresponding lengths.

From a technological perspective, phosphorene is more interesting and useful to study than black phosphorus. However, unlike graphene, the extraction of phosphorene and its manipulation for experiments are rather challenging. In this direction, surface studies on black phosphorus provide a good experimental background to understand the phosphorene 2D crystal structure and its properties.

Preliminary works using scanning tunneling microscopy have been performed on UHV cleaved black phosphorus crystals.[129,130] The STM images are shown in fig-1.7. Here we can observe the atomic arrangement with good resolution. The in-plane crystal structure and the anisotropy can be clearly seen in these images.

On these surfaces (fig-1.7), corresponding tunneling spectroscopy show an electronic band gap of 0.3 eV. Of particular interest are presence of dumb-bell shaped surface defects. The corresponding STS on these defects can be seen in fig-1.8. By comparing the STS on defects

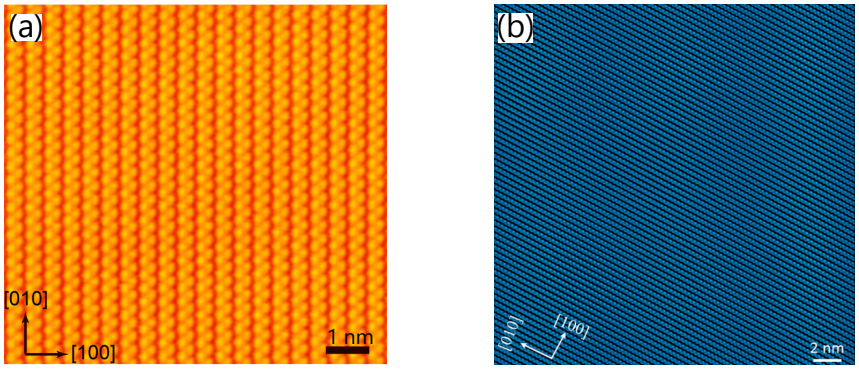

Figure 1.7: STM topography images taken by different research groups: Reference-(a) [130] and (b) [129] in bibliography

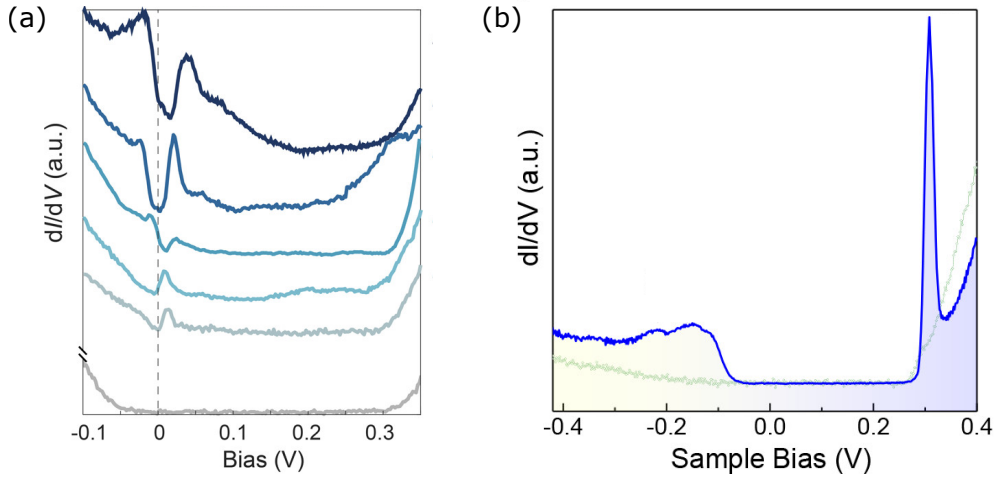

Figure 1.8: STS comparison on black phosphorus surface defects : Reference-(a) [130] and (b) [129] in bibliography

from these previous works we find that they are different and are debated to arise from a vacancy or presence of acceptor impurities.

Defects in optically active semi-conductors such as black phosphorus are vital to understanding of the material characteristics, from a technological point of view. We focus on the surface properties of black phosphorus and its defects, the results of which are detailed in coming chapters.

Functionalization of BP

For inorganic semiconducting crystals, the electronic properties is tuned by doping the lattice with donor or acceptor type atoms. Such approach proves to be difficult for layered vdW materials because the atoms may either intercalate between layers or form clusters on surface, and is often

difficult to control. For these materials, much of the physics takes in the atomic plane or at the interface. Functionlization of the surface (covalent or non-covalent techniques) may provide an easy alternative with wide range of options to modify the electronic and transport properties of the surface.

Also, the progress in the field of black phosphorus is hampered by its high sensitivity to ambient conditions. And a way to solve this issue is by encapsulating the surface with thin molecular layers which can functionalize the material at the same time. Non-covalent functionalization is an easier approach than covalent since we would like to keep the intrinsic properties, that are advantageous over other materials such as in-plane charge carrier mobility, which can reduce significantly when the surface is covalently modified.

At present, we find a good amount of theoretical work for molecules on BP, giving useful guidelines for practical experiments. Absorption of fullerene is shown to produce a deformation in the phosphorene monolayer leading to a shift in band structure.[131] In the same work, benzene physisorption has no effect on phosphorene electronic structure and is independent of the position of benzene molecule, and is projected as a good candidate for molecular encapsulation. The p-type conductivity of phosprorene has been shown to improve, following charge transfer with physisorbed F_4TCNQ molecules. Additionally, monolayer of F4TCNQ on blue-P can also assist in band engineering by creating heavy holes that are useful for the reduction of in-band tunneling.[132]

1.4 Thesis Outlook

This thesis aims to investigate the electronic properties of functionalized van der Waals materials, such as graphene and black phosphorus, by scanning tunneling microscopy and spectroscopy. The interface physics between non-covalently adsorbed molecules on surface often departs from the traditional explanation of energy level alignment in the Mott-Schottky framework. Photoemission based experiments for molecules on metallic substrates have provide ample evidence for this departure of explanation. Prediction of energy position for frontier orbitals levels on surfaces remains a daunting task for researchers. Aligned with this scientific problems, we utilize vdW materials to probe the charge transfer mechanism for physisorbed molecules.

1.5 Plan of the thesis

This thesis is divided into six chapters including the present one with introduction, i.e **Chapter-1**. Following introduction is the Experimental section (**Chapter-2**) which starts with a brief account on the theoretical physics for STM/S followed by the description of experimental setup

and related processes. The results for this doctoral work are then presented in the subsequent three chapters.

Since we have studied molecules on different substrates, i.e. on graphene and black phosphorus, we present results on graphene, first, in **chapter-3**&**4** followed by studies on black phosphorus in **chapter-5**

Chapter-3 is a STM/S based investigation of tautomerisation mechanism in tetraphenyl porphyrin, on pristine and nitrogen-doped graphene. On the same substrate, the adsorption and electronic properties of F_4TCNQ have been studied and presented in **Chapter-4**.

Chapter-5 is the last result chapter, where a combined study of surface defects in black phosphorus, degradation in ambient conditions, and the interaction of F_4TCNQ molecules has been presented.

From these studies, an overall conclusion is summarized in **Chapter-6**, the last chapter of the thesis.

Chapter 2

Experimental Methods

The beginning of 20th century saw the rise of quantum physics when Max Planck found the formula that could explain black-body radiation in 1900. The first three decades that followed were phenomenal in the development of modern physics. The ground breaking works of eminent scientists like Max Planck, Albert Einstein, Neils Bohr, Louis de Broglie and Schrödinger, to name a few (and without any particular order), played key role in laying down the foundations.[(a)] After years of research and development, Schrödinger proposed the famous wave equation in 1926, to describe the mechanics of particles which in one dimensional time dependent form is written as,

$$-\frac{\hbar^2}{2m}\frac{\partial^2\Psi(z,t)}{\partial z^2} + U(z)\psi(z,t) = i\hbar\frac{\partial\Psi(z,t)}{\partial t} \tag{2.1}$$

where $\hbar$ is planck's constant divided by 2π, m is particle's mass, $\Psi(x,t)$ denotes the time dependent wave-function describing the particle and $U(z)$ is the potential energy as a function of position.

The time independent solution of above equation for a particle having energy E has a non-vanishing probability to exist beyond a finite barrier of potential V (where $E < V$) of a certain width or spacing. This phenomenon has been commonly described as *quantum tunneling* and seems un-intuitive in classical aspects. It explains the process of radioactive decay, josephson effect, Esaki diodes, etc. The most profound application of quantum tunneling has been the invention of Scanning Tunneling Microscope (STM) by Binnig and Rohrer in 1982.[134] With this technique, it has become possible to obtain atomic resolution images of surfaces even at room temperature and remains an indispensable tool for surface science studies.

The technique has become quite matured in the last three decades and is well documented in textbooks. A short description of the theoretical background and the working principles for STM is presented in the next section that summarizes the important concepts and assumptions

[(a)] For a quick summary of the time line for the development of quantum mechanics, enthusiastic readers may find this short article[133] and the references therein very interesting.

therein.

2.1 Principle of STM

2.1.1 Theoretical background

In a STM, a sharp metallic tip is brought at a distance of a few Angstroms ($\mathring{A}$) of a conducting surface so that electrons can tunnel through the classically forbidden vacuum gap when a voltage bias is applied. The dependence of the current with the tip-sample distance can be understood from a one dimensional (1D) potential barrier model. The schematic shown in fig-2.1 depicts electrons tunneling from the left region (tip) of the vacuum gap to the right side (sample) of the barrier.

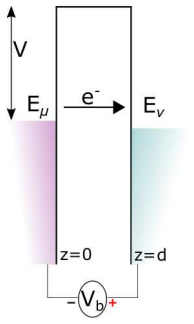

Figure 2.1: One dimensional model of a tunnel barrier

In one-dimension, Schrödinger equation is written as,

$$-\frac{\hbar^2}{2m}\frac{\partial^2\Psi(z)}{\partial z^2} + U(z)\psi(z) = i\hbar\frac{\partial\Psi(z)}{\partial t} \tag{2.2}$$

and the solution is given in the following form

$$\psi(z) = \begin{cases} Ae^{\pm ikz} & (z < 0) \\ Ce^{\pm\beta z} & (0 \leq z \leq d) \\ Fe^{ikz} & (z > d) \end{cases}$$

$$\text{where} \quad k = \sqrt{\frac{2mE}{\hbar^2}} \quad \text{and} \quad \beta = \sqrt{\frac{2m(V-E)}{\hbar^2}} \tag{2.3}$$

Here, V is the potential energy barrier encountered by the electron which has an energy E where $E < V$. In the zero temperature limit, the electrons are filled only upto the Fermi level E_F for metals, so that E can be identified with E_F. The potential barrier is the energy difference

between E_F and the vacuum level which is the work-function (ϕ) of the material. The decay constant for $\psi(z)$ inside the barrier is $\beta = \sqrt{\frac{2m\phi}{\hbar^2}}$.

The transmission probability T of finding an electron on the other side of barrier is given by the ratio $|F|^2/|A|^2$

$$\begin{aligned} T = \frac{|F|^2}{|A|^2} &= \left[1 + \frac{1}{4}\frac{V^2}{E(V-E)} sinh^2\left(\frac{d}{\hbar}\sqrt{2m(V-E)}\right)\right]^{-1} \\ &= \left[1 + \frac{1}{4}\frac{V^2}{E(V-E)} sinh^2(\beta d)\right]^{-1} \\ \text{In the case, } \beta d \gg 1 &\text{we can write } sinh(\beta d) \approx \frac{1}{2}e^{\beta d} \\ \text{Therefore, } T &\approx \left[\frac{1}{16}\frac{V^2}{E(V-E)} e^{2\beta z}\right]^{-1} \\ &\approx \frac{16E}{V}\left(1 - \frac{E}{V}\right) e^{-2\beta z} \\ \text{or, } T &\propto e^{-2\beta d} \end{aligned} \tag{2.4}$$

The probability tunneling current (I) is proportional to the transmission probability and has the same exponential dependence with parameters β and z, as comes out in above equation (2.4) for T.

Local density of states

We consider the empty and filled states for the electrons tunneling from tip to sample or vice versa. In the schematic shown (fig-2.1), electrons are depicted as tunneling from filled μ^{th} state at the fermi level of tip to the empty ν^{th} state of the sample. The two states are at the same energy level to conserve the energy of electron in the *elastic tunneling approximation*. For n discrete states at energy E, the density of states (DOS) can be written as,

$$\rho(E) = \sum_n \delta(E - E_n) \tag{2.5}$$

where δ represents the Dirac delta function. As it will be described later, the current in STM is related to the *local density of states* (LDOS). The LDOS is expressed as the DOS modulated by the probability ($|\psi(\mathbf{r})|^2$) of a particle to be at position $\vec{r}$

$$\text{LDOS} = \rho(E, \vec{r}) = \sum_n |\psi_n(\vec{r})|^2 \delta(E - E_n) \tag{2.6}$$

Due to an external bias (V_b) between tip and sample, the fermi level of the left and right are shifted. For negative bias on tip, $E_{F,tip}$ shifts upwards in energy with respect to $E_{F,sample}$.

Working in the zero temperature approximation, tunneling can occur only in the bias window between $E_{F,tip}$ and $E_{F,sample}$.

Bardeen had put forward a theory for the transition rate of electrons from one electrode to another in case of tunneling in a metal-insulator-metal structure, long before STM was invented.[135] It took into account Fermi's golden rule for electrons tunneling or scattering from initial state (μ) to the final state (ν) on the other side of barrier, given by

$$\omega_{\mu\to\nu} = \frac{2\pi}{\hbar}|M_{\nu\mu}|^2\delta(E_\nu - E_\mu) \tag{2.7}$$

where $|M_{\mu\nu}|^2$ is the matrix element of the transition probability and expressed as

$$M_{\nu\mu} = \frac{\hbar^2}{2m}\int (\psi_\mu \nabla\psi_\nu^* - \psi_\nu^*\nabla\psi_\mu)\cdot d\vec{S} \tag{2.8}$$

The integral is over any surface (S) lying entirely within the vacuum (barrier) region separating the two sides. Tunneling current is then obtained from the transition rate (number of electrons per unit time) by multiplying with unit charge and summing it over all the states available for tunneling. Thus from equation-2.7, we obtain

$$I = \frac{2\pi e}{\hbar}\sum_{\mu,\nu}|M_{\nu\mu}|^2\delta(E_\nu - E_\mu) \tag{2.9}$$

Summing over the filled energy states at tip and the empty states on sample, in the bias window (eV_b), the equation of tunneling current can be written as,

$$I = \frac{2\pi}{\hbar}e^2V_b\sum_{\mu,\nu}|M_{\nu\mu}|^2\delta(E_\mu - E_F)\delta(E_F - E_\nu) \tag{2.10}$$

Tersoff-Hamann approximation

Above equation, in Bardeen formalism, derived for the tunneling current is quite general and warrants some approximations to calculate the matrix element in the case of an STM experiment. The approximation which is widely used the Tersoff-Hamann approximation. In this approximation, the tip is modeled as a locally spherical potential well where it approaches nearest the surface. The energy dependence of the matrix element is neglected around the fermi level and is applied in the limit of small tunneling bias voltages.

Green's function approach The matrix element $M_{\nu\mu}$ can be evaluated by using the Green's function $G(\vec{r}-\vec{r_0})$ corresponding to the Helmholtz equation, which is defined by

$$\left[\nabla^2 - \beta^2\right]G(\vec{r}-\vec{r_0}) = -\delta(\vec{r}-\vec{r_0}) \tag{2.11}$$

The solution is known and is given by

$$G(\vec{r}-\vec{r_0}) = \frac{\exp\left(-\beta|\vec{r}-\vec{r_0}|\right)}{4\pi|\vec{r}-\vec{r_0}|} \tag{2.12}$$

The solution obtained above is the spherical wavefunction also known as s-wave solution. In the Tersoff-Hamann approximation, the wavefunction of the tip is assumed to have a spherical form just like shown in equation-2.12. We take the tip wavefunction to be

$$\psi_\mu(\vec{r}) = \frac{4\pi C}{\beta} G(\vec{r}-\vec{r_0}) \tag{2.13}$$

where C is a constant. The value of the matrix element is then solved by using the tip wavefunction from equation-2.13 by using equation-2.14. We have

$$\begin{aligned}
M_{\nu\mu} &= \frac{\hbar^2}{2m}\int (\psi_\mu \nabla\psi_\nu^* - \psi_\nu^*\nabla\psi_\mu)\cdot d\vec{S} \\
&= \frac{2\pi C\hbar^2}{m\beta}\int [G(\vec{r}-\vec{r_0})\nabla\psi_\nu^* - \psi_\nu^*\nabla G(\vec{r}-\vec{r_0})]\cdot d\vec{S} \\
&= \frac{2\pi C\hbar^2}{m\beta}\int \left[G(\vec{r}-\vec{r_0})\nabla^2\psi_\nu^* - \psi_\nu^*\nabla^2 G(\vec{r}-\vec{r_0})\right] d\tau \\
&= \frac{2\pi C\hbar^2}{m\beta}\int \left\{G(\vec{r}-\vec{r_0})\beta^2\psi_\nu^* - \psi_\nu^*\left[\beta^2 G(\vec{r}-\vec{r_0}) - \delta(\vec{r}-\vec{r_0})\right]\right\} d\tau \quad \text{(from eqn-2.11)} \\
&= \frac{2\pi C\hbar^2}{m\beta}\int \psi_\nu^*\delta(\vec{r}-\vec{r_0}) d\tau \\
&= \frac{2\pi C\hbar^2}{m\beta}\psi_\nu^*(\vec{r_0})
\end{aligned}$$

therefore,

$$M_{\mu\nu} \propto \psi_\nu^*(\vec{r_0}) \tag{2.14}$$

The expression for tunneling current as obtained in equation-2.10 can be now simplified in the Tersoff-harmann approximation by substituting the value obtained for the matrix element in equation-2.14. We get

$$\begin{aligned}
I &\propto \sum_{\mu,\nu} |M_{\nu\mu}|^2 \delta(E_\mu - E_F)\delta(E_F - E_\nu) \\
&\propto \sum_{\mu,\nu} |\psi_n(\vec{r})|^2 \delta(E_\mu - E_F)\delta(E_F - E_\nu)
\end{aligned} \tag{2.15}$$

from the definition of LDOS as given in equation-2.6, above equation for tunneling current

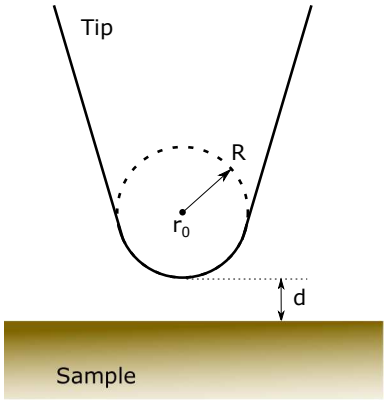

Figure 2.2

can be expanded on the basis of LDOS for the tip and sample surface separately, and expressed as

$$\begin{aligned} I &\propto \sum_{\mu,\nu} \rho_{\mu}(E)\rho_{\nu}(\vec{r},E) \\ \text{or,} \\ I &\propto \sum_{\mu,\nu} \mathrm{DOS}_{tip}(E)\mathrm{LDOS}_{sample}(\vec{r},E) \end{aligned} \tag{2.16}$$

Now, summing upon all the available tunneling states in the bias window $(0-eV_b)$, we replace the summation with an integration sign and write the expression for tunneling current as,

$$I \propto \int_{E_F}^{E_F+eV_b} \rho_{tip}(E)\rho_{sample}(\vec{r},E)d(E) \tag{2.17}$$

Thus, the tunneling current is proportional to the electrons tunneling through the available density of states of the tip and sample in the range of bias window. Based on this equation scanning tunneling microscopy and spectroscopy can be interpreted.

Equation-2.17 does not yet give a straightforward relation between the tunneling current and the properties of the sample because the LDOS of the sample convoluted with the DOS of the tip. However, for a perfect metallic tip, the density of states can be considered to be constant. In that case, the tunneling current can be expressed as:

$$I \propto \int_{E_F}^{E_F+eV_b} \rho_{sample}(\vec{r},E)d(E) \tag{2.18}$$

2.1.2 Scanning Tunneling Microscopy and Spectroscopy

STM

Scanning tunneling microscopy (STM) is a scanning probe technique where a sharp metallic tip acts as a local probe through which tunneling current is sampled as a function of the surface position on sample. A collection of tunneling current values for different surface position plotted in two dimensions gives the topography image for the area under observation. A STM topography image can be obtained in two operating modes, after the tip approaches in the tunneling regime:

- Constant current mode
- Constant height mode

In the constant current mode, the current feedback loop of the control system is closed which maintains the tunneling current setpoint defined by the user. The tunneling current is proportional to the transmission probability which varies exponentially with the tip-sample distance as shown in equation-2.4. Therefore, to maintain a constant current, the distance between the tip and sample is adjusted as the STM tip scans the surface of the sample. The LDOS on the sample surface changes locally, the magnitude of which depends on the material under investigation. As a result of this variation, the tip retracts or approaches the surface depending on whether the LDOS at a given point gives higher or lesser tunnel current, as compared to the tunneling current setpoint. Thus, the data obtained in this mode is composed of relative tip height over the surface which is displayed in digital format. To visualize this information, the 2D matrix is represented by false colors which can be defined by the range of tip deflection in the entire data set. The reference tip-sample separation, here, is dictated by the current set-point and a higher value represents tip retraction (high LDOS) while a lower value denotes tip approach (low LDOS). Usually, low LDOS regions are represented with dark colors while high LDOS regions are shown in bright colors. In a typical STM viewgraph, a color scale bar is presented alongside the image to illustrate the relative range of tip movement.

In the constant height mode, the current feedback loop is opened once the tip approaches tunneling distance as defined by the initial current set-point. The tunneling distance remains constant while scanning the surface and any changes in LDOS results in varying tunneling current. A higher LDOS gives higher tunneling current and vice-versa. The 2D data matrix is then composed of current values for all the points scanned on the sample. This is represented by false colors in a digital format similar to a constant current image, the only difference being the color scale bar which now represents the range of tunneling current variation relative to the current set-point before the feedback loop is opened.

In principle, both techniques can be used to obtain LDOS information for the sample surface. However, in most cases, constant current mode is employed for STM imaging which provides an added advantage in terms of large variations or corrugations in local surface profile. It also helps to avoid unwanted collisions of the tip with the sample that has high surface irregularities.

STS

Scanning tunneling spectroscopy (STS) is performed by recording tunneling current as a function of bias voltage, at a given point on the surface. The feedback loop system adjusts the tip height based on the tunnel bias and current set-point. The feedback loop is then opened to perform a STS measurement in a given voltage (energy) range. The sample is always kept at ground in the experiments and all voltages are applied at the tip. We saw from equation-2.19 that the current is proportional to the combined LDOS of tip and sample within the bias energy window. For most practical considerations, the LDOS for tip is assumed to have a constant profile in the measurement energy range at low temperatures. Thus, we approximate the tunneling current as,

$$I \propto \int_{E_F}^{E_F+eV_b} \rho_{sample}(\vec{r}, E) d(E) \tag{2.19}$$

The current at a given bias sums up the LDOS information from the fermi level. To obtain the LDOS profile as a function of energy, the derivative of the current (dI/dV) is taken

$$\frac{dI}{dV} \propto \rho_{sample}(\vec{r}, E) \tag{2.20}$$

Therefore, by performing STS it is possible to map the LDOS point by point on an atomic scale which is an important tool in surface science. By plotting the current derivative as a function of position, we get the dI/dV or a conductance map at a given energy level. Series of such images show more information in the form of a movie which essentially shows the evolution of DOS as a function of energy. Thus, the quantity dI/dV is tremendously useful in the surface science and specially for low dimensional systems, molecules, point defects, etc.

Tunneling currents are usually in the range of nA to pA which is extremely small and very close to the instrument's electronic noise level. Hence the current is amplified using an extremely low noise trans-impedance pre-amplifier for analog and digital post processing. The derivative of the tunnel current is obtained from a lock-in-amplifier using a small signal *ac* modulation. In this configuration, the modulation from lock-in is provided to the voltage input to the tunnel junction through the controlling instrumentation. During a STS measurement, both the channels of current (amplifier) and its derivative (lock-in output) are saved in a given energy range.

Few variations of the STS are obtained by playing with the parameters of feedback loop,

voltage, current and tip-sample distance. To monitor changes in the tunneling current as a function of time, voltage is ramped with a null difference in a given time interval. This keeps the energy constant and records the time dependent current. As usual, the feedback loop is opened for this measurement. An example of such measurements are presented in chapter-3 (for example see figure-3.5). In constant height mode, dZ/dV spectroscopy is made by recording the sample-tip separation.

The typical value of work-function (ϕ) for most metals lie in the range of $4 - 5eV$ which roughly translates to $\beta = 1\mathring{A}^{-1}$. With some algebra, it can be observed from equation-2.4 that the tunneling current drops one order of magnitude for every Å of vacuum separation (d) between the electrodes. Thus, the tip-sample distance has to be maintained with extremely low vibrations so as to keep the tunneling current stable and within acceptable fluctuations. Thus, the two main components of the STM instrument comprises of state of the art technology for (1) feedback control system and, (2) noise (electrical and mechanical) isolation. A brief description of the machine setup is presented next.

2.2 STM instrument setup

A commercial low temperature (LT) STM machine procured from Omicron NanoTechnology GmbH has been used for all measurements. It is run by Matrix SPM control that includes the microprocessor based control system and the software interface installed on a separate windows XP desktop computer. The complete setup can be viewed in the labelled photograph of figure-2.3. The main components and its functionality are detailed below:

Chambers: Two main chambers in this machine are the preparation and LT chambers. Samples are transferred from a load lock chamber (inset figure-2.3) to the preparation chamber where annealing, direct-current heating, argon sputtering and LEED can be performed. Adjacent to it, is LT chamber fitted with a cryostat. The STM instrumentation is spring suspended in this chamber and surrounded by double cylindrical enclosures to maximize thermal insulation. Eddy-current damping is also present to reduce mechanical vibrations.

Low temperature cryostat: Two coaxial cylindrical vessels house the cryogenic liquid to reach temperature down to 4.6 K. The cryostat is storage type where the inner part is filled with liquid helium and the outer part with liquid nitrogen. Normal refilling is done every 48 hours in this setup.

Cryogenic pumping: The two chambers are provided with UHV pumping systems that include separate turbo and ion-pumps. A base pressure of less than 10^{-10} mbar is maintained in normal working conditions. Pumping for load-lock has a separate turbo unit backed by a primary pump. Pressure gauge monitors are used for continuous monitoring in both the

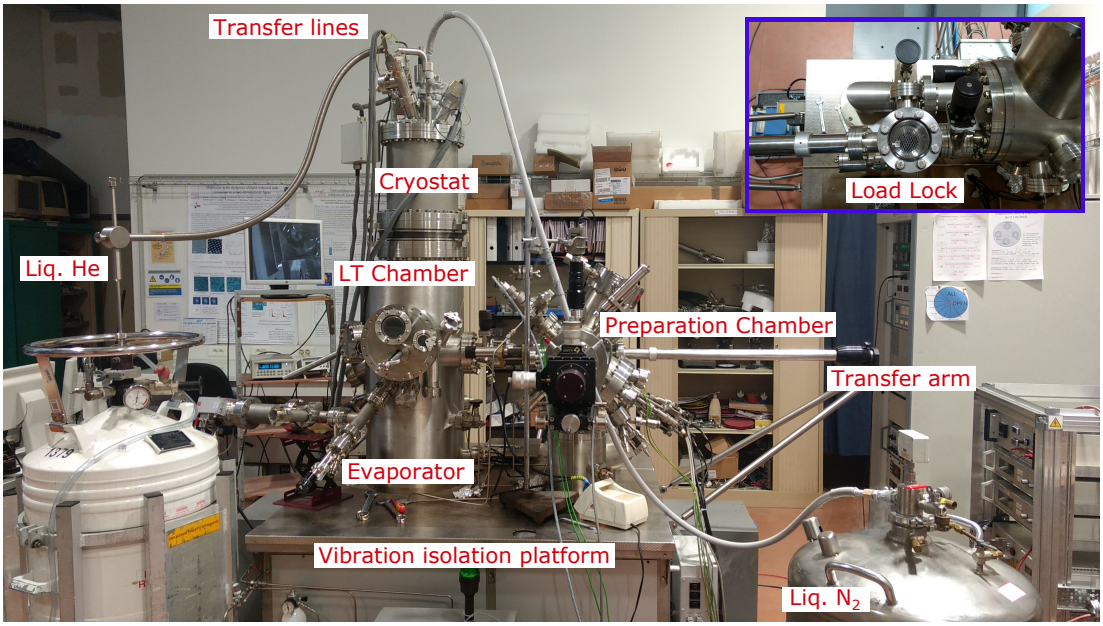

Figure 2.3: Omicron LT-STM machine with air damping platform shown during refilling.

chambers. Besides these units, the chambers are equipped with tungsten sublimation pumps to further improve the base pressure periodically.

Air-damped Control system: Entire STM setup rests on an active vibration isolation platform, also procured from Omicron, that greatly reduces the mechanical noise in the experiments. The platform is supported by three hydraulic damping legs controlled by separate feedback based control system. In our setup, the noise on the STM tip is recorded to be less than 1 pm peak-to-peak when measured in the point mode at 4.6 K.

2.3 Methods

2.3.1 STM tip preparation

A sharp metallic tip is a quintessential requirement for the atomic scale imaging of surfaces. Besides obtaining a narrow tip profile as much as possible, one needs a tip with a stable atomic configuration at the apex position and free from contaminants. Keeping these factors in mind, an electrochemical etching method is employed to prepare STM tips using tungsten wires.

Electrochemical etching

The electrochemical etching of metal like tungsten gives greater control on the preparation of tips for STM purpose due to a very slow rate of metal dissolution. It's setup involves the following

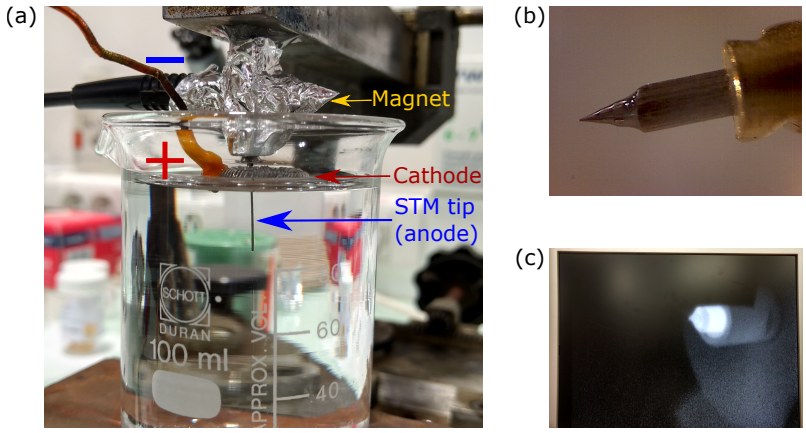

Figure 2.4: Experimental setup demonstrating etching of tungsten tip observed as a thin line

components:

- Electrodes: A blunt tungsten cylindrical wire of 0.5 mm diameter having 99.99 purity which acts as anode while a toroidal palladium coil acts as cathode.
- Electrolyte: Sodium hydroxide solution of 4M concentration is used.
- Power Supply: A home built electronic setup is used to drive the electrochemical reaction which is explained below.

The reactions taking place at the cathode and anode are described by following chemical equations.

$$\begin{aligned} Cathode: \quad & 6H_2O + 6e^- \rightarrow 3H_2(g) \uparrow + 6OH^- \\ Anode: \quad & W(s) + 8OH^- \rightarrow WO_4^{2-} + 4H_2O + 6e^- \\ Total: \quad & W(s) + 2OH^- + 2H_2O \rightarrow WO_4^{2-} + 3H_2(g) \uparrow \end{aligned} \tag{2.21}$$

The etching process of a tungsten wire fixed on tip holder can be viewed in the photograph shown in figure-2.4(a). The tip is surrounded by a circular shaped coiled cathode which ensures homogeneous etching from all sides. A three dimensional concave profile builds up around the tungsten wire which gradually progresses with time eventually splitting the wire with extremely sharp ends. After the second part separates from the tip, it is dipped inside the electrolytes by 1-2 mm to get rid of an extremely pointy tip which has unstable atomic configuration and is also quite fragile to handle. The electrochemical etching continues for 10-15 seconds for this latter stage.

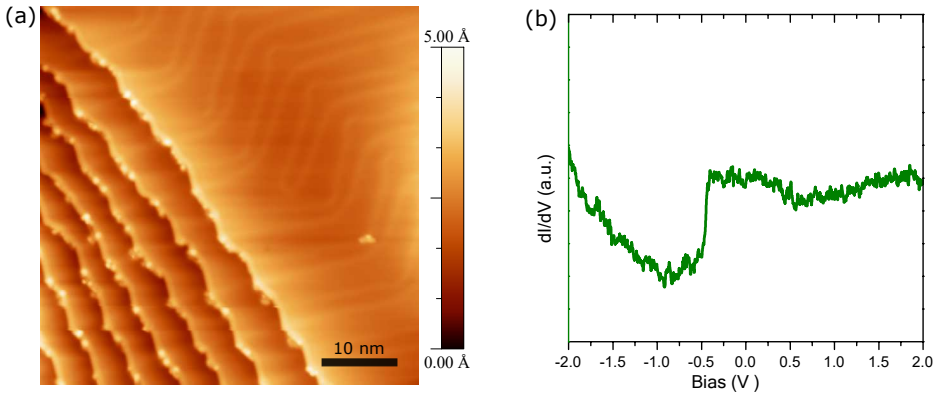

Figure 2.5: STM and STS on Au(111) surface for tip calibration

Once the etching is complete, it is thoroughly rinsed under running de-ionised water for two minutes to dissolve the electrolyte on the tip. The tip is then blow dried with dry nitrogen gas to remove moisture. Thereafter, it is transferred to the UHV chamber for further tip conditioning, described next.

Tip conditioning

Surface of freshly prepared tungsten tips are prone to adsorbates and may contain some impurities from the electrolyte solution. The tip is cleaned under UHV conditions to get rid of such contaminants. Once transferred to the preparation chamber, a direct current is passed through the axis of the tungsten wire which sits in the tip holder. Current is gradually increased which results in resistive heating of the metallic conductor. Initially, the degassing of the tip takes place which is monitored by rise in pressure of the preparation chamber as the temperature (current) is gradually increased. The STM tips show a resistance of around 0.7 to 1 Ω for which the first phase of degassing usually gets over in an hour with the maximum current reaching 1.5A. Thereafter, the current is increased rather steeply going from 1.5 A to 4 A in two minutes or less. With this treatment, the tips get heated enough to start emitting radiation in the visible range seen as faint red color. The image shown in figure-2.4(c) is captured by a CCD camera (black and white) and displayed on monitor for a tungsten tip being treated with 4.5 A direct current. Once the tip starts emitting red light, a short flashing of the tip is performed by increasing the current by one ampere lasting 20 seconds. The flashing of tip is observed as bright yellow light wherein the temperature can reach upto 3000 K or more. This heat treatment gets rid of most contaminants and volatile adsorbates while leaving the tip with a stable atomic arrangement at the apex.

The tip-flashing technique gives extremely good results in terms of tip conditioning and, in

principle, can be used for STM without further conditioning. However, for the purpose of fine tuning, the tips are calibrated on a clean metal surface for reliable spectroscopy. The idea of using a metal surface is twofold: (1) the metal surface reconstructions and atomic lattice parameters serves as a reference point to check the imaging conditions with the tip, and (2) the spectroscopy as measured by tip is calibrated to have a rather constant or featureless DOS profile when used for studying new surfaces and molecules.

For the present work, all STM tips have been calibrated on UHV cleaned Au (111) surface. The tip conditioning on Au surface involves voltage pulses and controlled sub-nanometer dents into the surface until a strong signature of shockley surface states are seen in the STS. A good tip is characterized by reproducible spectroscopy and sharp imaging conditions verified by the height of step edge and surface reconstructions. In figure-2.5 the STM of a Au (111) surface is shown with step edges where tip is calibrated. The STS on this area is shown in right where the sharp change in the STS can be observed at -0.45 V due to shockley surface state.

2.3.2 Sample preparation

The first tool available to prepare samples for surface science measurements and specially in HV and UHV conditions is thermal annealing. Depending on the nature of the substrate various methods can be applied to either heat the surface to very high temperatures or remove the top few layers to obtain fresh and clean surface for STM studies. Based on the samples that have been studied in this thesis, their cleaning procedures are detailed below:

Au(111)

Cleaning and preparing of metallic surfaces like gold, copper, cobalt, silver, etc is done by argon sputtering followed by high temperature annealing. Sputtering cleaning by noble gas like argon ensures no other chemical species are created in the process that may combine with the freshly prepared surface. However, implantation may occur if the energy of incoming ions are high. For Au (111) surface cleaning, energy of 0.7 - 0.8 keV are used in the pressure of 2×10^{-6} mbar pressure. The sample surface is kept at 45 degrees with respect to the flux of argon ions. To ensure maximum exposure, emission current from the sample is monitored with a keithley multimeter 2400 to adjust the sample position giving the maximum current after the argon pressure becomes stable.

The sputtering is done for around 10-15 minutes followed by annealing the sample just below the melting point. In this case, temperature is slowly ramped upto 400 deg celsius and maintained for 30 minutes before ramping down the temperature at a rate of no more than 3 deg/min. Samples are then transferrred to the low temperature (LT) chamber for imaging.

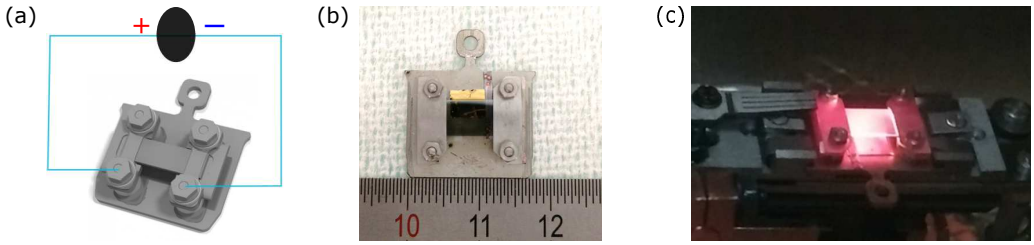

Figure 2.6: Sample plate for mounting graphene sample and UHV cleaning

Multilayer graphene

Multilayer graphene (≈5-10 layers) samples were grown on SiC(000$\bar{1}$) crystal by annealing these substrates in ultrahigh vacuum (UHV) at 1320°C for 12 min under a silicon flux of ≈1 ML/min. After synthesis, the sample was transferred in air to a UHV chamber and degassed for a few minutes before the measurements. Doping of these pristine graphene samples with nitrogen atoms gave nitrogen-doped graphene. Nitrogen doping was obtained by exposing the graphene sample to a flux of nitrogen radicals produced by a remote RF plasma source.[136] Both pristine and N-doped graphene samples have been used as substrates for molecular functionalization studies. These graphene samples were studied in a special type of mounting sample holder that facilitates passing a direct current through the top surface.

A schematic of the sample plate shown in figure-2.6(a) in which the top metal strips that are fixed with the sample act as conduit for electric current while the rest of sample is electrically insulated. A graphene sample used for STM is shown in figure-2.6(b) with a scale below for visual aid. In this sample plate, a gold (111) on Mica is also fixed alongside the graphene sample to prepare STM tips without changing the sample plate. Since graphene is semi-metallic and has resistance in the order of few hundred ohms, a small current is high enough to heat the top layers. In the experimental setup, this corresponds to starting with 0.1 A current which heats up the graphene leading to degassing of the sample. After waiting 15-20 min, the increment in pressure drops down and the current is increased. Starting from 0.3 A, the sample is seen to emit bright red light as can be seen in fig-2.6(c). After this point, the graphene samples are flashed for 10-15 seconds by increasing the current upto a maximum of 0.5 A, depending on the observed brightness.

Black phosphorus

Black phosphorus is a soft crystal which is difficult to handle and clean for UHV measurements. Due to its high surface reactivity, various adsorbates bind chemically which are hard to get rid off. First and foremost issue comes with the mounting of the sample using the conventional spot

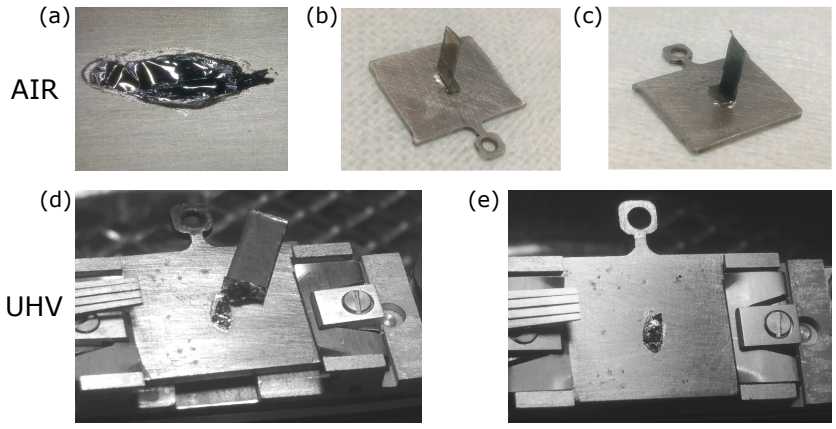

Figure 2.7: UHV cleaving of black phosphorus crystal

welded molybdenum strips. The BP crystals deform with the slightest touch making it hard to ensure a good electrical contact with the sample plate for STM measurements.

To overcome such issues, we fix the black phosphorus crystals on the sample plate by using electrically conducting silver epoxy. The silver epoxy used here is called EPO-TEK H21D and has been commercially procured from Epoxy Technology. A droplet of the prepared epoxy is put on the sample plate and after that a black phosphorus crystal is gently placed on top of it. The sample plate is then heated to 140 degree celsisus for 40 minutes to cure the epoxy. An example of a mounted BP crystal is shown in the figure-2.7(a). For the purpose of UHV cleaving or exfoliation, a L-shaped molybdenum strip of suitable dimension is fixed on top of the BP crystal with the same epoxy glue. After curing the sample, the strip should be firmly fixed on to the top layer of the black phosphorus crystal and not touching the sample plate. In figure-2.7(b) and (c), images are shown for sample plate with the L-strip mount for cleaving.

After transferring the prepared L-strip sample inside the preparation chamber, the sample is degassed upto 120 degree celsius until the pressure stabilises, typically not more than 2 hours. After the sample cools down to room temperature, cleaving is performed by the transfer arm by making a gentle stroke on the strip strong enough to cleave the top layer of BP exposing clean surface. In figure-2.7(d), we can see the L-strip which has exfoliated the top surface after being pushed by transfer arm, and is slightly attached to the crystal at the end. In this image we can also see the other side of the cleaved surface which is glued to the L-strip which confirms successful cleaving of the crystal surface. The sample shown in fig-2.7(e) has been cleaved and is ready for STM measurements.

Molecule	Temperature	Evaporation time
H_2TPP	255°C	30 sec to 5 min
F_4TCNQ	104°C	1 min to 15 min

Table 2.1: Parameters for evaporating molecules on samples in UHV conditions

Molecular Evaporation

Molecular deposition is performed by using knudsen-cell evaporator for all our measurements. Quartz crucibles are cleaned first by degassing in high vacuum conditions (10^{-7} mbar pressure) upto a temperature of 600 degree celsius before being used for molecules in the UHV system. All molecules before being evaporated on the sample are degassed just below their evaporation temperature for more than 4 hours. The parameters for the evaporation of the molecules studied are detailed in table-2.1

Molecular deposition in UHV can be made at room temperature or at the low temperature STM stage maintained at 4.5 K. Room temperature evaporation takes place in preparation chamber after which the sample are cooled down to low temperature for microscopy. In the present work, all evaporations have been performed for samples kept inside the LT chamber where the average temperature is around 5.5 K during deposition. The knudsen cell evaporator is fitted with an independent pumping unit that maintains a base pressure in the range of 10^{-8} mbar and is separated from the LT chamber by a vacuum valve.

Chapter 3

Dynamics of proton-transfer in free base porphyrin

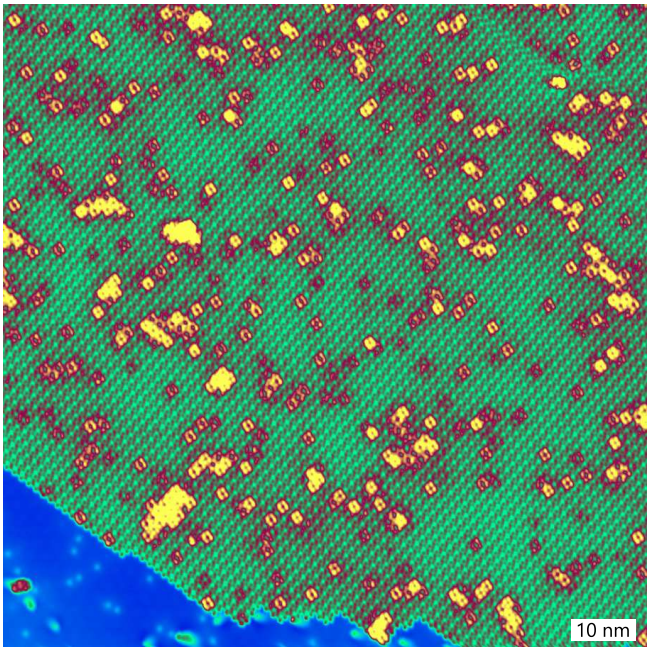

This chapter focuses on the control of hydrogen transfer in the cavity of free base poprhyrin molecule and the determination of the excitation mechanism for the transfer reaction. Comparative analysis on pristine and nitrogen-doped graphene is presented for experiments performed at 5K. On graphene, two stable configurations of porphyrin are identified with respect to the position of H-atoms with characteristic contrast in STM image (bright and dark) due to difference in tunneling conductance. The interconversion rates of dark and bright forms are analyzed to understand the dynamics of hydrogen transfer in the porphyrin core, and are further supported

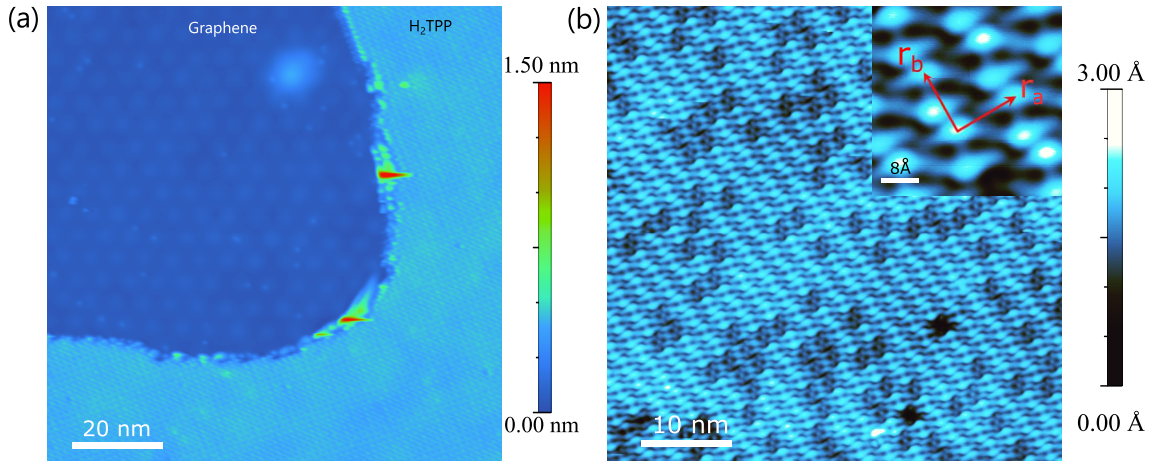

Figure 3.1: H_2TPP on pristine graphene (a) Large scale STM topography image showing sub-monolayer coverage of H_2TPP lattice on pristine graphene (-1.5 V, 20 pA). (b) Zoomed area on molecular layer with molecules packed in square lattice. The inset shows the lattice vectors with $\vec{r_a}$ 1.39 nm and $\vec{r_b}$ 1.38 nm. (-1.5 V, 10 pA)

by theoretical calculations.

3.1 Porphyrin on pristine graphene

STM

Tetraphenyl porphyrin is evaporated directly onto the cold (≈5.5 K) multilayer graphene substrate grown on SiC(000$\bar{1}$) crystal. On pristine graphene substrate, porphyrin (H_2TPP) molecules self assemble into 2D molecular islands when the sample is annealed to room temperature. A large scale STM topography image of self-assembled porphyrin molecules is shown in fig-3.1(a). Molecular coverage is sub-monolayer and the underlying graphene substrate can be seen in the left side of this image. The packing of molecules in this 2D island can be seen in the image on right, fig-3.1(b), with an inset on upper right corner showing a zoomed area. Porphyrin packs in a square type lattice due to its four membered ring structure. In the inset of fig-3.1(b), the molecular lattice vectors can be identified with red arrows. The vectors are perpendicular to each other and have magnitude of 1.39 nm ($\vec{r_a}$) and 1.38 nm ($\vec{r_b}$), as obtained from STM measurement.

In the molecular lattice, we find a difference in the contrast for some molecules. Most of the molecules are bright while others have a dark contrast. These two types of molecules correspond to the tautomers having different tunneling conductance at a given bias set-point. For identification, these tautomers are referred to as "bright" and "dark" forms. We can clearly see that the molecular island is composed of randomly distributed *bright* and *dark* forms of tautomer.

H_2TPP tautomers have been studied on Au(111) substrate previously in our group.[137] In this

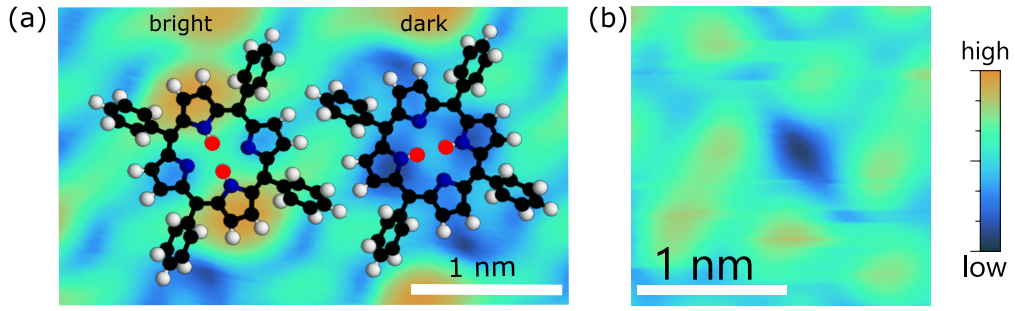

Figure 3.2: Tautomers of porphyrin

work, bright and dark tautomeric forms can be differentiated in the conductance map of single molecules. With the help of theoretical calculations, the molecular structure corresponding to the tautomers was identified. The pyrrole group in the macrocycle are somewhat twisted with respect to its neighbors. As a result, two pyrrole rings point upwards and other two downwards. The convention for defining "upwards" or "downwards" is related to height of C-C bonds in the pyrrole ring with respect to the surface. Pyrroles pointing upwards have N-atoms closer to surface, and subsequently the C-C double bond is at a elevated height from the surface. For reference, these pyrroles are called as α pyrroles and the other two as κ pyrroles.[(a)] In terms of the position of H-atoms for the tautomers, the bright form corresponds to the arrangement where the inner hydrogen atoms are attached to α pyrrole groups also referred as H_α configuration, while dark form corresponds to H_κ configuration.

Molecular schematic corresponding to tautomers are shown in fig-3.2. The left image (3.2a) shows the bright and dark tautomers in the same area, lying side by side, and are superimposed with the molecular structure. In this comparison, we can observe the position of H-atoms in H_α and H_κ configuration. This image of bright and dark tautomers has been taken at negative polarity (-1.5V) and shows the HOMO shape of the molecule. On the other hand, the image on right is taken at positive polarity (2.2V) which corresponds to LUMO of the molecule. The difference in the HOMO and LUMO shape is quite evident in these images. We can see two bright lobes for HOMO state and four smaller lobes for LUMO. Concerning the bright and dark tautomers, they can be identified clearly in the negative polarity which is the HOMO state but with different conductance properties. The maxima of the lobes for bright molecules are replaced by a node in the dark molecules. In the positive polarity STM images, the contrast difference between the tautomer forms is quite small and hence difficult to distinguish.

[(a)] the molecular structure is also described in chapter-1

Tautomeric interconversion

Under the influence of STM tip, H_2TPP is found to switch randomly from one tautomer form to another (bright$\rightleftarrows$dark) at 5K. As a result, in a STM image some molecules appear with a "cut" separating partial images of bright and dark states for the same molecule. The switching of the tautomer in either direction is random. The bright and dark tautomers appear as two stable states for H_2TPP on graphene when imaged at low current setpoint. By increasing the tunneling current, more instances of molecules switching are observed. To study this behavior, we perform I(t) spectroscopy at a fixed voltage and record current as a function of time.

The difference in the image contrast or tunneling conductance is more pronounced at the maxima of the two lobes that is observed in bright tautomers. In a time trace of the tunneling current, the tautomerization is evidenced by random transitions between two discrete levels of current, corresponding to a telegraph signal. This measurement is performed by parking the STM tip on the molecule and then the feedback is opened which then maintains a constant height during the measurement. The tip-sample height being determined by the tunneling current and voltage setpoint. In fig-3.5 (a) the time plot of tunneling current for various bias voltage are shown. We analyse the telegraph signal by measuring the duty cycle, switching frequency, and yield which are defined hereafter.

Duty-cycle: The time spent on upper and lower levels in telegraph signal corresponds to the lifetime of the tautomer. The bright form is characterized by a higher conductance and hence this state relates to the upper level (for positive bias) while the lower level corresponds to dark state. For negative bias, the trend is reversed due to sign change since the magnitude of current is always higher for bright molecules. Corresponding current values for the two state are then referred to as I_b (for bright) and I_d (for dark state). Similarly, the average lifetime is represented as τ_b and τ_d. In a given time duration, the average τ values are obtained by dividing the sum of individual lifetime values with the total number of switching events (N_s) in that period..

Switching frequency(ν) is the inverse of average time spent in a particular state (bright or dark). We obtain two switching parameters, for a given time trace, corresponding to transitions from bright to dark (ν_b), and dark to bright (ν_d) conversions.

$$\nu_b = 1/\tau_b \qquad \text{and} \qquad \nu_d = 1/\tau_d \tag{3.1}$$

Yield, for a transition, is defined as the number of switches induced per electron. We calculate the total number of tunneled electrons by integrating the total current passed through the junction for the time duration of measurement. Similar to switching frequency, we get two yield values-*yield bright (Y_b)* and *yield dark (Y_d)* given by the following expressions:

$$Y_b = \frac{q}{I_b \tau_b} \quad \text{(yield bright)} \qquad Y_d = \frac{q}{I_d \tau_d} \quad \text{(yield dark)} \tag{3.2}$$

The concept of yield is quite effective in comparing the switching rate of tautomers as it relates with the efficiency of the process. In the time dependent current measurement, the switching of tautomers are identified with various lifetimes and number of switching events. For illustration, the time traces corresponding to H_2TPP on pristine graphene (C-site) is presented for negative (fig-3.3) and positive (fig-3.4) bias. The current setpoint is constant at 100 pA for the recording and voltage is varied.

In fig-3.3, the bias voltage is varied from -1.15 V to -1.8 V as the HOMO of the molecule lies around -1.4 V.[92] The recording of tunneling current (100 pA) starts from the bright state of molecule. Consequently, the dark state has a lower current value after switching. For H_2TPP on C-site, the current in dark state lies between 10-15 pA. However this value is affected by z-drift of the piezotube in measurements since the feedback is open for the spectroscopy measurement. In the current time (*I(t)*) plot, the recorded graph is presented in absolute values so that the upper level always correspond to the bright state and lower level as dark state. For the analysis of this telegraph signal, the raw I(t) data is first fitted with a discrete two-level graph (red curves). The fitted plot is then separated into bright and dark data vectors to calculate I_b, I_d, τ_b, τ_d, N_s, and Yield values.

It is evident from the time plot (3.3) that the number of switching events increases with magnitude of bias voltage. These effects are better visualized by calculating the yield parameter as a function of bias voltage. Similar to this graph, collection of I(t) trace for positive bias (range: 1.6 to 2.5 V) is shown for the same H_2TPP molecule, in fig-3.4. The LUMO state of the molecules lies around 2 V for H_2TPP on C-site.[92] At positive bias, the switching of molecules is observed as a multilevel system for bias above 1.9 V. Below this value, the difference in the conductance states for bright and dark forms are very less and appears as small modulation in the tunnel current. The range for current in y-axis is the same for all stacked plots, for visual comparison. Fitting of a simple 2-level telegraph plot for these plots is slightly difficult given the presence of multilevel states in high bias measurements and small conductivity difference for low bias measurements.

To analyse this data set, we identify an average yield parameter and name it as global yield (Y_g). For calculating Y_g, we count the total number of electrons in the entire time plot (all states) and total number of switching events in time trace. The global yield which is the number of electrons required to induce one switch, is then expressed as

$$Y_g = \frac{N_s}{I_t \Delta t} \tag{3.3}$$

where Δt is the sampling time interval for I(t) measurements (usually 5 ms) and the parameter I_t is the sum total of all current points measured for the entire duration.

The yield of the switching process for the data shown in fig-3.3 and 3.4 is presented in fig-3.5(a). Along with yield, the STS on the molecule, on which these measurements have been performed, is also plotted for comparison. The voltage range for telegraph measurement is based on the STS of H_2TPP on graphene. We see in 3.5(a) the HOMO - LUMO positions which correspond to -1.3 V and +2.1 V, respectively. The switching between tautomers is negligible in the energy gap.

The magnitude of yield increases by orders of magnitude around the HOMO position. Here, the black circles and red squares represent Y_d and Y_b, respectively. At negative bias, both Y_b and Y_d are seen to increase sharply for voltage around -1.4 V, and then saturate beyond this value. Comparing with the STS plot, this saturation point coincides with the HOMO level (-1.3 V) of the molecule. Similar trend for yield saturation (global yield) is seen for positive bias, and is close to the LUMO state (2.1 V). It is striking to see that the voltage dependence of the yield is not symmetric with respect to zero bias. This is in sharp contrast with what has been reported so far in STM induced tautomerization.

For negative bias data, it is observed that Y_d is always greater than Y_b which means that the chances for a dark-to-bright switching is higher than the reverse. Further, after crossing the HOMO and LUMO energy levels, the magnitude of yield appears to saturate between $10^{-9} - 10^{-10}$.

The increase in yield (switch/e^-) could also be influenced by an increase in the number of tunneling electrons due to the increasing bias even though current remains constant, as seen in fig-3.5(a). To understand the effect of the number of tunneling electrons, similar experiment as a function of current was performed. The plot in the left, fig-3.5(b), show the yield as a function of current taken at constant bias of -1.5 V (i.e. above the HOMO level). Interestingly, it is observed that the yield stays almost constant with current, as compared to yield as a function of voltage. This suggests that the yield remains independent of the number of electrons that are sent across the tunneling junction. The number of switching event would increase with tunneling current but the number of electrons required for one switch remains the same.

Interpretation

From these measurements, it is shown that the yield for tautomerization process is pinned to the resonant states of H_2TPP molecule on pristine graphene surface. This implies that the switching of H-atoms takes place througth resonant tunneling of electrons through frontier orbitals. Typically, tautomerism in porphycene and phthalocyanines have been observed to be activated by inelasting tunneling of electrons (see table 1.2 in ch-1). In this framework, the increase in

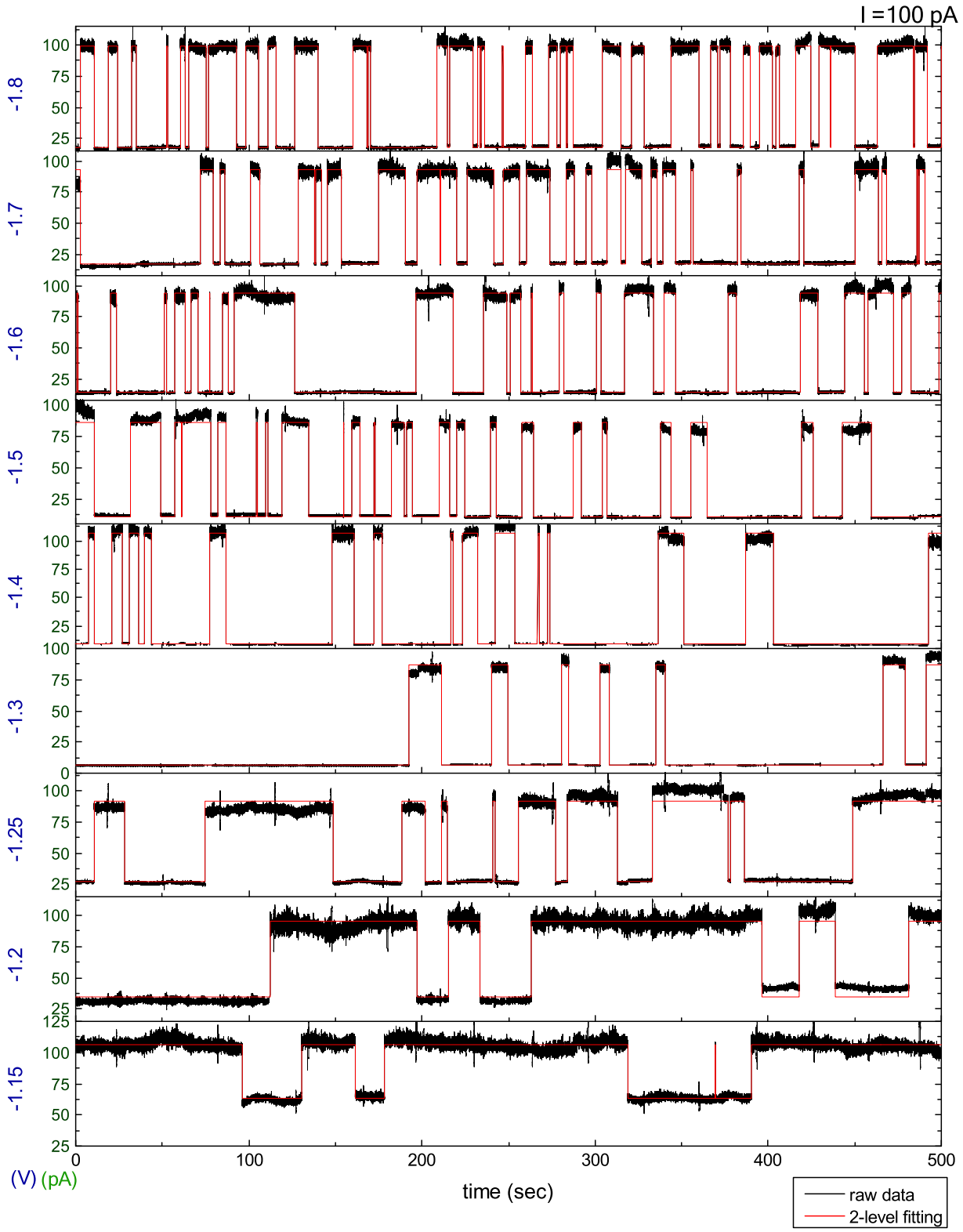

Figure 3.3: Telegraph signal in negative bias: Time dependent current plot showing the two-level conductance states of H_2TPP on graphene. Bottom to top shows the current measurement as a function of bias voltage from -1.0 V to -2.0V. The red lines are fitted telegraph signal for analysis.

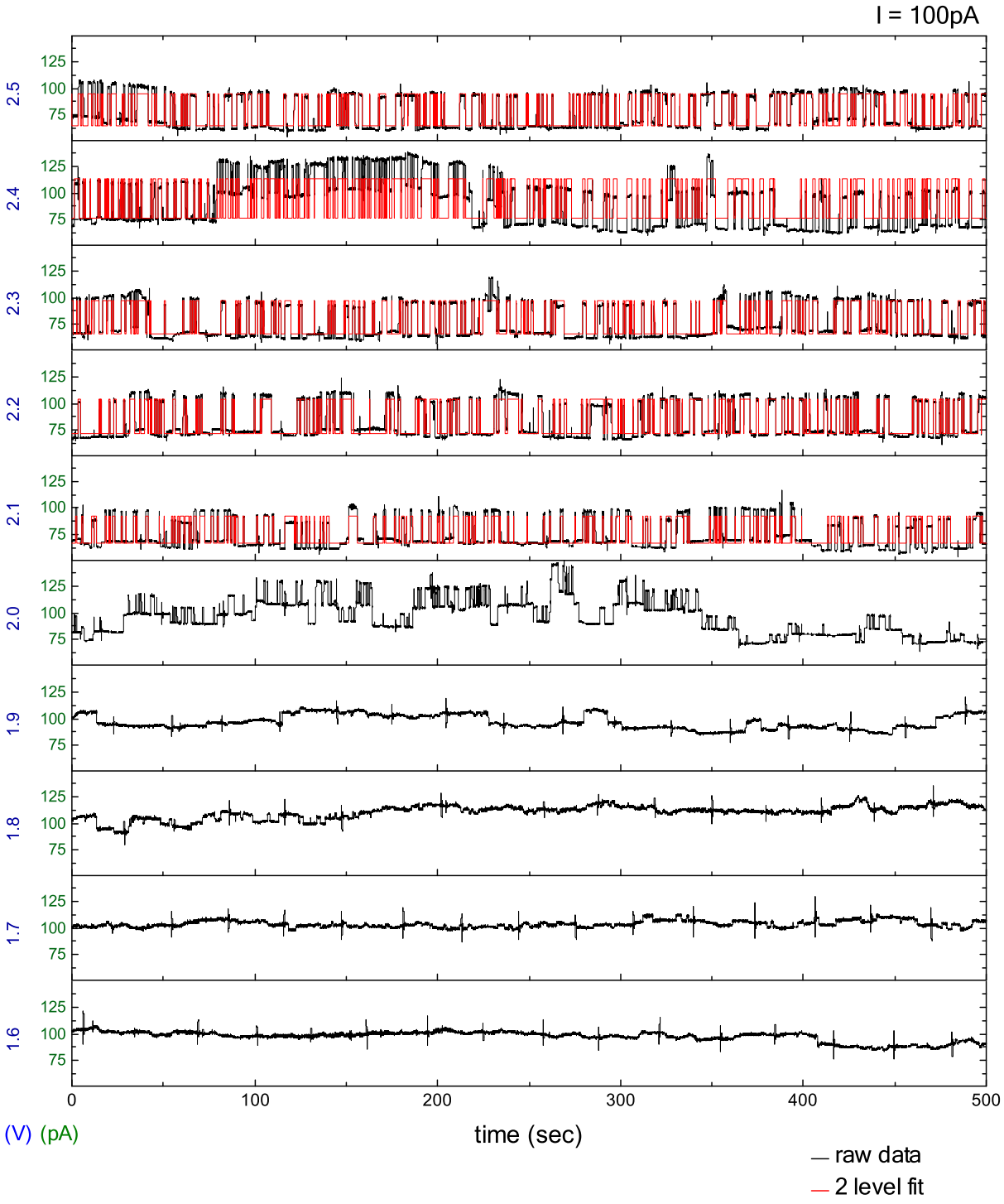

Figure 3.4: Telegraph signal in positive bias: Time dependent current plot showing the multi-level conductance states of H_2TPP on graphene. Bottom to top shows the current measurement as a function of bias voltage from 1.5 V to 2.5V.

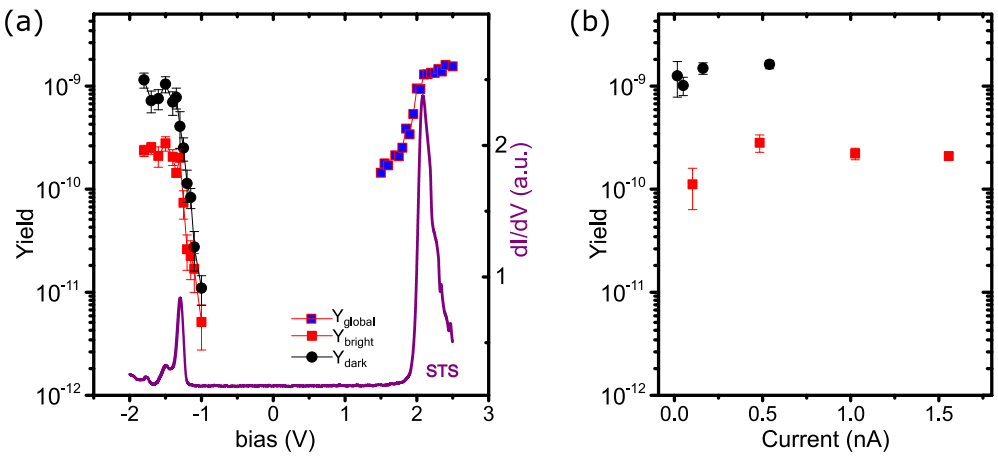

Figure 3.5: Tautomeric switching of H_2TPP on pristine graphene (a) Yield of the switching process as a function of bias voltage. The STS is plotted in the same figure for observing trends with respect to HOMO-LUMO state of the molecule. (b) Yield as a function of current, measured at -1.5 V. The y-axis on the two plots have the same range to compare the yield values.

yield is symmetric with respect to Fermi level. In a general approximation, the typical range for threshold voltage lies in few hundreds of millivolts which marks the onset of switching process. Tautomerization, here, is argued to be induced by vibrational excitation through an inelastic electron tunneling process. These experiments have also been performed with single molecules at 5K and find theoretical calculations in good agreement with the results. Takashi Kumagai et. al have extensively studied the porphycene molecule and been able to switch between tautomers using light and thermal annealing which further supports the explanation of vibrational excitation.

In simpler words, a threshold minimum amount of energy is required to cross the activation barrier in order to observe tautomerism independently of the sign of the bias voltage. But that is clearly not the case here. The observable signs of H_2TPP switching can be seen to start from -1.0 V for negative bias and around 1.5 V in positive bias. These energy values are sufficiently high for an isomerism reaction that usually requires very less activation energy. But for the sake of argument, let's assume that these *asymmetric* energy positions are related to the vibrational excitation of molecules. Quite unlikely but one can even find probable reasons to support these arguments such as changes in conformation of pyrrole groups or presence of weakly coupled graphene substrate, which eventually requires more vibrational energy to induce switching at low temperatures. However, it does not explain the saturation of the yield below and above HOMO - LUMO levels, respectively. It is quite clear that the concept of threshold energy doesn't fit in the switching mechanism through resonant tunneling.

Here, we propose a mechanism for induced tautomerism based on resonant tunneling. The first step is a transition to a transient charged state of the molecule when molecular orbitals are in

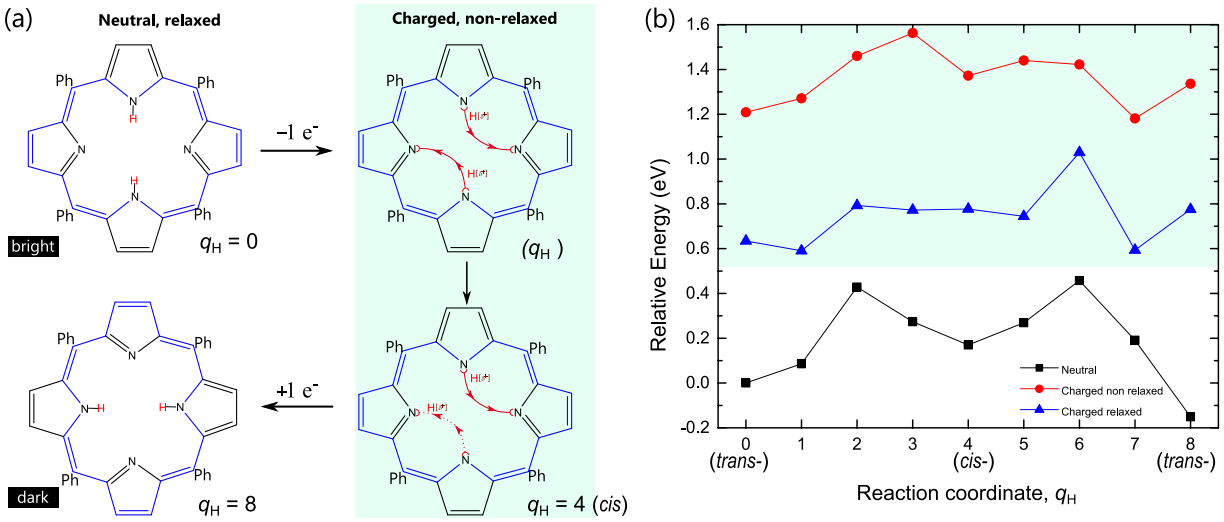

Figure 3.6: Energy landscape of tautomerization (a) Intra-cavity movement of H-atoms at HOMO resonance level. (b) Difference in total energy of the molecule during the tautomerization process as a function of the H-coordinate.

resonance with Fermi level of the tip. This process would lead to loss of an electron from HOMO state and electron gain at LUMO. For calculations, we have considered the switching process at the HOMO energy level. Assuming a transition following the Franck-Condon Principle, the molecule is first brought to a non relaxed charged state. The relaxation of the molecules then proceeds in parallel with the movement of protons in the cavity, in order to convert to another tautomer form or fall back to its initial state.

In fig-3.6(a), these steps are demonstrated where we start the neutral (bright) molecule which gets ionized and is in a *charged-non relaxed* configuration. The molecule then passes through an intermediate state (-*cis* configuration[(b)]) to finally decay into a neutral and relaxed tautomer form. It is also possible that the molecule end up in the starting configuration.

$$trans(\text{bright}) \rightleftarrows cis \rightleftarrows trans(\text{dark}) \tag{3.4}$$

In order to understand the excitation mechanism of tautomerization, DFT calculations have been performed by Yannick Dappe at CEA Saclay. The tautomerization energetic barriers of the neutral and charged molecules have been determined using the localized orbital basis set DFT code Fireball.[138] In both cases, a 15×15 unit cell of graphene has been used with the H_2TPP molecule on top. In the case of the neutral molecule, the structure has been first optimized, and then the tautomerization energetic barrier has been determined by calculating the total energy of the system for different configurations of H atoms, following the minimal pathway described

[(b)]two hydrogen atoms can lie on opposite pyrrole groups, identified as -*trans* configuration or on adjacent pyrroles referred to as -*cis* configuration.

in the work by Maity et al.[139] Regarding the charged molecule, the HTPP molecule on graphene has been calculated first, and added an H+ atom following the same pathway. This yields the energy barrier for the non-optimized molecule on graphene. To determine the energy barrier after optimization, once again we have first optimized the HTPP molecule on graphene, and again added the H+ atom for the different configurations. The movement of H-atoms is identified as the reaction co-ordinate for the switching process.

The calculated total energies for charged and neutral states for H_2TPP are plotted in fig-3.6(b). For neutral molecules (square plot), the stable tautomer forms in the energy curve can be seen for positons, $q_H = 0$ (bright) and $q_H = 8$ (dark) with a local minima for -*cis* configuration ($q_H = 4$). On charging, the molecules ends up in an excited state, the energetic landscape is shown in top curve (diamand plot). In this non-relaxed state, the barrier for tautomerism is still high so the molecules decays to a more relaxed configuration with less energetic barrier, shown in the middle plot (triangles). In this state, the intermediate $-cis$ configuration has higher total energy compared to *bright* or *dark* forms, subsequently it can proceed for another tautomer form or fall back to the original form. We also find an asymmetry in the three energy profile suggesting that the rates of tautomerization are dependent on the starting form of molecule.

We have shown that the onset of tautomerization is marked by the position by the frontier orbitals, on pristine graphene. The HOMO-LUMO energy position for H_2TPP is known to shift on N-doped graphene substrate.[92] In the context of tautomerization, the switching yield for H_2TPP molecule atop N-site has been studied, and detailed in the next section.

3.2 Porphyrin on N-doped graphene

Nitrogen dopants behave as electron donors to the graphene lattice by increasing the overall charge carrier density of the graphene lattice.[140] In STM images, the dopants[(c)]are observed as triangular points having comparatively higher LDOS than surrounding carbon atoms. A high resolution topography image obtained at constant current is shown in fig-3.7 showing randomly distributed N-atoms in the lattice. The underlying moiré pattern of the graphene layers can also be seen very clearly.

Porphyrin molecules self-assemble on N-graphene in a similar way as seen for pristine graphene (fig-3.1). In fig-3.8(a), monolayer of H_2TPP is shown (1.8V, 20 pA) on top of N-doped graphene substrate. We find partial coverage of graphene surface and the molecular aseembly is seen to terminate at the grain boundary. The contrast in STM image (or the LDOS) of some molecules in this packed assembly are observed with higher values. These molecules have been found to sit atop N-dopants in the substrate.

[(c)]for N-atoms, the term 'dopants' and 'defects' are used interchangeably in this chapter.

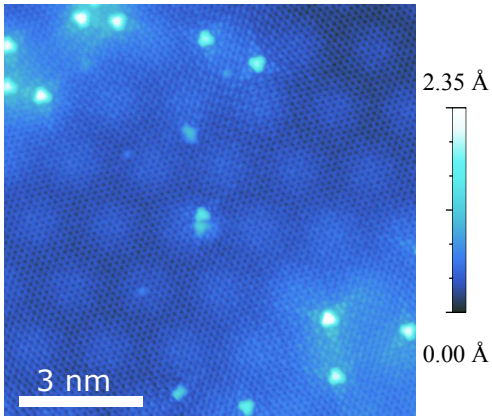

Figure 3.7: STM image of nitrogen dopants in graphene lattice taken at 0.2 V and 1 nA

In order to verify the presence of nitrogen atoms below the molecule, this molecular island was swept away by repetitive STM imaging using a voltage bias of 0.5 V and 400 pA. The image obtained after this procedure is shown in fig-3.8(b) revealing the graphene layer beneath the molecules. The grain boundary and the distribution of defects can be compared in 3.8(a)("before") and 3.8(b)("after") images. These two images were taken at identical tunneling setpoint (1.8 V and 20 pA) for comparison.

Further, the image of the substrate is superimposed on the molecular assembly and shown in fig-3.8(c), that serves as a visual guide to reveal the position of N-dopants below the molecules.

By comparing the STS on various molecules in this assembly, we find two categories of molecules. In one group, there are porphyrin molecules having similar spectra as that on pristine graphene surface suggesting that these molecules lie on carbon atoms (C-site). In the second group, the molecules are identified by a shift in the STS for both HOMO and LUMO levels, due to the presence of N-defects below the molecule (N-site). The STS comparison for these two types of (*neighboring*) H_2TPP molecules is shown in fig-3.8(d) where the shift in energy levels can be clearly observed. The peak positions for the HOMO-LUMO state of H_2TPP on N-site is identified with a shift of 0.2 V moving deeper and away from the Fermi level. The STM image in the inset shows the N-site H_2TPP molecule and a neighboring C-site molecule marked with color dots showing the position where the spectra is taken.

The difference in the energy positions (fig-3.8d) can be correlated with a difference in contrast in a series of STM images shown in fig-3.9 In this collection, the top row comprises of images taken at positive bias starting from 2.2 V in the left to 1.3 V at the right. The row below is taken at negative bias from -1 V (left) to -1.9 V.

From STS in fig-3.8(d), we find the LUMO level for N-site H_2TPP (or N-H_2TPP) is around 1.9 V while for C- site (C-H_2TPP) it is 2.1V. Thus, the shape of molecules can be distinguished

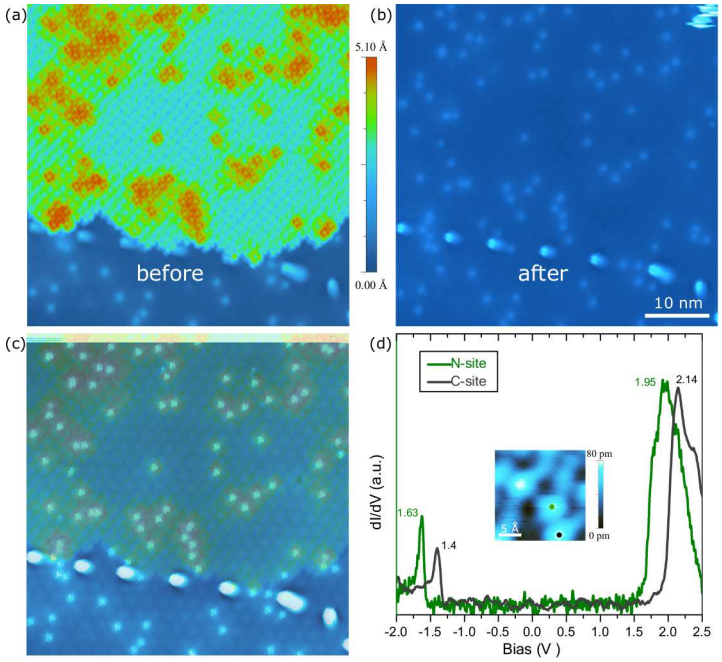

Figure 3.8: Adsorption site below molecular layer (a) STM topography showing a H_2TPP molecular lattice on N-doped graphene.(1.8 V, 20 pA) (b) Image showing the same area after removing the molecules.(1.8 V, 20 pA) (c) Superimposition of **b** on top of **a** correlating the position of nitrogen dopants with molecular lattice. (d) STS comparison of H_2TPP on N-site (green curve) and C-site (black curve). Inset show the position (green and black dots) on molecules where the spectra has been taken.

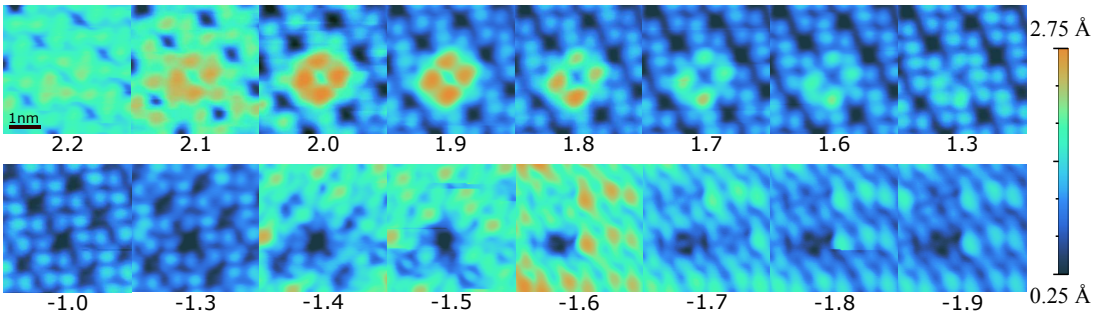

Figure 3.9: STM topography images of N-site H_2TPP molecule as a function of bias voltage. The top rows show images taken at positive polarity, and the bottom ones in the negative. The current setpoint is 10 pA for all images. Image area 4nm × 4nm.

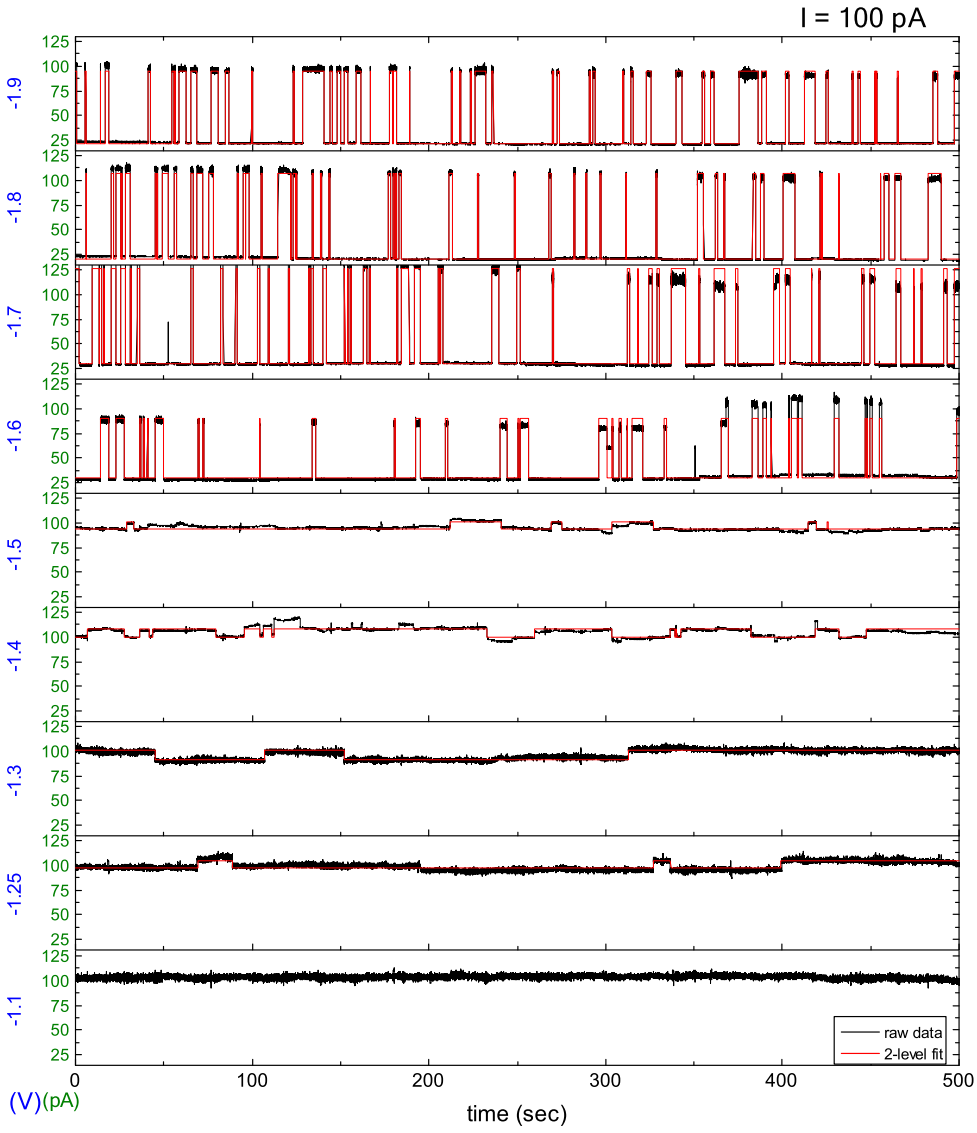

Figure 3.10: Telegraph signal in negative bias (N-Graphene): Time dependent current plot showing the two-level conductance states of H_2TPP on N-doped graphene. Bottom to top shows the current measurement as a function of bias voltage from -1.1 V to -1.9 V. Sampling time is 10 ms for each plot. The red lines are fitted telegraph signal for analysis.

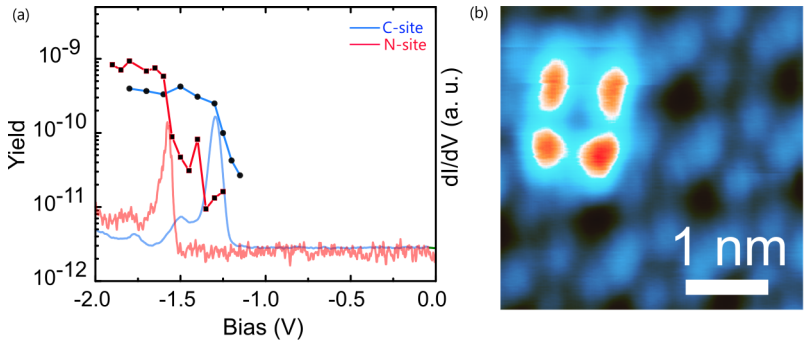

Figure 3.11: Yield as a function of orbital position (a) Switching yield of H_2TPP is compared atop N-site and C-site, co-plotted with corresponding STS. The yield is obtained as a function of bias voltage at constant current of 100 pA (b) STM topography image showing the H_2TPP molecule in a monolayer surrounded by C-site molecules. (1.8V, 100 pA)

by recording topography image at intermediate bias voltages. In the positive bias, the shape of N-H_2TPP can be identified in the molecular lattice for bias voltage upto 2.0 V, and can be clearly seen in the images. Similarly, molecules can be identified in negative bias based on energy position for HOMO levels. In this polarity, the HOMO of C-H_2TPP is visible at lower bias voltage (-1.4 V) while N-H_2TPP appears with a darker contrast. Above -1.6 V (HOMO on N-site) the bright form for both molecules have the same shape and can be seen in the inset of fig-3.8(d).

Tautomerization in N-site porphyrin is observed in the same way as seen on pristine graphene substrate, with characteristic bright and dark forms. Since the nitrogen dopants are randomly distributed in graphene lattice, we only observe single molecules or small clusters that are adsorbed on top of it. These can be seen in fig-3.8(a), as well as the cover image of this chapter. The switching process for N-site molecules are analyzed as described in the previous section.

In a molecular lattice, we choose a N-H_2TPP molecule that is surrounded by C-site molecules. The STS on this *single* N-site molecule (in the 2D molecular lattice) is compared with neighboring molecules, to observe the difference in peak position for frontier orbitals. Subsequently, the telegraph signal is recorded as a function of bias voltage from -1.1 V to -1.9 V and analyzed to calculate the yield of the switching process. Here also, we start from the bright form of the tautomer at constant current setpoint of 100 pA. The time dependent data is shown in fig-3.10. On the I(t) plots, the fitting of telegraph signal is displayed in red trace.

From the time trace, we can see that the switching frequency increases rapidly around -1.6 V which corresponds to HOMO state of N-H_2TPP. The global yield is calculated for this dataset and compared with that of C-site molecule. The results are shown in fig-3.11. The yield for N-H_2TPP increases until -1.6 V (red curves) and then saturates for higher bias voltage. We plot the STS in the same energy range to clearly identify the onset and saturation behavior for yield,

for both sites/substrates. The dependence of yield with energy position clearly demonstrates the pinning of switching process with molecular energy levels. From this comparative study, it is evident that switching of H-atoms in porphyrin macrocycle is activated by the resonant or elastic tunneling of electrons.

3.3 Control of the tautomerization process

3.3.1 Tautomers as molecular switch

Co-existence of bright and dark forms of tautomer for porphyrin suggests that these states are stable. Further we have demonstrated that they can be reversibly switched using appropriate bias voltage. These tautomeric forms are identified with distinct conductance values which can be exploited for implementing a simple logic function, for example, in the form of a *molecular switch*. The concept of a molecular switch on the basis of tautomerization has been demonstrated on isolated molecules but has not been observed in molecular lattice which is more relevant from technological point of view.

The switching behavior of H_2TPP are observed for both single molecules (on Au(111)) and for molecules in a 2D lattice (graphene). On graphene substrate, porphyrin molecules form close packed assembly and is found to be very stable, even when samples are kept at room temperature. Switching of tautomers can be induced by applying a voltage pulse that is slightly higher than the HOMO level of molecule (-1.5 V for C-site, -1.8 V on N-site). The conversion of one tautomer form to another can be observed by monitoring the amplitude of tunneling current over time. Once the conductance changes, the voltage pulse can be stopped and the molecule stays in the converted tautomeric form. With this procedure, the porphyrin molecules are manipulated individually to observe the stability of switched molecules, on pristine graphene substrate. For simplicity, these experiments are demonstrated on pristine graphene substrate as there are two types of H_2TPP molecules on N-graphene each having bright and dark forms which increases the complexity of the system.

Stability of tautomers

The ability of tautomers to remain in one particular form, under unperturbed conditions, would be the first criteria to judge for practical considerations. In the initial condition, the distribution of dark and bright forms of H_2TPP is quite random, as shown in fig-3.12(a), where the molecules can be found to switch while scanning specially when the tunnel bias is close to HOMO (or LUMO) level. Molecules can switch spontaneously and also due to the tip induced electric field. However, at 5K, it is not clear whether thermal equivalent energy can induce spontaneous switching of tautomers.

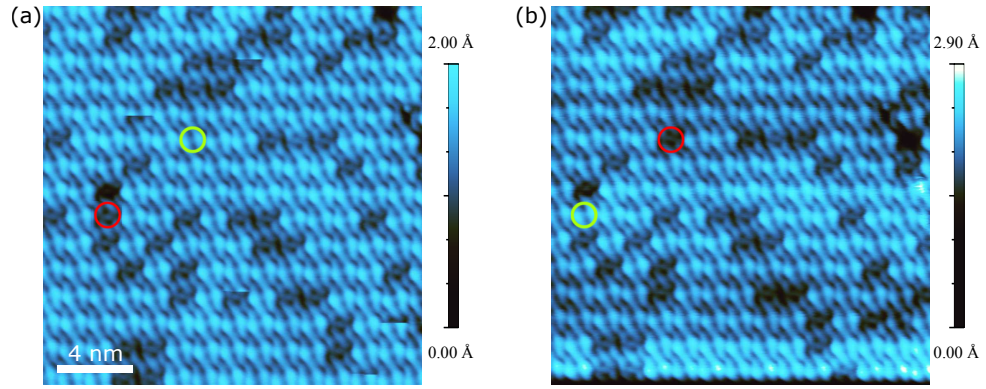

Figure 3.12: Stability of tautomers (a) STM topography image showing random distribution of bright and dark tautomers of porphyrin. Some molecules are also seen to switch while scanning. (b) The same area imaged after 15 hours with the tip far away from the sample (50 nm). Circles compare the change in tautomeric state of molecules. Both image are taken at -1.4 V and 10 pA.

In order to establish whether the tautomerization can occur spontaneous, we compared topography images for an area with large time gap between successive measurements. In fig-3.12(a), a molecular island is scanned at low perturbing setpoint (-1.5 V and 10 pA), thereafter the tip is retracted by 50 nm to reduce the electric field effect. The temperature had been kept constant to avoid any drift issues with the tip, so that the same area can be imaged afterwards.The sample is then approached with the tip after 15 hours and the first image that has been taken, is shown in fig-3.12(b).

It is clear from the distribution pattern of bright and dark molecules that the image in the right corresponds to the same area as shown in left. Comparing the distribution of bright and dark molecules, we find only 2 molecules out of approx. 400 molecules have switched. In the left image (a), it is observed that 4 molecules have switched while scanning and hence, it is possible that the two molecules that have different tautomeric form have also switched due to the influence from tip. From this observation, it is evident that spontaneous switching of tautomers is extremely rare, if not absent.

Locality and precision of switching

Tip-induced switching may also influence neighboring molecules when the molecule below the tip is being converted to other form. The neighboring molecules can be influenced by two different ways. Through electronic coupling depending on the strength of inter-molecular interactions and by the fringing effect of electric field around the tip

The locality of a single molecule switching can be observed in a molecular lattice which only one tautomeric form, as shown in fig-3.13. A region of 20 nm $\times$ 15 nm is converted into an *all bright state* by manipulating the states of all dark molecules that were present initially, and the

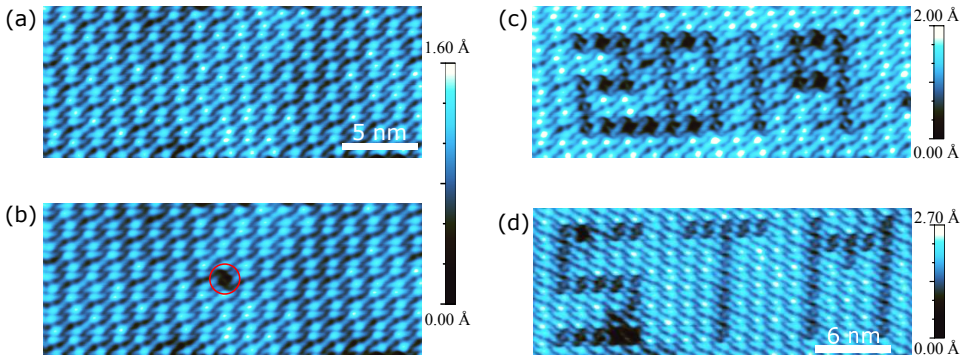

Figure 3.13: Single molecule manipulation (a) An area in porphyrin lattice with molecules set to bright tautomer form. (b) Same area after a molecule has been switched to dark tautomer form. (c) Writing **2019** on this area by manipulating tautomeric state of individual molecules. (d) The letters **STM** are produced with combination of bright and dark molecules, similar to **c**. All images have been taken -1.4 V and 10 pA

image is shown in fig-3.13(a). Subsequently, in this lattice, one bright molecule is converted to dark form and the STM image after this manipulation is presented in fig-3.13(b). The red circle in (b) shows the position of the molecule which has been switched to dark form. From the two topography images ((a) & (b)) we observe that the effect of the voltage pulse is confined to the switching of one molecule while neighboring molecules remain unperturbed. This demonstration suggests that the tip induced switching is a very localized phenomena.

Thus, switching of porphyrin molecules can be treated as fairly independent events due to a high degree of control and precision using STM tip. With such capabilities, constituent molecules of the lattice shown in fig-3.13(a) is manipulated so that a numeric pattern of *2019* can be *written* using dark molecules as pixels. The final figure obtained after a number of switching events required to make this pattern, is shown in fig-3.13(c). The manipulation or "writing" conditions are identified by tunneling parameters of -1.5 V and 100 pA (or even higher) whereas the "reading" or imaging conditions are -1.4 V and 10 pA. Since the bright and dark forms are clearly distinguished at the HOMO energy level, the reading and writing parameters are very close. However, a lower tunneling current setpoint acts as non-perturbative reading mode for observations without changing the state of molecules. In the same spirit, we also demonstrate the writing of "**STM**"in fig-3.13(d) in a different area.

3.4 Conclusions

The control of the movement of hydrogen atoms inside the porphyrin macrocycle has been demonstrated on pristine and nitrogen doped graphene, at 5K. In H_2TPP, there are four nitrogen center in the inner core and two of them have covalently bonded hydrogen atoms. The location of

H-atoms can be changed by the application of a voltage pulse from the STM tip, typically lasting few seconds, which leads to hopping of H-atoms to the nearest nitrogen centers. This transfer is accompanied by a rearrangement of pi electrons in the molecular framework, commonly known as tautomerism. Experimentally, two stable tautomeric forms of porphyrin are identified on graphene substrate with characteristic tunnel conductance appearing as bright and dark in STM topography image. This intramolecular switching of hydrogen atoms appears to occur reversibly at 5 K and without any structural deformation of the molecular lattice.

Rate of switching and the transition probability into the other tautomeric state are found to be different for the bright and dark form of porphyrin molecules. The number of switching events are found to increase linearly with the tunneling current so in terms of number of switch per electron (or yield), this is independent of the magnitude of current. However, this value of yield is found to depend strongly on the molecular orbital energy levels. This observation is enforced with N-doped graphene substrate where the HOMO-LUMO levels of H_2TPP are shifted and the plot of yield as a function of bias voltage also follows the same trend. Resonant tunneling of electrons through molecular orbitals is identified as the excitation mechanism for the tautomerization in porphyrin/graphene system. This is in stark contrast to the more commonly observed for tip-induced tautomerization in single molecules where the activation energy for proton transfer is provided by the inelastic tunneling of electrons. In that case, the plot of yield is always symmetric with bias voltage and not pinned to the molecular energy levels which is clearly different from the work presented in this chapter.

Further, through the precise control over the tautomer state of individual porphyrin molecules, the molecules are employed as molecular switch identified by bright and dark states to store alphanumeric information. It is important to note that this information can be changed on the same area and thus resembles a form of re-writable memory. In an ideal approximation, the storage density is almost 6 times more than the commercially available 14 nm node technology for memory chips.

Chapter 4

Interaction of electron acceptor F4-TCNQ molecules with Graphene

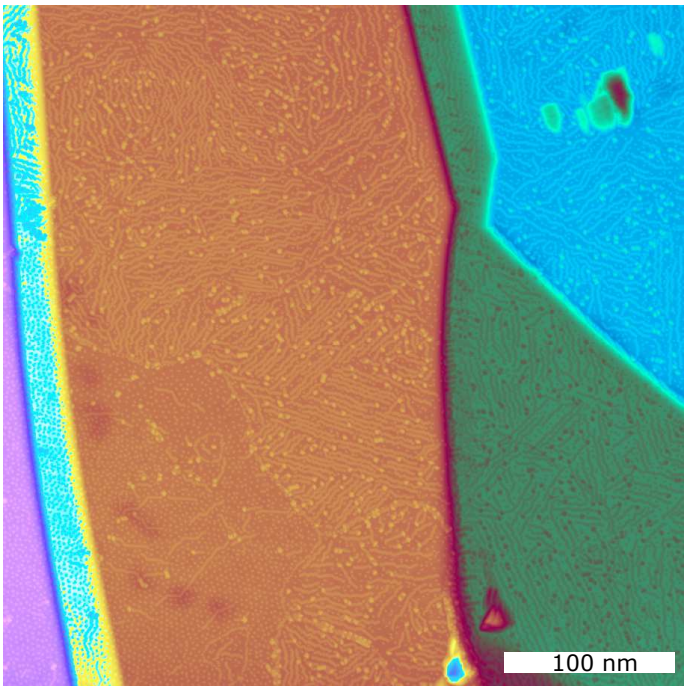

We have studied electron acceptor F_4TCNQ molecules on pristine and nitrogen-doped graphene. The influence of moiré superstructure on the distribution of molecules at the surface evidence the role of molecule-graphene interaction on molecular organisation. The electronic properties of adsorbed molecules are discussed based on STS measurements revealing molecular orbital resonances and charging peaks.

4.1 Isolated molecules at low concentration

On pristine graphene, as evaporated F_4TCNQ molecules show stronger interaction as compared to TCNQ molecules[119] for example, allowing us to observe single molecules on graphene. After molecular deposition [(a)], the molecules are found as aggregates on the surface. The STM images shown below compare the organization of molecules before and after room temperature annealing. The following sections detail the behavior and electronic properties of F_4TCNQ on pristine and N-doped graphene.

4.1.1 On pristine graphene substrate

Figure-4.1(a) shows an area on pristine graphene covered by a sub-monolayer of F_4TCNQ, taken just after deposition with the sample maintained at low temperature. In this image, the molecules appear asymmetric with a part that is brighter indicating that they are not flat but inclined or standing with respect to the graphene surface. Few single molecules are also seen to be moving under the influence of the STM tip and are therefore not stable enough to be studied.

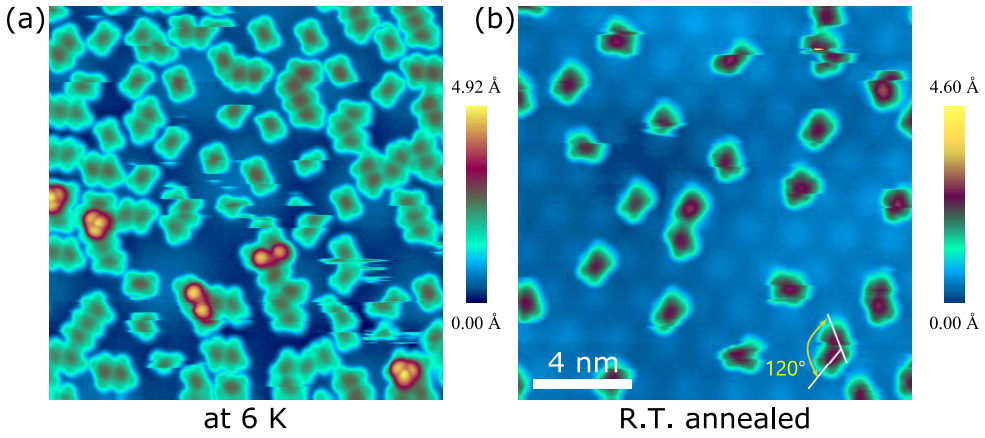

Figure 4.1: Surface density of F_4TCNQ molecules (a) just after depostion (sample kept at 6 K) and, (b) when the sample has been annealed to room temperature. Imaging parameters: 2.0 V, 10 pA

In order to obtain a stable arrangement of molecules on graphene, we have annealed the sample to room temperature for few minutes. The image in fig-4.1(b) shows the distribution of molecules after annealing. It can be seen that the concentration of molecules has been drastically reduced, in a rough estimate by as much as 20 times. This reduction is observed throughout the sample and points to an overall loss in surface density. Therefore, the room temperature annealing has lead to a diffusion of molecules on the surface allowing for reorganisation as well

[(a)] sample stage is maintained at 6 K during evaporation, details of the evaporation process can be found in chapter-2.

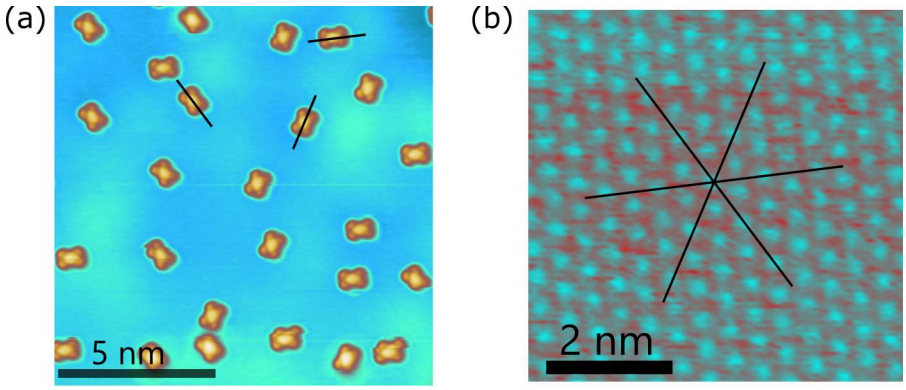

Figure 4.2: Molecular alignment(a) STM image of F_4TCNQ molecules on pristine graphene. (b) STM image of atomic resolution on the same graphene domain as in (a). The lines indicate the armchair axis of the graphene atomic lattice.

as a loss of molecules on graphene flat areas. The origin of reduced density of molecules could be either due to desorption or trapping of molecules at rough domain edges. The remaining molecules are separate single molecules in contrast with some molecules previously studied such as porphyrin or TCNQ that form compact islands[92,119]

We find three orientation axis for the molecules on graphene in a given domain. These directions follow the graphene rotational symmetry of 60° giving rise to three directions along which the molecules are aligned. Comparing STM image of molecules on a graphene area with atomic resolution image on the same domain, it can clearly be seen that the moleucles adsorb with their axis aligned along the armchair direction of graphene as shown in fig-4.2.

The molecules can also be displaced unintentionally during scanning in the same way as we observed for as deposited molecules on the cold sample. After such motion, the molecules keep one of the three directions and no intermediate orientation is observed, which emphasizes that these configurations are clearly the most stable ones. Theoretical calculations also predict that F_4TCNQ prefers to align along the *arm-chair* direction compared to the *zig-zag* direction.[117,118,141]

Next, we study the spectroscopy of isolated single molecules on pristine and N-doped graphene substrates. The STM and STS of molecules on pristine graphene is presented in fig-4.3. In order to identify the structure of graphene below the molecules, we removed the molecule by tip manipulation after measurements.

In fig-4.3(a) and (b), an area of pristine graphene with two moire domains can be seen which is separated by a grain boundary. This area is populated by very low density of F_4TCNQ molecules which are found to be stable during scanning. After recording the STS, these molecules were removed and the underlying adsorption sites were found to be point-type defects, as seen in the

[(a)] For F_4TCNQ, typical setpoint values of 500 pA and 0.5 V were used for this operation.

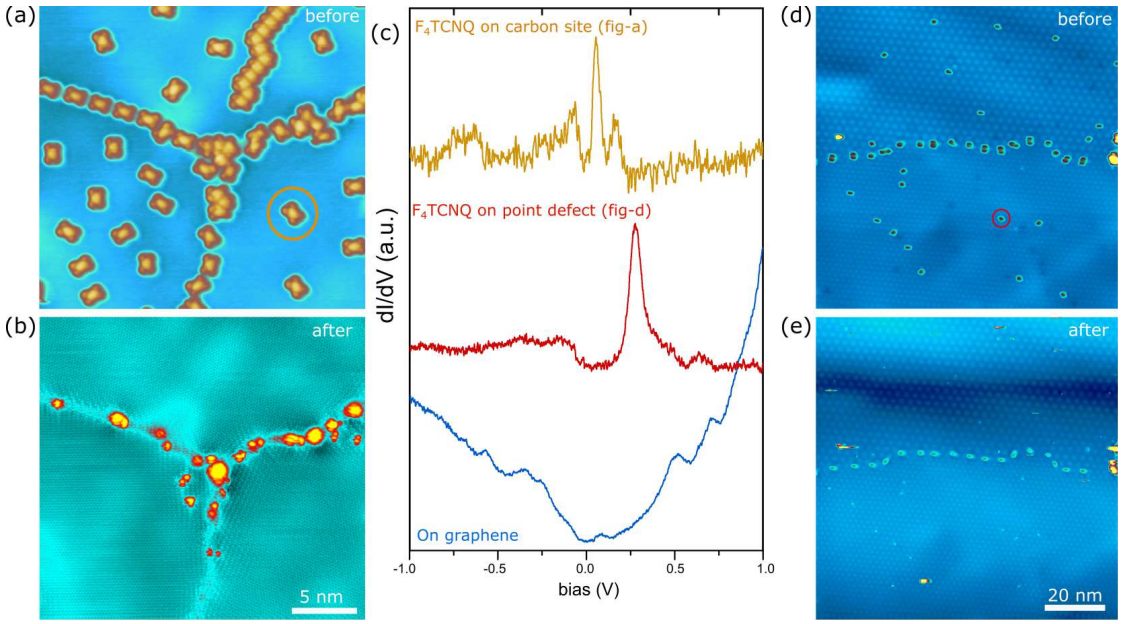

Figure 4.3: F_4TCNQ on pristine graphene: (a) STM image of molecules adsorbed on flat graphene lattice and on grain boundary (2V, 10 pA). (b) Same area as in (a) after removing the molecules revealing the substrate underneath (2V, 100 pA). (c) STS measurement of F_4TCNQ on graphene lattice (C-site) and point defect, shown with spectrum on graphene. The molecules have been encircled on which spectra was recorded. Before (d) and after (e) image of graphene domains where F_4TCNQ is adsorbed on point defects (2V, 10 pA).

image 4.3(b). The grain boundary region is decorated by molecules adsorbed on both sides, forming pair-like structures. Since the nature of interaction is difficult to understand for these sites, we focus only on homogeneous flat areas on graphene lattice.

In this area (4.3a), molecules fill all the defect positions and grain boundary regions and only additional molecules can sit on the carbon lattice. This is showing that grain boundaries and intrinsic point defects in graphene act as trap for diffusing molecules. The topography image in fig-4.3(a) shows molecules on graphene with domains separated by grain boundary. The grain boundary is lined by closely spaced F_4TCNQ molecules adsorbed on it. In this area, STS on different molecules were recorded and removed afterwards using high current setpoint. The image after removing the molecules (fig-4.3b) reveals that there is no point defect below the molecules that were observed in this area. Thus, the STS taken on molecules away from the grain boundary correspond to those adsorbed on carbon site, and a representative plot is shown in fig-4.3(c).

The spectrum shows sharp peaks close to E_F at -62 mV and 54 mV and 155 mV. Given the weak coupling of F_4TCNQ with graphene, the tunneling parameters (tip-sample distance) had to be adjusted to record the spectra so as to not perturb the positon of molecule underneath. Thus, the constant current images and the spectroscopy have been optimized at 2V and 10 pA. Due to this low current setpoint used in the STS measurement, the peaks are barely evident amidst

the background noise. However, we have performed repeated measurements on more than 50 molecules spanning a large macroscopic area to confirm the presence of these peaks close to fermi level. With lower tunneling current also comes the issue of poor intramolecular resolution in the topography image. It is still possible to resolve intra-molecular features in the topography such as lobes centered around the cyanide groups of F_4TCNQ and a central elliptical lobe, in fig-4.3(a).

In contrast to molecules on C-sites, the molecules on defects remain stable while scanning which shows that molecule-graphene interaction is stronger at defect sites. Representative STS on a molecule atop a point defect (encircled in red in 4.3d) is presented in fig-4.3(c) (red curve). This dI/dV spectrum shows features near E_F, a shoulder type feature at -0.1 V and a peak at 0.27 V. While all molecules adsorbed on these defect sites show similar features in their spectrum, the energy position for some molecules vary slightly due to small differences in the adsorption geometry. Thus, the STS is characteristic of the adsorption site of F_4TCNQ molecules.

Molecular orbitals

We investigated the molecular orbitals of a molecule on carbon site on a flat pristine graphene area. In fig-4.4(f) we show the spectra measured on a molecule on carbon site, in absence of any defect. Each STS trace is an average of 20 individual measurements at a given spot. As mentioned above, slight modification of spectra are observed from one molecule to another, as can be seen from the difference between spectra of fig-4.4(f) and of fig-4.3(c). However the main features reported previously are still observed with one peak at negative bias and two peaks at positive bias. A careful examination of the spectra show that the energy of the two first peaks at positive and negative bias varies depending on the position of the tip on the molecule. These energies vary from -150 mV (+100 mV) at the center of the molecule to -100 mV (+70 mV) at the edge of the molecule. Such effect has been discussed in the case of pentacene on insulating film and attributed to inelastic tunneling effect that shifts the apparent resonant peak to higher energy in the center of the molecule.[142] In order to identify the states corresponding to the two frontier peaks we performed constant height STM images which are reported in fig-4.4. The images in fig-4.4 (a) and (b) show molecular shape in the negative bias polarity at -150 mV and -100 mV. Similarly, the images shown in fig-4.4(c) and (d) are taken at positive bias: at 70 mV and 100 mV, respectively.

First, we compare the molecular shape in the STM topography image in both polarities. A schematic of F_4TCNQ molecule is shown on the right of 4.4(a) to serve as visual aid for the features seen in STM topography. Here, the constant height images have been taken close to Fermi level therefore, we can assume to a good approximation that it is similar to that of a dI/dV image. The molecular shapes look equivalent for -150 mV (a) and -100 mV (b) suggesting

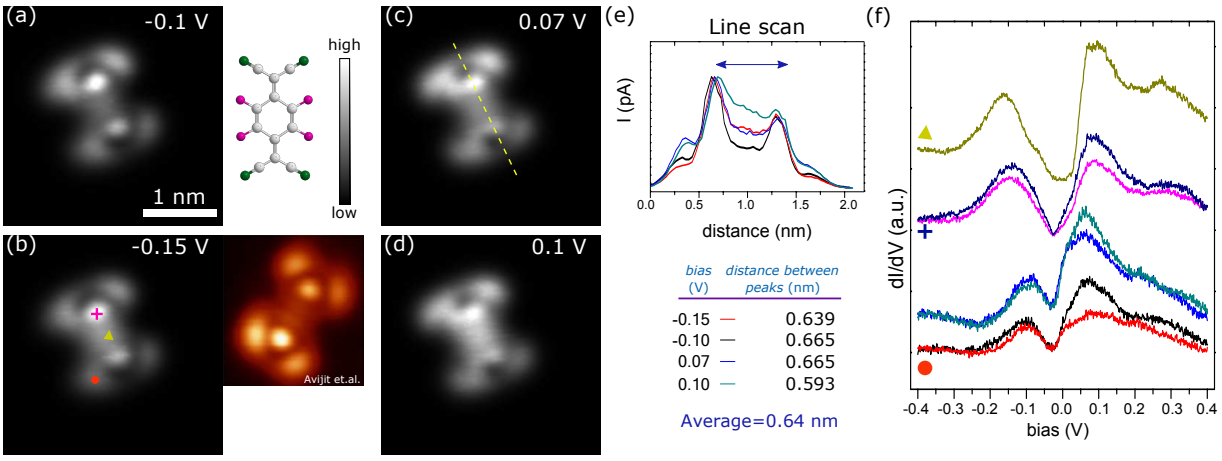

Figure 4.4: F_4TCNQ molecular shape: Constant height topography at (a) -100 mV (b) -150 mV (c) 70 mV (d) 100 mV. Image on the right of (b) is taken from Avijit et.al. showing the LUMO of molecule on Gr/Ir(111). (e) Line scan comparison for (a)-(d) at the position marked by yellow dashed line in (c). A table showing the peak-peak distance corresponding to the line scan. (f) STS on the molecule at different position in the molecule, the *circle, plus* & *triangle* markers denote the position of measurement corresponding to four outer lobes, two inner bright lobes and the center of the molecule, respectively.

that they are the same orbitals. We compare this result to an earlier work done by Avijit et.al. for F_4TCNQ on epitaxial graphene (SLG on Ir(111)).[78] The constant height dI/dV map of a single F_4TCNQ molecule from this study is presented on the right of fig-4.4(b) which is strikingly similar to our topography images. Comparing these two results, it is clear that the LUMO level of the molecule is seen in fig-4.4 (a) & (b).

Further, the images at positive bias (4.4 (c) & (d)) appear very similar to those at negative bias. For illustration, line scan profile passing through the long symmetric axis of the molecule are shown for all four images in fig-4.4(e). For reference, we focus on the position of two peaks which corresponds to the inner bright lobes in the images. These lobes are located close to the carbon atom that links the two cyanide groups (on each side) to the central benzene ring. In the line scan comparison, we observe that the maxima of the lobes are at the same position with an average distance of about 6.4 $\AA$ (see table in fig-4.4). Thus, we observe the *same* molecular orbital at both polarity and we identify this orbital to be the LUMO state.

Since the LUMO energy of the F_4TCNQ in gas phase lies deeper than the fermi level of pristine graphene (see section1.3), it is expected to observe the LUMO below the fermi level of the system. The observation of a double peak for the LUMO state at both negative and positive bias suggests that the LUMO splits into two states that could be attributed to a singly occupied state (SOMO) and singly unoccupied state (SUMO).

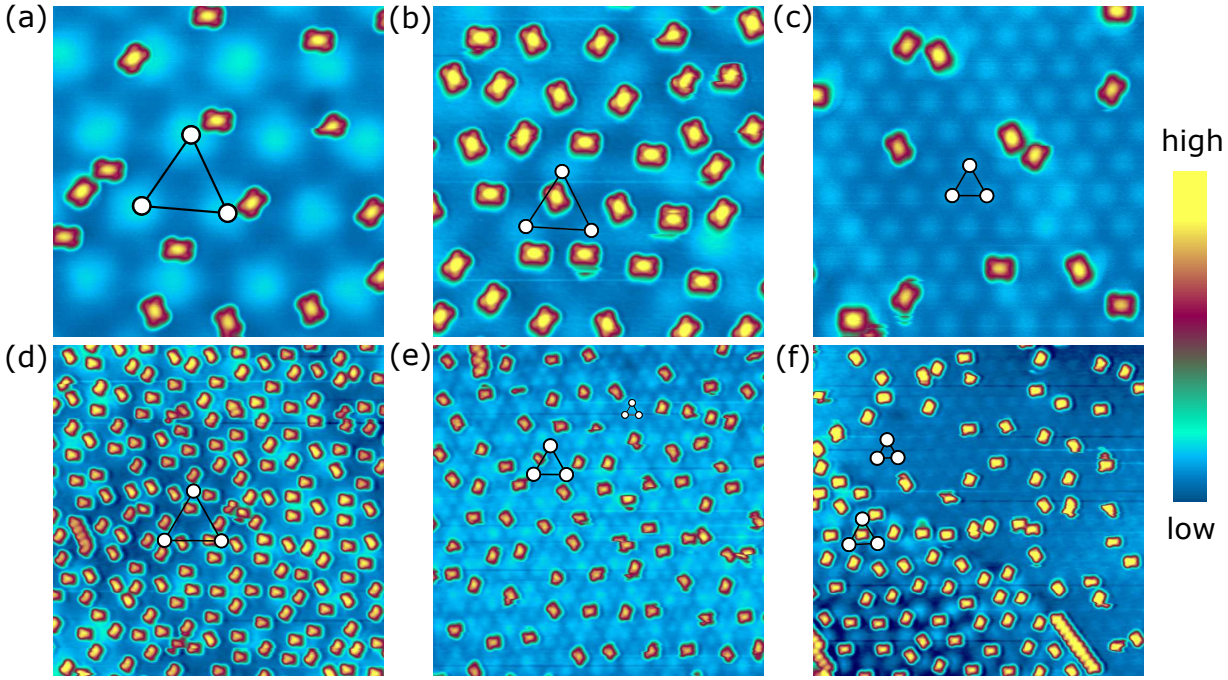

Figure 4.5: Single molecules on moiré superstructure: Image size is 20 nm × 20 nm for (a), (b) & (c), and 40 nm × 40 nm for (d), (e) & (f). All images recorded at 2V and 10 pA. Markers indicate the moiré superstructure by joining three adjacent *top* sites.

Effect of moire pattern

Multilayer graphene contains a collection of domains with various moiré superstructure originating from the angle between the top layers.[(b)] The assembly of isolated F_4TCNQ molecules is influenced by the periodic electronic modulation of graphene layer in the moiré structure. Depending on the bernal stacking of carbon atoms, electronic interaction between the two layers give rise to selective adsorption sites for molecules. The spot with AA stacking of C-atoms is referred to as *top site* which appears bright in STM image while the position of AB stacking is referred to as a *valley site*. Molecular assembly on different moiré domains are shown in fig-4.5.

While it is commonly observed for the molecules to move under the influence of the tip, this trend ceases to a great extent when they are adsorbed on specific sites of moiré domains. In fig-4.5(a), single molecules reside at sites located between *top* site and *valley* site for a moiré unit cell larger than the size of the molecule. Occasionally, a rotation of the molecule is observed following three fold symmetry on the graphene lattice.

It was previously reported that the adsorption site favorable for F_4TCNQ is determined by the highest overall electron density on the underlying substrate. In epitaxial graphene, for example Gr/Ir(111) system, F_4TCNQ adsorbs on the electron rich FCC site where the metal atom lies

[(a)] This can be observed in previous figures (4.1(b), 4.3(a) & (b)) as well.

between (and below) the C-C bond of top graphene lattice.[78] In the moiré superstructure of bilayer graphene, AA stacking region is identified with larger electron density and AB with lower density. The molecules, in this case, avoid the AA region and prefer to adsorb onto a bridge site i.e. between top and valley positions.

With increasing molecular coverage the bridge positions on moiré are filled up , such as shown in fig-4.5(b). As long as the moiré unit cell is large enough to allow all the molecules to avoid the AA regions there exists stable adsorption sites on the surface for the molecules. When moiré cell size is relatively large, there is an aggregation of molecules around the *top* site, such as depicted in fig-4.5(d). Thus, clusters of 3-4 F_4TCNQ molecules can be seen close to *top site*, throughout the valley domain. However, when the moiré unit cell size approaches the dimensions of a molecule like the image shown in fig-4.5(c) we observe tip-induced molecular motion during scanning reflecting less stable adsorption sites.

Therefore, we conclude that long range ordering of F_4TCNQ is due to site selective adsorption linked to the moiré pattern.

The last two figures of 4.5 ((e) & (f)) show regions with multiple moiré domains. In 4.5(e), the superposition of two moiré domains[(c)]involving top three graphene layers can be seen. In this complex geometry, F_4TCNQ molecules find their preferential adsorption sites based on adsorption energy profile of the surface. The periodicity in moiré modulation can be identified with the help of two triangles in this image.

The area shown in fig-4.5(f) has two separate moiré domains as a result of different lattice orientation of the layer below. The topmost graphene layer is continuous and the different domains arise from a rotation of the layers below. This particular region is interesting as it shows a transition of F_4TCNQ surface coverage from an ordered molecular assembly to a disordered one. The region on left has higher moiré cell size accommodating at most one molecule per *valley* site. Here the distinction between the *valley* site and *bridge* position is hard to make as they are located in close proximity. The characteristic feature of this region is that all molecules avoid the *top* sites and occupy the darker *valley* positions. It also ensures that maximum packing of single molecules is achieved. On the other hand, the region on right side has a lower moiré size where the molecules aren't able to differentiate between small changes in the adsorption energy of the surface and thus, are more mobile during scanning.

Due to a weak interaction with graphene, the F_4TCNQ molecules show some instabilities during imaging and STS measurements with the STM. In the next section we investigate these molecules on nitrogen-doped graphene. As will be shown the doping can improve the stability of the molecule.

[(c)] i.e between the moiré of 1st-2nd layer with the moiré of 2nd-3rd layer

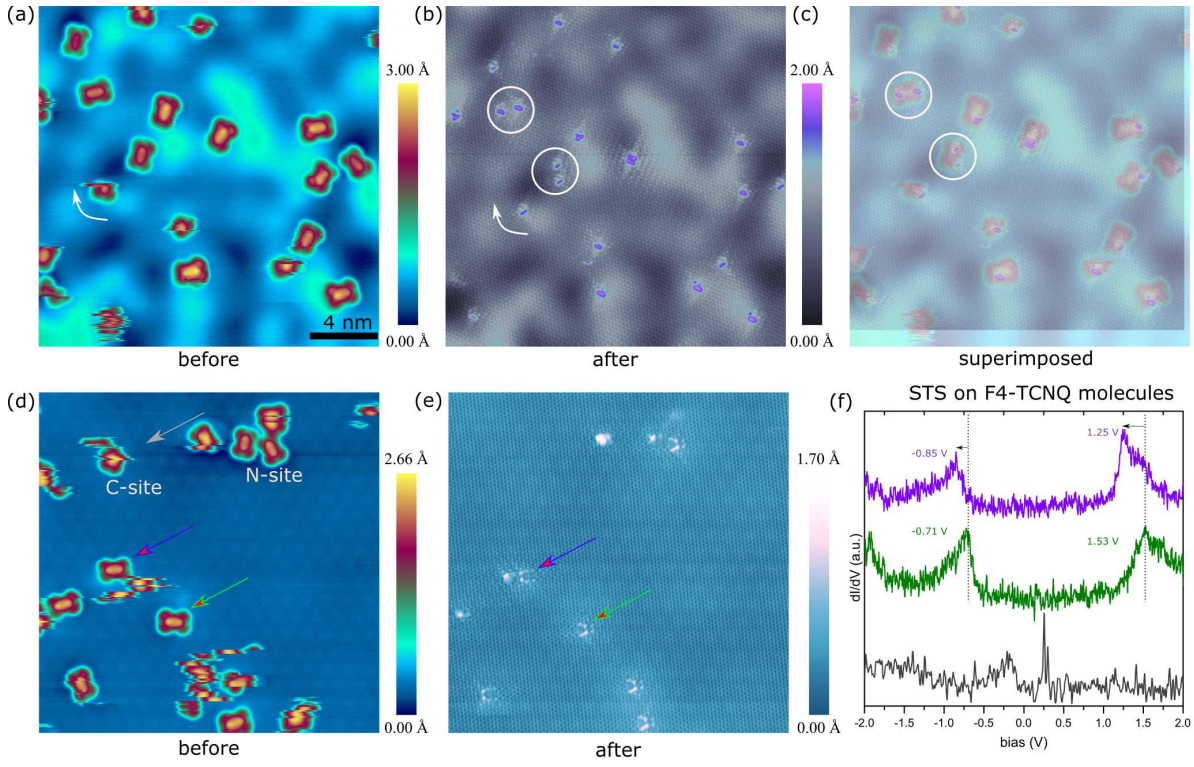

Figure 4.6: F_4TCNQ on N-doped graphene(a) STM image of single molecules on N-doped graphene, molecules that are stable are on N-site while mobile ones are on C-site (2V, 10 pA). (a) Same area as in **a** after removing the molecules (1.5V, 1 nA). (c) Superimposed image of **(b)** on **a** showing the position of N-atoms and double N-atom pairs underneath F_4TCNQ molecules. (d) Different area for molecules on N-Gr where STS has been recorded for F_4TCNQ on N-site and C-site (2V, 10 pA). (e) Adsorption sites beneath the molecules for the shown in **(d)** (1V, 400 pA). (f) STS comparison for molecules on C-site, N-site and double N-pairs.

4.1.2 On nitrogen-doped graphene

At the atomic level, the electronic charge density is modified at the N-site. These dopants induce a local charge transfer at the graphene-molecule interface. These sites are then expected to be efficient adsorption sites for the strong electron acceptor molecules, like F_4TCNQ.

At low concentrations, single F_4TCNQ molecules preferentially occupy nitrogen sites first. In fig-4.6(a) and (d), isolated F_4TCNQ molecules can be seen that appear to be stationary or mobile on the N-doped graphene substrate. In order to identify the adsorption site for these molecules, they were removed by using relatively high current set-point and low bias (500 pA and 0.5 V), and imaged afterwards. The topography image in 4.6(b) shows the area in (a) after removing the molecules where the nitrogen atoms can be identified with bright purple spots. Similarly, the image in 4.6(e) shows the dopants after removing the molecules in 4.6(d). Comparing the *'before'* and *'after'* images, we find that the molecules atop N-site are stable while those moving are on C-site. In some cases, it is possible to find a molecule stable on a C-site but those are rare

instances where a structural corrugation may help stabilize molecular position. We concentrate on molecules adsorbed on relatively flat surfaces, away from the regions of grain-boundary, large surface ripples or unknown defect sites.

In fig-4.6(c), the images (a) & (b) are superimposed to show the position of nitrogen dopants with respect to the molecules. In this comparison, majority of molecules adsorb asymmetrically onto single N-sites. The result of which is an asymmetry in the STM topography image. Geometrically, these positions coincide with the location of cyanide groups (lobes) or the **C-atom** joining the cyanide groups. Because of this *anchoring* property, sometimes rotations of the molecule are seen when the molecule is attached with one of the cyanide groups and can be tracked in successive STM images. One such movement is recorded in 4.6(a) where a molecule on N-site rotates while scanning, and is marked by a curved arrow.

There exists *nitrogen pair* type dopants which are located close enough ($\approx$ 1 nm) so that a single molecule can adsorb on both the atoms. We find two such molecules in 4.6(a) sitting on N-pairs that are revealed when the molecules were removed. In fig-4.6(b) & (c), the site of N-pairs and the molecules residing on top of it are circled.

The dynamics of F_4TCNQ under the action of the STM tip gives further information on the stability of molecules depending on the adsorption site. We generally observed that molecules on C-site are translated by the tip, while molecules on N-site are mainly only rotated, which is indicative that the latter is more stable. The molecules sitting on N-pair atoms however appear to be stable.

We have also performed STS on F_4TCNQ to identify the electronic features of molecules related to their adsorption site.

Spectra of single molecule F_4TCNQ on N-doped graphene are presented in fig-4.6(f), which has been taken on the area shown in 4.6(d). The image in 4.6(e) shows the atomic positions of the nitrogen dopants. On this lattice, we identify three adsorption sites:

1. **C-site** which implies presence of only carbon atoms below the molecule.

2. **N-site** where only one nitrogen atom is present which interacts with the molecule.

3. **Double N-site** where the adsorbed molecule sits atop a pair of N-atoms in close proximity.

The spectrum on *C-site* (bottom curve) is similar to the molecules on *C-site* measured on pristine graphene. The spectrum on *N-site* however, clearly shows different features with peaks below (-0.85 V) and above (1.25 V) the Fermi level (E_F), unlike molecular states located very close to E_F for molecules on C-site. For the case of *double N-site*, the STS (top green curve) is similar to N-site with peaks at -0.71 V and 1.53 V. The electronic gap defined by these peaks are 2.1 eV and 2.23 eV for N-site and double N-site, respectively. In gas phase, F_4TCNQ is

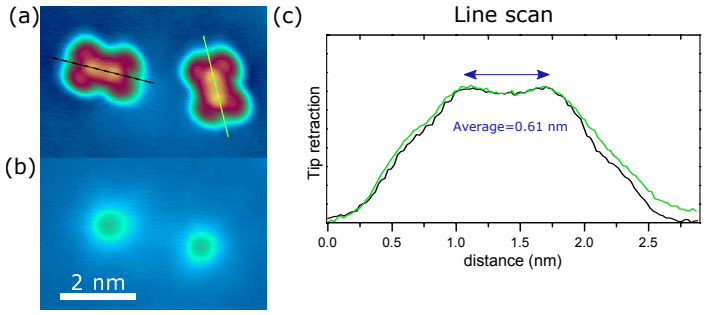

Figure 4.7: F_4TCNQ on N-site: (a) STM topography of F_4TCNQ adsorbed on N-sites, taken at 1.5 V and 5 pA. (b) Same area as (a) after removing the molecules (1.5 V and 100 pA) showing the two nitrogen atoms, and (c) Line scan profile for the molecules in (a) in the long axis of symmetry.

estimated to have a HOMO-LUMO gap of approx 3 eV (LUMO at -5.2 eV and HOMO at 8.3 eV).[143]

Molecules tend to re-organize energy levels depending on the coupling with the substrate. While it is possible that we observe HOMO-LUMO states on N-sites, the fact that F_4TCNQ LUMO is deeper than Dirac point of graphene may also lead us to probe LUMO and LUMO+1, or LUMO split into SOMO and SUMO seen at negative and positive polarity, respectively. In order to resolve the orbital shape for F_4TCNQ, conductance maps are required. Due to the weak interaction and instability of single molecules, the conductance map (dI/dV image) of the molecule at the energy of peaks were not successful so far and thus, remains a topic to investigate further.

In STM topography (constant current) images, the apparent shape of single F_4TCNQ molecules (at positive bias) on *N-site* is similar to that of pristine graphene (fig-4.4). The images in 4.7(a) & (b) show the molecules and the underlying N-atoms (after removal) in the graphene lattice, respectively. The typical shape of F_4TCNQ can be identified with two bright inner lobes and four outer lobes. In fig-4.7(c), the line scan profile passing through the long axis of symmetry for two molecules on N-site is presented. The distance between the maxima of the inner lobes is approximately 6.1 $\mathring{A}$ which is slightly less than the observed separation of 6.4 $\mathring{A}$ for C-site (fig-4.4(e)). This difference could be due to a difference in the molecular orbitals but also to the effect of acquisition mode (constant height in fig-4.4 and constant current in fig-4.6).

In this section, we focused on the electronic interaction of single F_4TCNQ molecules on graphene, both pristine and nitrogen-doped. Another aspect of molecular functionalization to explore the inter-molecular interaction and its role on molecular organisation on the surface. This is the topic of interest for the next part of this chapter.

4.2 Organization and inter-molecular interaction

Weak substrate coupling of F_4TCNQ with graphene leads to a loss in surface coverage when the sample is stored in room temperature (UHV) conditions. An unavoidable circumstance since the tip needs to be calibrated on Au(111) surface for reliable measurements. The surface coverage, thus, increases quite slowly with molecular deposition due to this competing loss. Increasing molecular surface density forces F_4TCNQ to interact with each other and to find energetically stable configuration.

4.2.1 1D growth

In the initial stages, low concentration of molecules adopt isolated configuration (as seen in previous section) which clearly indicates that close-packed assembly is not favored by F_4TCNQ on multilayer-graphene. With moiré supercell, there can be a degree of selective adsorption but eventually the molecules stay *isolated*. An increase in surface coverage leads to one dimensional ordered assembly of F_4TCNQ molecules in the form of *molecular chains*.

The stacking of the molecules in the 1D structure can be determined from the topography images shown in fig-4.8 which have been recorded for different surface coverage (or deposition). At comparatively lower coverage, a mixed phase of single and 1D linear structure of F_4TCNQ exists, as seen in 4.8(a), while at higher coverage, the number of 1D chains increases with gaps in between that are populated by isolated molecules. This clearly suggests that single molecule phase is preferred than the 1D packing arrangement. The formation of this linear structure can be understood by a balance of two main factors : (a) inter-molecular interaction determining the stacking and orientation of molecules, and (b) interation with the graphene including the moiré superstructure that prevent the adsorption of molecules on graphene AA stacking area. A third aspect of this *single-1D mixed phase* existence can be the surface molecular coverage. However, as we will see later in this section, this doesn't turn out to be a completely independent parameter to dictate the growth of 1D molecular chains.

Stacking of molecules is mostly influenced by the functional groups when the molecule-substrate coupling is weak. Here, we compare the molecular assembly of TCNQ and F_4TCNQ on graphene. TCNQ molecules form 2D islands on pristine and N-doped graphene.,[119] however we don't find such packing for F_4TCNQ. Both molecules show similar properties on graphene and theoretical works on this topic have demonstrated such behavior.[117,141] It has been found that the adsorption energy for F_4TCNQ on graphene (monolayer) is less than the TCNQ/gr. system.[117,141] The reduced interaction for F_4TCNQ molecules in a packed assembly is attributed to the repulsion between the fluorine atoms in the monolayer. Similar to -F groups, the -CN groups are also electron withdrawing in nature. The stabilization of molecular assembly through

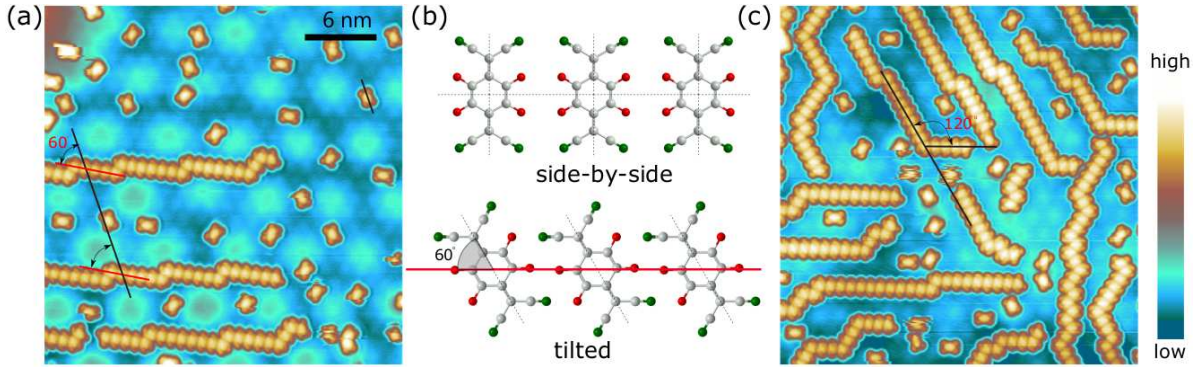

Figure 4.8: Molecular orientation in 1D chain (a) STM image of F_4TCNQ chains on pristine graphene at low concentration (2V, 10 pA). Black lines are aligned along the long axis of molecules and the red lines along the molecular chain axis. (b) Schematic for stacking of molecules in linear chain structure, side by side v/s tilted geometry are shown. In tilted fasion, the long axis of molecule makes 60° with the 1D chain axis, as seen in **(a)**. (c) STM topography at higher molecular coverage showing an increase in number of chains and the chain length. Long range formation is hampered on graphene moiré and bends are observed (2V, 10 pA).

hydrogen bond with -CN group (in TCNQ) is absent in F_4TCNQ.

In a simplified version, we can visualize the carbon backbone which is comparatively electron depleted due to the presence of four fluoride and four cyanide groups in this small molecule. The F_4TCNQ molecule can be modelled as symmetric distribution of polar bonds with a *zero* net dipole moment. In this electrostatic picture, the 1D chains observed experimentally could correspond to an alignment of negative and positive centers.

In fig-4.8(a), a black line indicate the long axis of the molecules that are involved in 1D chains. Interestingly it can be seen that the orientation of the molecules in chains is the same as that of isolated molecules. Concerning the structure of these chains, it is characterized by an angle of 60° between the molecule long axis and the axis of the chain as depicted in the figure by the angle between red and black lines.

The structure of the linear chain correspond to a tilted stacking of molecules that is different from other structures reported on other type of graphene samples as depicted in fig-4.8(b). In the top image, a side by side structure is shown that correspond to the alignment that has been reported in 2D lattice on graphene on hBN.[79] In the bottom images, a chain with the long axis of molecule tilted by 30° corresponding to the chain structure that we measured is shown (with an angle of 60° between chain and molecule axis).

When the molecular density is increased, more 1D chains can be seen on the surface. Parallel chains can be seen in image 4.8(c) that maintain close distance but avoid side-by-side stacking and therefore avoid the formation of two dimensional lattice. We observe this feature even at higher concentrations. The electrostatic interpretation provides a reasonable explanation for this behavior. In the molecular chains, the sides are terminated by -CN groups on both sides which

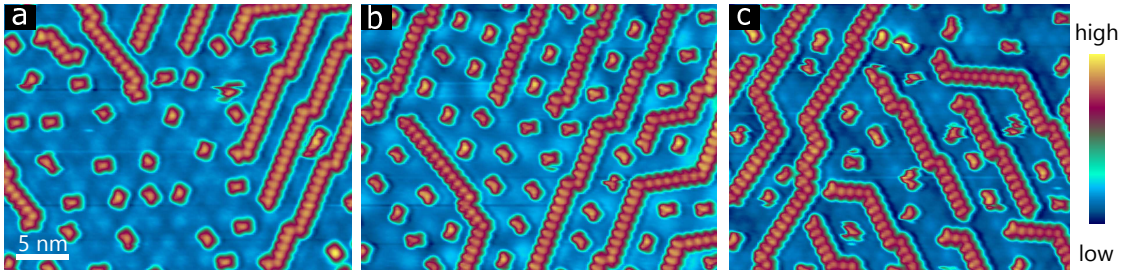

Figure 4.9: Moiré influence on molecular chains: With increasing surface coverage molecules pack densely into chains. (a) Combination of single F_4TCNQ and linear chains with some available sites for molecules. (b) Dense packed structure of single molecules and chains, chain lengths are longer compared to **(a)**. (c) Less number of single molecules and more lengthy chains. The scale bar is 5 nm. STM parameters- 2.0 V and 10 pA

gives slightly negatively charged character in the transverse direction which doesn't favor packing of molecules.

Beside the **straight chain** structure described above, a **zig-zag chain** arrangement can rarely be observed where the center of molecule deviates from a straight line alignment even at short range. Interestingly, in the chains, the perfectly straight parts have a limited length and 'kinks' are formed along the chains. The images clearly show that the formation of kinks correspond to an avoiding of AA stacking region by the molecules, which are less stable sites for the adsorption as described previously. This can be seen in image 4.8(a). We note also that zig-zag chains can be seen corresponding to a line of kink structures (figure 4.8(c)).

4.2.2 Moiré influence on molecular stacking

Single molecule adsorption on moiré regions are observed in a range of domains with different angles of rotation. The atomic corrugation of the top graphene layer forces molecules to adsorb in an intermediate position close to the low lying sites in accordance with the flat geometry of the molecule.[144]

At first, the influence of moiré pattern is not completely evident on 1D chains but a pattern emerges by observing their *collective behavior* at higher chain density. For isolated molecules, moiré cell provides selective adsorption sites. The orientation of molecules in 1D chains is similar to that of isolated ones, which suggests that there is not much variation in the adsorption behavior of molecules on graphene lattice. Mixed phase existence of single molecules and chains points to close adsorption energies for the two cases. It is very likely that the adsorption behavior of molecules in 1D chains, on graphene lattice, are influenced by similar effects as that for single molecules.

The STM topography image in fig-4.8(a) shows three linear chains in a moiré region which occupy the low-lying areas of the moiré superstructure. When the surface coverage is increased

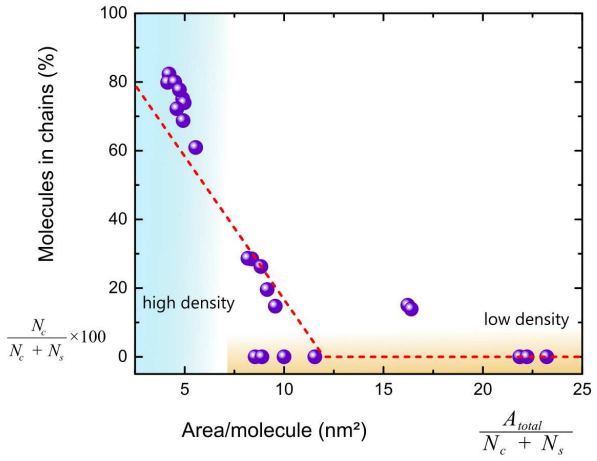

Figure 4.10: Dependence of number percentage of molecules in chains with surface density

gradually, more single molecules start to occupy the intermediate adsorption sites on moiré cell. When all these adsorption sites are occupied, any further increase in the surface density forces the molecules to occupy positions between the previously adsorbed molecules, thus growing into a connected 1D network.

At higher molecular density, the number of chains increase on the surface and the organization or the packing of chains can be observed through the images shown in fig-4.9 (a)-(c). These three images show chains formed in different moiré regions, going from left (a) to right (c) we can observe an increase in the moiré cell size also. It can be seen from these images that molecular chains are *always* formed in the dark regions of moiré, avoiding the bright (top site) regions. The intrinsic nature of F_4TCNQ to avoid the bright regions also explains its failure to assemble into a packed 2D lattice. The tendency to pack in a molecular island is further hindered by weak inter-molecular forces between them.

We make a statistical analysis for the number percentage of molecules staying as single/isolated or in chains. The plot shown in fig-4.10 shows the fraction of molecules that form chains as a function average area occupied by all the molecules. The quantities N_C and N_S represent number of molecules in chain and in single phase, respectively. In a given area (A_{total}), the average area per molecule is the ratio $\frac{A_{total}}{N_C+N_S} = A_{avg}$.

The percentage of molecules that form chains (f_C) is then given by, $\frac{N_C \times 100}{N_C+N_S}$. For domains with only single molecules, $N_C = 0$ and so the fractional percentage f_C is also 0. The x-axis of the plot, A_{avg} is the inverse of molecular concentration. With increasing surface coverage, more and more molecules occupy the same area leading to an increase in concentration or a decrease in average area/molecule, A_{avg}. In the plot, we find that molecules start to condense in 1D chain phase for value of A_{avg} around 10 nm^2 which is marked by an increase in percentage

value f_C. Increasing the molecular coverage beyond this point leads to increase in molecules in chain phase and increases very sharply. Thus, the onset of chain formation can be identified by a critical molecular concentration $A_{cr.}^{exp}$ that determines whether the molecules remain as isolated or assemble into linear chains.

We make a simple fitting based on observed experimental results by measuring area occupied by a single molecule (A_C) and area of one molecule in chains (A_C). Indeed the total area can be expressed as,

$$A_{total} = N_C A_C + N_S A_S \tag{4.1}$$

We find from topography images, value of A_S around 1.8 nm^2 and A_C to be 1.2 nm^2. This analysis is done in SPIP software using the *Particle and Pore Analysis* tool. Here we define a threshold current parameter to count the particle shape as a single molecule or chain. Since we have taken all images at 10 pA, the obtained values are fairly consistent through different datasets.

One of the characteristic features of molecular chains is the presence of *kink* molecules which divide the chain into segments. The formation of linear chains with a kink position is illustrated in fig-4.11. In this figure, a schematic of moiré on bilayer graphene is shown with a rotation of 5.4° between the layers. This gives a moiré periodicity of 5.4 nm which is marked by arrows. On top of this moiré region, F_4TCNQ molecules are stacked side by side forming a linear chain. The chain axis is shown by green arrow.

There are two ways to form a linear chain while avoiding the *top sites* of moiré cell-

1. Chain axis is parallel to the lattice vector of moiré supercell, thus passing through the AB and BA sites of the lattice.

2. Chain axis is inclined with respect to the moiré lattice.

The first configuration, though possible, has not been observed in our experiments. Mostly, the chains are found to have some inclination between the chain axis and moiré lattice vector. In some cases, the chains are aligned with moiré vector direction but these are also the regions with smaller moiré cell size. In this condition, the angle is quite small and difficult to distinguish from other adsorption sites. It is therefore, reasonable to assume that the chain axis is not aligned with moiré lattice directions.

Usually, the top part (or upper half) of F_4TCNQ is situated near the top of neighboring molecule while forming a chain. However, when the neighboring molecule shifts in a way that top part of a molecule is close to bottom part of the preceding one, a kink is formed in the chain. These 'kink' molecules are formed from a shift along the molecule long axis to avoid

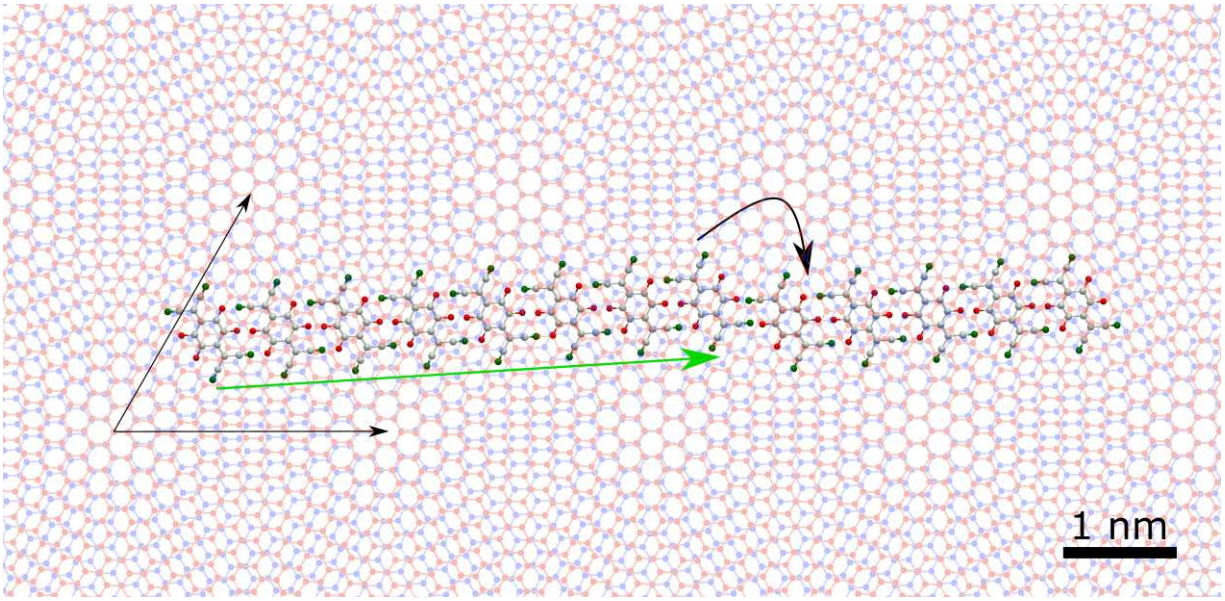

Figure 4.11: Schematic of a F_4TCNQ linear chain on bilayer graphene. The moiré superstructure has a rotation angle of 5.4◦ between the layers. Lattice vectors of the supercell point to the AA top sites.

adsorption on top sites of moiré supercell. Thus, after a certain distance, molecule assembles with a transverse shift to continue the growth of the molecular chain.

In this schematic, we find a form of moiré cell size dependence for the position of *kinks* in the chains. With smaller moiré cell, the chains encounter the 'top' sites at smaller distance which would lead to more kinks in the chain. Similarly, for bigger moiré cell, the kinks should appear at larger distances or the chain segment length between two kinks increases. In experiments, we observe linear chains that have various chain segment length in the same domain. This complicates the analysis for determining the average chain segment length versus moiré unit cell size. The spread is relatively large where we find chains that have segment length ranging from 3 to 15 molecules per segment.

Another important factor is the molecular surface density. The dependence of segment size on the moiré cell size can be observed on graphene domains that have the highest possible concentration of molecules which is not the case. It is hard to find regions that are saturated with molecules, and also with varying moiré cell.

We still argue that the kink formation in 1D chain is induced by the presence of AA sites on graphene lattice. The influence of Gr/Ru(0001) moiré forces the TCNQ molecules (as shown in fig-1.4c)to form linear chains just as we observe for F_4TCNQ here on multilayer graphene. Also, we don't have any instances of molecules occupying the top sites for moiré cell with larger lattice vectors compared to molecular length. These observations clearly reveal the moiré supercell

influence on the growth of 1D molecular chains.

Chains have an inclination with the moiré vectors, further enforces the fact that molecular adsorption on AB and BA sites (dark sites) are not favored but the bridge positions in between. For domains on graphene with smaller moiré cell, the chains appear to be aligned with lattice vectors but that is due to the fact that different adsorption sites are located very close to each other giving a pseudo-appearance. We note that even in these areas, kinks are present on the chains suggesting that *top* sites are encountered in the long range which is better explained if the chain axis is not aligned with moiré lattice.

In comparison with the single isolated molecules, linear chains exhibit similar trends of site selectivity concerning adsorption on graphene as well as on a moiré lattice. In the next section we investigate the electronic properties of the molecular chains.

4.2.3 Electronic structure of molecular chains

Since molecular chains are more stable than single molecules, setpoint parameters with higher tunneling current can be used to image and acquire spectra for these structures. In fig-4.12, a comprehensive analysis of the STS on molecules in 1D chain is presented. We distinguish three cases corresponding to molecules at the *edge*, at *kink* positions, or in the *middle*. The *edge* molecules are stable during imaging, however they diffuse on the surface when we perform a spectroscopic measurement. Gradually the chains get disintegrated if the edge molecules are removed by taking STS measurements.

The STS plots shown through fig-4.12 (a)-(c) have been taken on a molecular chain and correspond to sites represented by markers (*circle, plus, triangle*) in the topography image (d). Red circles mark the *kink* sites while the 'plus' and 'triangle' correspond to middle-position molecules. Further, the plus markers identify the spots corresponding to mid-portion of the molecules while the triangle denotes the site between the molecules. In this way, a spatial distribution of STS on the molecular chain can be examined. The typical features of electronic spectra in 1D chain are a sharp resonance type peak at around -0.8 V and a broadened feature at 0.23 V. In these spectra, the position of the peak in negative bias varies greatly unlike the states at positive bias. A distribution plot (fig-4.12(e)) details the range of the peak position for the STS shown through (a)-(c). The peaks at negative bias mostly lie between -0.75 to -0.83 V with a mean value of -0.8 V and the range can be upto 0.1 V which is rather large and hints towards charging type behavior of molecular energy levels. Comparatively, for the positive bias, the range is from 0.21 to 0.25 with a mean value of 0.23 V. The shifts in the peak position in this case is clearly smaller than the peak at negative bias and lies within the error bar of the determination of the peak position.

The energy position of peaks measured at positive bias is similar to the values measured on

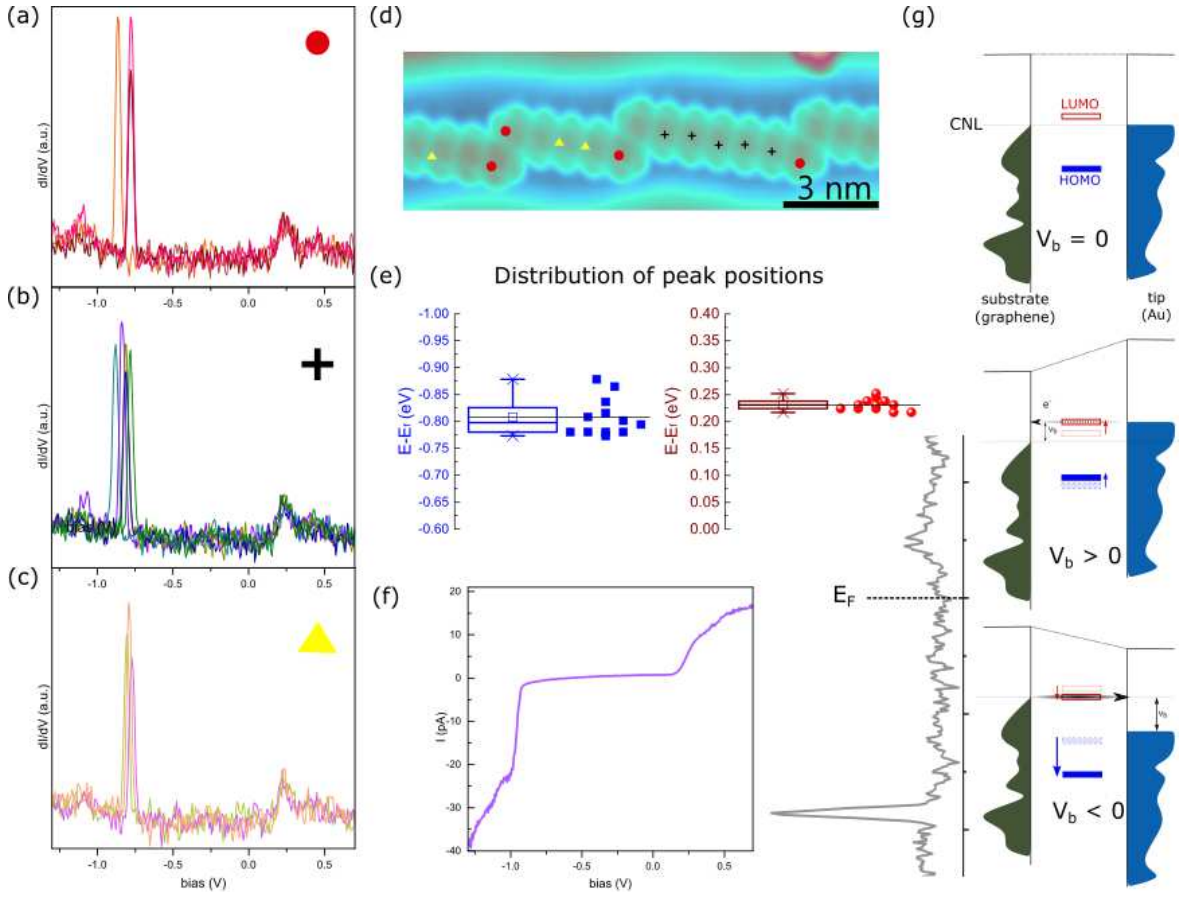

Figure 4.12: STS on F_4TCNQ linear chain The graphs shown in figures- (a), (b) & (c) show STS on molecules in a 1D chain on pristine graphene. *Circle, plus and triangle* shapes identify kink position, and two middle positions (center of molecule and between the molecules), respectively. (d) STM topography of the linear chain on which STS has been recorded (2V, 10 pA). (e) The energy position of peaks in positive and negative bias are shown in a scatter plot for the STS shown through **(a)-(c)**. (f) An example of I-V plot of the spectra showing sudden increase in tunneling current close to -1 V. (g) A simplified schematic of energy level alignment for *Gr-F_4TCNQ- Tip* system at zero bias (top), positive resonant conditions (middle) and negative resonant conditions (bottom). An example of dI-dV spectrum is placed vertically for visual aid.

individual molecules. In this case, the state observed in the positive bias is very close to E_F (similar to isolated molecules) whereas, for negative bias, resonant peak is seen much deeper for a state lying close to E_F. We suspect that the peaks in STS are coming from the same LUMO orbital.

To understand the -0.8 V peak for linear chain, we focus on its I-V characteristics. As shown in fig-4.12(f), the tunneling current increases dramatically near -0.8 V and this behavior is typically observed in the case of charging (or discharging) of physisorbed molecules. Since HOMO state of F_4TCNQ lies deep compared to the fermi level of the system, we assume that this peak corresponds to the *charging* of LUMO state of molecule in the chain phase. The energy level diagram corresponding to the STS are illustrated in fig-4.12(g) and a representative STS plot is shown alongside.

Energy levels of substrate (graphene), tip (Au) and molecule are shown relative to the fermi level or *Charge Neutrality Level (CNL)* of the system at zero bias. The STM tip is considered to be gold since it has been calibrated on Au(111) surface by making several indentations on the surface which covers the tip apex. For better understanding of the main features of the system we consider, as usual, that the tip and the sample have the same workfunction. HOMO and LUMO of the molecules in chain are placed at energy levels corresponding to gas phase single molecules with respect to the vacuum level. Since, the position of orbitals are not known *a priori*, we place LUMO above the CNL and will be justified later in the discussion. The schematic on top is a simplified representation of energy level alignment in the context of **double-barrier tunneling** suitable to describe electronic spectra in case of weakly bound physisorbed molecules.

The energy level diagram for positive and negative bias are illustrated below in fig-4.12(g). At positive bias, tip fermi level goes up with respect to substrate and subsequently LUMO level moves upwards relative to substrate. At 0.23 V, resonant tunneling occurs through the LUMO which is aligned with the Fermi level of the tip, i.e. electrons are tunneling from filled states of the tip to the vacant LUMO and substrate levels. In negative polarity, reverse trend is observed where the tip Fermi level moves downwards together with the LUMO state, with increasing magnitude of bias voltage. Tunneling through the LUMO occurs with electrons tunneling from the filled states of substrate to available empty states of the molecule and the tip, when the Fermi level of graphene aligns with the shifted LUMO level. To confirm whether the peak at -0.8 resonant peak corresponds to a charging phenomena, an electric field dependent measurement has been performed at a fixed site on the 1D chain.

The electric field between the tip and sample is varied by bringing the tip closer to the surface while keeping the tunnel bias constant. At a given tip-sample separation (d_{ts}), STS is recorded on the chain to find the position of the resonant peak. The plots in fig-4.13 summarize the results for this experiment. The image in 4.13(a) shows the position on the chain where the spectra

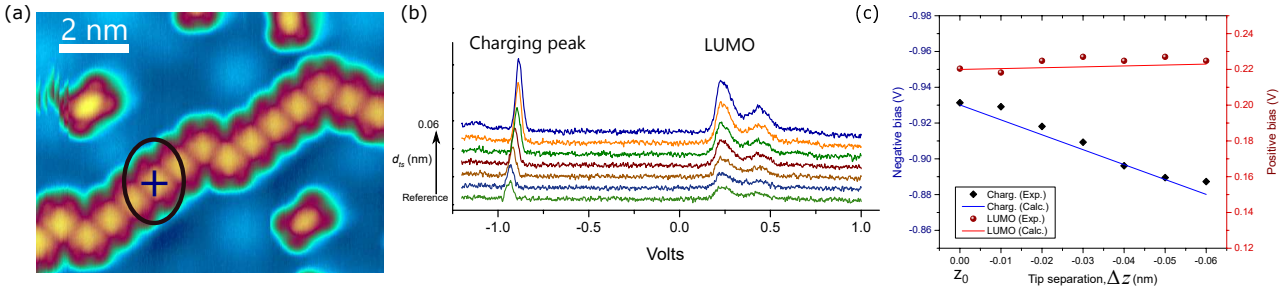

Figure 4.13: STS as a function of tip-sample distance: (a) STM image of F_4TCNQ chain with a marked molecules on which STS is recorded as a function of tip separation. (b) Waterfall-type plot showing the shift in the energy position of the resonance peak in negative polarity. Going from bottom to top, the tip-sample separation decreases. (c) The resonance peak positions are plotted for change in the tip-sample distance, compared to a reference starting distance.

was recorded as a function of tip separation and the corresponding curves have been plotted in 4.13(b). The plots are shifted in the vertical direction to observe the evolution of peak positions and is plotted in 4.13(c).

It is evident from the plots in 4.13(b) and (c) that the energy levels shift for the resonance (or charging) peak in negative bias. The energy position of peaks at positive and negative bias, in fig-4.13(c), is fitted with a mathematical model developed in the framework of double barrier tunneling.[145]

This model is used here to obtain original energy position of the LUMO level (E_0) that lies near E_f. Under the assumption that the LUMO state is observed as charging peak in negative polarity (-0.8 V), we can express measured energy position ($E_{charging}$ and E_{LUMO}) by following equations:

$$\begin{aligned} E_{LUMO} &= E_0\left(1+\frac{d}{\epsilon z}\right) \qquad \text{positive LUMO peak} \\ E_{charging} &= -E_0\left(1+\frac{\epsilon z}{d}\right) \qquad \text{negative charging peak} \end{aligned} \tag{4.2}$$

Here, z is the tip-sample (molecule) distance and can be expressed as $z = z_0 + \Delta z$ where z_0 is the reference distance corresponding to current setpoint. Δz is relative tip approach towards the sample as shown in fig-4.13(c). The parameters d and ϵ are F_4TCNQ-graphene distance and effective dielectric constant for this system, respectively.

Above equation is solved for the peak position shown in plot 4.13(b&c) for the changes in tip sample distance upto 0.6 Å. The value of E_0 from this fitting comes out to be around 0.18 V and tip-sample distance for reference position, i.e. z_0 is 9 Å. The ratio of the constants for this system, $\frac{d}{\epsilon}$ is around 2.6 Å

Comparatively, the variation of the peak position at positive bias is quite small and almost lies constant. On the other hand, the peak position is seen to decrease monotonically with smaller tip-sample distance in negative bias. With smaller d_{ts}, the electric field in the tunneling region increases. The position of the peak shifts closer to E_F which means that the bias required to reach the resonant tunneling conditions is lower.

The discussion on the charging of molecular state is based on the presence of sharp resonance peak below fermi level. By observing the movement of energy levels with respect to bias polarity, this also fixes the position of the LUMO level of molecules in the equilibrium state. If the LUMO were positioned below CNL, the resonant conditions at positive bias would not be observed since the tip Fermi level would shift faster than the LUMO. Even in the case of strong coupling of energy levels between tip and molecule, the levels would still maintain a constant difference at any positive bias, just as in equilibrium.

The energy value of 0.8 eV below E_F for the charging of molecule is an overestimation of the observed shift in LUMO position. A bias voltage of 0.23 V is required to reach tunneling conditions above E_F, therefore the maximum difference between the actual LUMO and CNL should not exceed this value if the coupling of molecular energy levels were symmetric at both interface. Experimentally, a much higher bias voltage on the tip (0.8 V) is required to bring the LUMO state at the fermi level of graphene. Since the two materials on both sides are characterized by different distribution functions for the DOS, and charge carrier density at the fermi level, the molecule is most likely to have an asymmetric coupling in this arrangement. In this case, the influence of the movement of tip fermi level on the position of molecular levels is smaller as compared to the substrate.

4.3 Conclusion

In this chapter, the assembly and electronic properties of F_4TCNQ molecules on multilayer graphene substrate has been studied. At low concentrations, F_4TCNQ adsorbs as single isolated molecules. F_4TCNQ avoids packing into a molecular lattice which suggests that the inter-molecular interaction is, to some extent, repulsive in nature.

The molecules orient with their long axis along one of three symmetric arm-chair directions on the graphene lattice. Additionally, F_4TCNQ is sensitive to the periodic modulation of LDOS in a moiré supercell. Site selective adsorption of molecules is observed in moiré superstructure where the preferred adsorption site lies in an intermediate region between the *AA* and *AB/BA* sites. The atomic corrugation of a moiré cell has minimum effect on the flat geometry of the adsorbed molecule, in these intermediate positions, thus maximizing substrate-molecule interaction.

Single F_4TCNQ molecules are weakly bound to graphene substrate as translational and/or

rotational motion can be induced from the STM tip during scanning. In this non-covalent interaction, F_4TCNQ retains its gas phase energy levels and wherein the LUMO state stays near the fermi level of graphene. In experiment, the STS on single F_4TCNQ molecules show resonant peaks close to fermi level of the system. The shape of the molecule recorded in the constant height mode at these peak positions resemble with the gas phase LUMO shape confirming the argument for energy level alignment.

Increased surface coverage forces the molecules to pack in one dimensional molecular chains, thus having a higher packing density compared to isolated phase. In this phase, molecules assemble in a tilted fashion to minimize the intramolecular dipole-dipole repulsion arising from the electro-negative functional groups present on periphery of the molecule (-F and -CN groups). The growth of the 1D structure takes place at an angle of 60° with the long axis of the symmetry for the molecule. Formation of the molecular chains takes place in accordance with site selection adsorption on graphene and moiré lattices. The molecular energy levels of frontier orbitals in 1D chain experience slight broadening forcing the LUMO to reside above the fermi level. In the tunneling spectra, this level is identified by a resonant peak below E_F and characteristic of charging type behavior of molecules in double-barrier tunneling.

As a model system, multilayer graphene and F_4TCNQ demonstrate fine tuning of electronic interaction in the framework of physisorption.

Chapter 5

Surface studies on Black Phosphorus

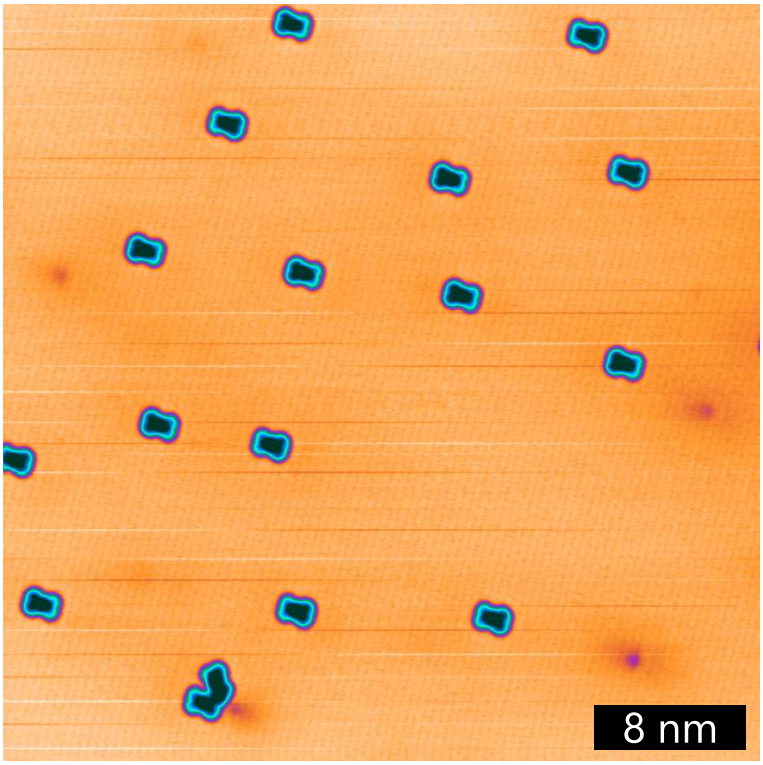

An investigation of back phosphorus surface is presented in this chapter with particular emphasis on the properties of intrinsic defects. Being an optically active semiconductor, understanding the precise nature of defects is of great importance for exploring the potential applications of black phosphorus.

5.1 Introduction

Atomic scale investigation of black phosphorus (BP) is relatively new if one consider that it was first synthesized in 1914 by Bridgman.[146] Although the first STM study of black phosphorus surface was carried out in 1992[147] but it was only in 2009 that the work by Zhang et al[148] could clearly show the atomic arrangement of the (010) surface of BP crystal. Within the last decade, there have been handful of STM based investigations[129,130,149–151] going beyond structural studies in order to explore the electronic properties of the BP surface. In this category, the understanding of the native defects present on the surface has only recently been reported in the last couple of years. Of particular interest are two studies[129,130] performed at low temperature (5 K) which discuss the properties of defects in pristine samples, investigated by scanning tunneling microscopy and spectroscopy along with supporting calculations. The presence of these defects have been confidently reported in STM measurements by different groups and are believed to be intrinsic to the material. A wholistic understanding of the nature and origin of defects is still in its infancy and not yet fully understood.

In this chapter, we present our STM and STS measurements on a pristine BP sample at 5K. All measurements have been performed on UHV cleaved samples, the details of which are explained in chapter-2. The UHV cleaving ensures a high degree of purity of the surface. Black phosphorus is known to be quite reactive in ambient conditions where it can undergo oxidation, formation of hydrophosphoric acid or some other chemical changes depending upon the exposure time and environment. Also, the cleaving of BP crystal exposes the native defects in the bulk which is the subject of our investigation. The aim of this study is to find a coherent understanding of the nature of BP native defects. In the following sections, STM based results are presented for a BP crystal which can be broadly classified into two main groups:

1. study of pristine black phosphorus surface along with defects, and
2. interaction of electron acceptor molecule (F_4TCNQ)[(a)]with BP surface.

5.2 Structural and electronic properties of pristine black phosphorus

5.2.1 Pristine Surface

Black phosphorus layers are stacked along the [010] direction which are exposed after the cleaving process. A single layer of black phosphorus comprises of two parallel planes of phosphorus atoms

[(a)] *2,3,5,6-Tetrafluoro-7,7,8,8-tetracyanoquinodimethane*

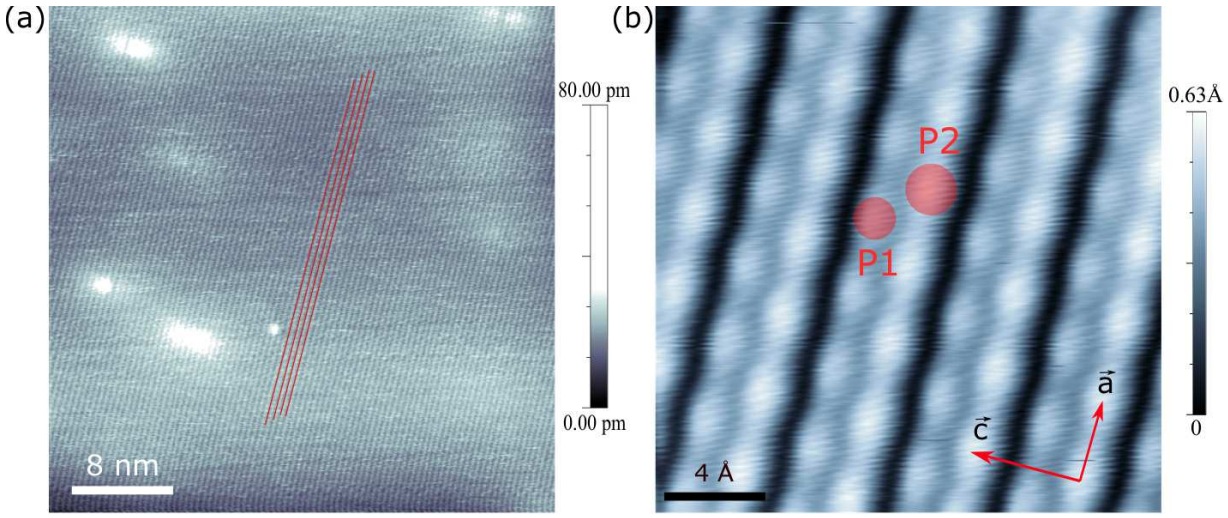

Figure 5.1: Black phosphorus lattice: (010) surface (a) Large area topography image at -2 V and 10 pA, (b) Small scale topography image showing phosphorus atoms taken at -50 mV and 20 pA.

(P-atoms) which are tetrahedrally bonded with each other due to sp^3 hybridization. In STM topography images, the (010) surface is observed as parallel rows of P-atoms with dark and bright contrast. The bright rows are the top plane atoms while the bottom plane is far away from the STM tip giving a dark appearance in the image. In the fig-5.1(a), a constant current STM image of 40 nm×40 nm area of black phosphorus is shown. The imaging parameters are -0.4 V and 100 pA for this image. There are two distinct features that can be identified in this topography viewgraph-

1. Presence of periodic atomic rows (red lines).
2. Randomly scattered bright spots with different intensities.

Arm-chair and zig-zag directions

A high resolution STM image of BP surface is shown in fig-5.1(b). In this image, the individual phosphorus atoms are resolved very clearly and correspond to the (010) surface of the bulk BP crystal. The vectors $\vec{a}$ and $\vec{c}$ are shown to identify the lattice direction in STM images. These periodic lines correspond to the buckled row of P-atoms as described in chapter-1. For simplicity, the vector $\vec{a}$ is also identified as the *zig-zag* direction in the single layer black phosphorus (or phosphorene) because of how they appear to arrange, from a top-view perspective. Similarly, the vector $\vec{c}$ is referred to as the *arm-chair* direction[(b)].

[(b)]These terminologies draw parallels from the zig-zag and arm-chair directions of carbon atoms in hexagonal graphene lattice.

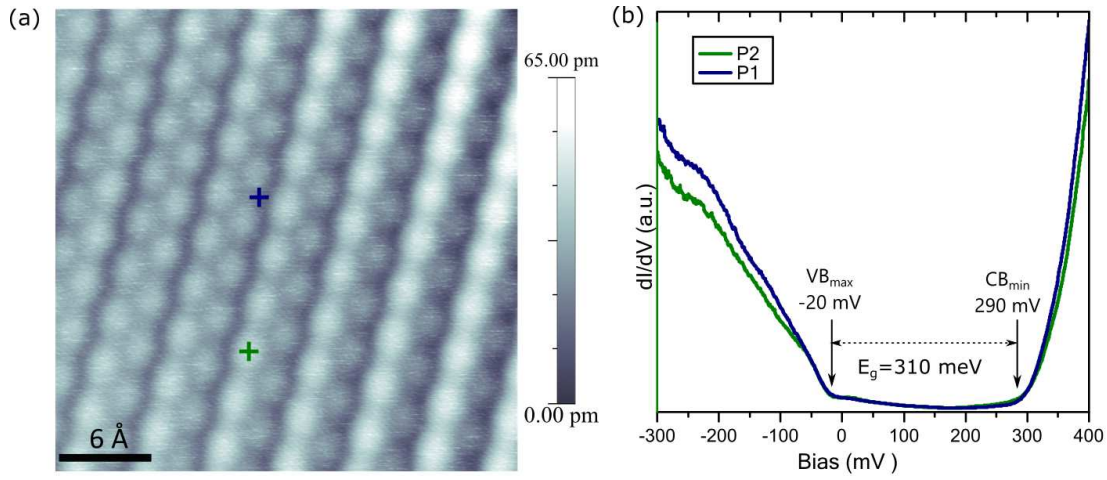

Figure 5.2: Energy band-gap (a)STM topography image (-50 mV, 50 pA) showing an area where spectroscopy has been recorded in black phosphorus sub-lattice at spots marked by green and blue cross. (b) Corresponding STS showing the energy gap of black phosphorus as measured on the marked areas.

The dark and bright rows of P-atoms in the arm-chair direction can be differentiated with good resolution. In the STM image, it appears that the width of atomic rows for the top and bottom P-atoms in the monolayer is different. The top P-atoms are clearly resolved and are wider than the spacing between them. This is because the wavefunction overlaps for the top P-atoms when the tip is moving from one atomic row to the next, giving a narrower width to the bottom row P-atoms.

The other noticeable feature in the atomic resolution image (5.1b) is the difference in the apparent width of P-atoms in the top plane. In this viewgraph, the phosphorus atoms on the right side of a given row appear bigger as compared to the nearest atom in the zig-zag direction, as indicated by the red circles. These two types of P-atoms in these circles are denoted by P1 (smaller size) and P2 (bigger size) henceforth. This has also been observed in other STM studies.[149] In view of the fact that our BP crystals are synthesized in the laboratory and that reported observations use commercially available samples, it is highly likely that the cause of unequal atomic size is intrinsic to the material. This rearrangement is understood as a surface reconstruction to account for the strain induced on the top layer of P-atoms due to imbalance in the co-ordination number on two sides. Thus, on BP surface, P1 and P2 atoms depart from a strictly coplanar arrangement wherein the atom denoted by P2 is slightly pushed out of the plane giving a slightly bigger appearance as observed in the STM image. It is entirely possible to find P2 on the left or right side of the zig-zag axis as a result of the propagating strain on the surface. Similarly, regions with equal size of P1 and P2 can also be found where locally the crystal surface is relaxed.[149]

We have investigated the electronic structure of BP by tunneling current spectroscopy. Since STS gives information about the LDOS at a given location, we take measurements on various spots to evidence intrinsic deviation in the spectra as a function of the atomic position in BP lattice. A sample data set is presented in fig-5.2 which shows a high resolution topography image and the measured STS on this BP lattice. In fig-5.2(a), the position of the STM tip for the spectroscopy measurements are marked by cross in green (for P2 atoms) and blue colors (P1 atoms). As such, we find no noticeable differences in the LDOS measured at different sub-lattice positions for black phosphorus.

The band gap of black phosphorus can be clearly seen in fig-5.2(b) to be around 0.31 eV which matches well with values reported for bulk crystal.[130,152,153] For a material where the band gap is highly sensitive to the number of layers, this shows that inter-layer electronic coupling is dominant in the measured STS for the top phosphorene layer. The valence band maximum (VB_{max}) is around -20 mV which is very close to fermi level suggesting that the sample is intrinsically p-doped.

Increasing efforts are directed towards the use of phosphorene to exploit its optically active tunable band gap.[154–156] In this material, defects play decisive role in electronic and optical properties. With that perspective, we turn our attention to the study of defects after investigating the structure and electronic properties of black phosphorus lattice, which is presented in the next section.

5.3 Native defects

The process of UHV exfoliation ensures high degree of cleanliness and also diminishes the chances of foreign contaminants to adsorb on the cleaved surface. In our STM measurements, the surface of BP is found to have randomly scattered point type defects as has been shown in fig-5.1(a) earlier. These bright spots are observed in our experiments, repetitively, through different samples and with multiple cleaving. It is highly unlikely to have foreign chemical species adsorbed on the surface under UHV conditions. So with that argument and taking into account the frequent occurrence of point defects on surface, we make the assumption that these point defects are intrinsic to bulk black phosphorus crystal.

The native defects reported in fig-5.1(a) appear as bright spots when imaged at negative bias. In fig-5.3 we show the same type of defects imaged at two polarities. It is worth to notice that the defects shown here are the most abundant and characteristic of black phosphorus. The apparent shapes and size of defects are quite different at +1 V and -1 V, circular dark spots are seen at positive polarity while elongated double lobes are seen in negative polarity.

Particular attention is drawn towards the defect shape in negative bias in fig-5.3(b). Here,

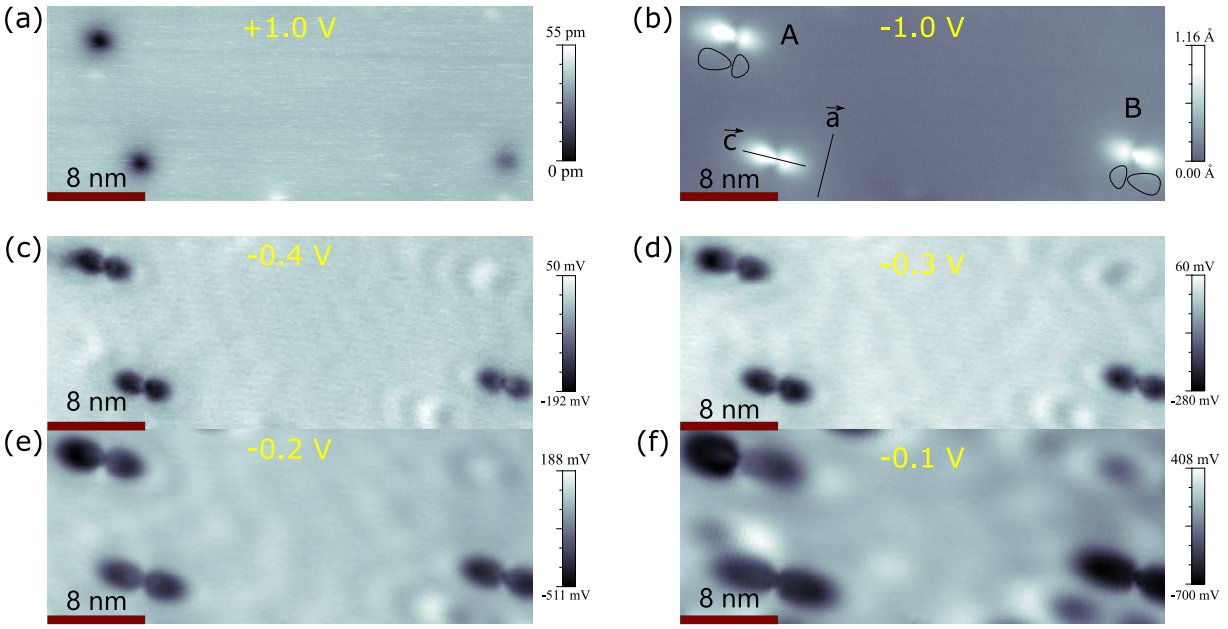

Figure 5.3: ***Peanut*** **defects:** STM topography image of native defects, in an area of 40 nm by 16nm, at (a) positive bias (+1.0 V, 100 pA) and (b) negative bias (-1.0 V, 100 pA). The peanut shape is evident in negative bias and has an energy dependence which is illustrated through conducting maps (for the same area) with corresponding voltage bias indicated in the figures.

the defects are identified by two unequal bright lobes leading to a "peanut" shape, and these defects will therefore be called *peanut defects*. The asymmetry in the lobes identify two similar configurations for the defects (A and B) indicating that these defects are sensitive to the sublattice position. This suggests that these defects are related to arrangement of P-atoms in the lattice that gives the peanut defect an inversion character in the arm-chair direction. These defects can arise from vacancy or missing P-atom/s in the top layer or a bridging configuration of P-atoms between two layers.

This peanut type shape for defects has also been reported in previous STM studies on BP.[129,130] The schematic drawn close to defects A and B clearly demonstrate the change in lobe positions for the two sublattice sites.

Peanut defects

With reference to $\vec{a}$ and $\vec{c}$ vector directions of the BP lattice (see fig-5.1), the bright lobes of the defect always extend in the armchair ($\vec{c}$) direction. In fig-5.3(b), two black lines are drawn along the lattice vectors around a defect for illustration.

The evolution of size of the peanut defect as a function of tunnel bias is shown in the conductance maps through fig-5.3(c) to (f), taken from -0.4 V to -0.1 V (at 400 pA). In these images, the peanut size is seen to increase as the tip bias decreases (while the current is kept

constant). This may seem counter-intuitive since at lower bias there are less states integrated, and the tip is closer to the surface, which leads to the expectation that the resolution should improve and the defect should appear smaller. The increase of size in conductance map turns out to follow the electronic feature of the BP surface observed from the defects. The conductance maps reveal the formation of standing wave patterns in the LDOS around the peanut defects. The typical wavelength of these patterns decreases with increasing energy. For negative bias, inverse relation with energy implies negative curvature for E-k dispersion in the valence band. The band structure has been studied through ARPES measurements and the shape of bands, with negative curvature, can be verified from these results.[157]

This trend is opposite to what is commonly seen in some noble metals, for example Au(111) where the shockley states show positive curvature in the E-k dispersion relation.[158]

From literature concerning the study of defects in black phosphorus, peanut defects are generally referred to as the only type that are found on surface.[129,130] In our experiments, we find several types of defects other than peanut defects.

We present an area of BP in fig-5.4 where different types of defects can be identified. All images correspond to the same area and are recorded with different tunneling parameters to highlight the characteristics of the observed defects. The top row of images (a-c) show the STM topography at constant current and taken at -0.2 V, -0.4 V and +1.0 V respectively. Shown in the second row are the corresponding conductance maps (d-f) for the topography with above mentioned bias setpoint, respectively. To simplify our observations, the characteristics features are identified and detailed as follows:

1. First and foremost, the peanut defects can be easily identified with oval shaped boundaries in fig-5.4(a). The shapes of these five peanut defects are seen with better contrast in fig-5.4(b) due to lower bias and increased current setpoint. Taking a closer look at these defects combined with corresponding conductance maps in fig-5.4(d) and (e), one can find the subtle differences in the contrast between them. Specially, no. 5 appears with lighter contrast both in STM topography as well as conductance map in comparison to others. This is indicative that these defects undergo slight variation in their properties , probably due to the interaction with some potential disorder induced by other defects.

2. *Sub-surface defects:* There are peanut type defects with brighter contrast in the conductance map (5.4d) but faintly visible in the STM topography (fig-5.4a). These defects are identified as sub-surface peanut defects and are marked with arrows in fig-5.4(b). These second type of defects however, show similar contrast as that of the top surface peanut defects in fig-5.4(e). Their similarity with the peanut defects described above suggest that they have the same nature but are located at a different depth.

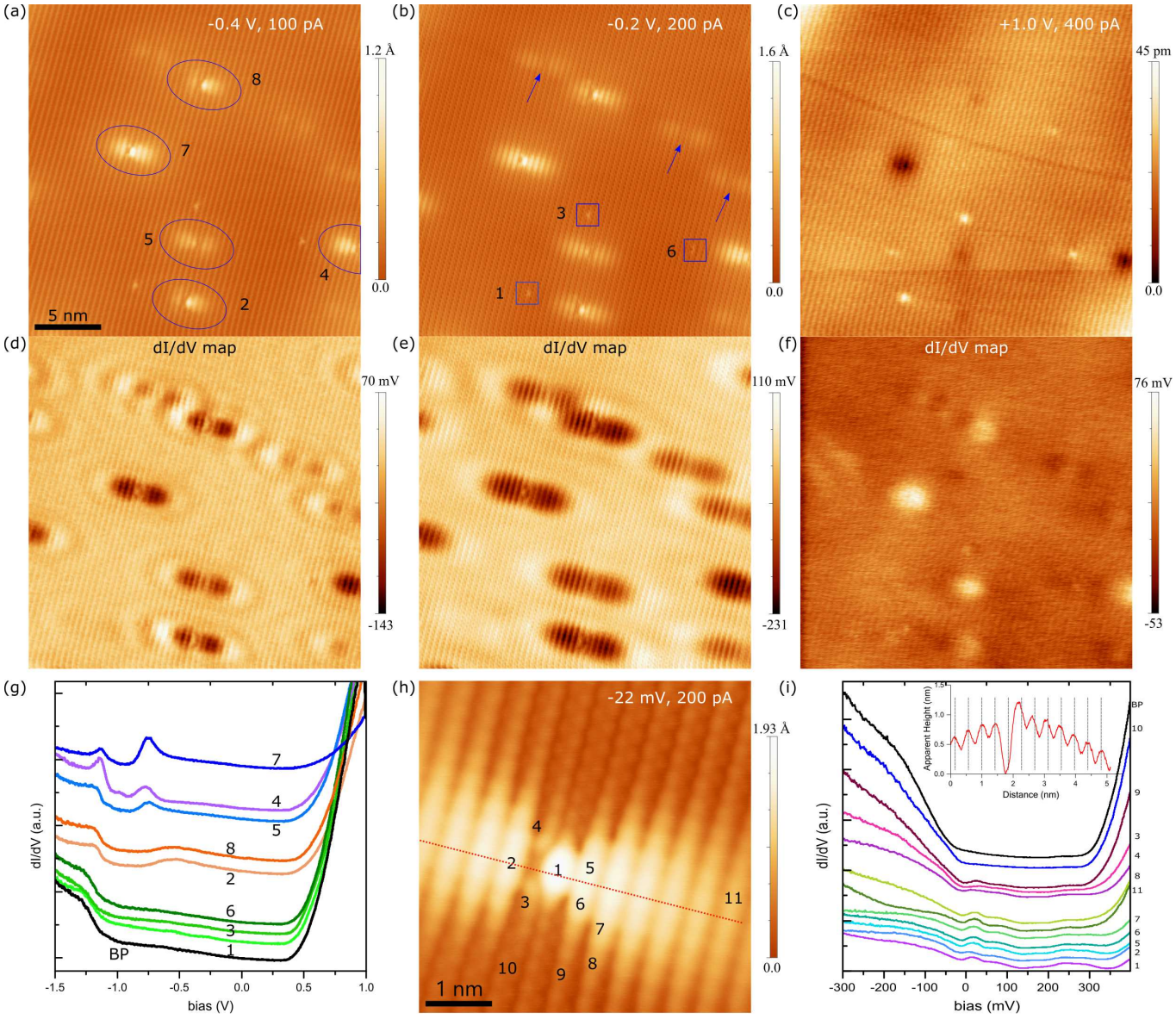

Figure 5.4: Types of defects in black phosphorus

Representative STM topography image showing defects in 25 nm×25nm area at (a) -0.4 V, (b) -0.2 V and (c) +1.0 V. The ellipses, squares and arrows in (a)&(b) identify various types of defects in these images. Corresponding conductance (dI/dV) maps are presented in (d), (e) and (f), respectively. (g) STS on the defects marked in (a)&(b), the spectra are vertically shifted to allow better view. (h) High resolution STM topography image of a peanut type defect taken at -22 mV and 200 pA (scale= 1 nm). The STS on this defect at spatially different locations is presented in (i) and grouped on the basis of similarity in electronic features. The location for STS on defect and the corresponding curve are identified by numbers in the two images. Inset shows a line scan profile of the defect in the arm-chair direction and identified by dotted lines in (h). Vertical lines are drawn corresponding to the center of P1 and P2 atoms in a given atomic row.

3. *Point defects:* In fig-5.4(b), three defects are identified with square boxes that are labelled as point defect owing to their appearance in (a) and (b). These defects do not have specific feature in the conductance map. In contrast with the peanut defects, these point defects do not exhibit *contrast inversion* with bias polarity, they always appear bright.

We investigated electronic properties of these defects by STS measurements including peanut type defects that have been reported. The STS on defects is presented in fig-5.4(g). The bottom most curve is the STS taken on black phosphorus away from defects (shown in black). The three green curves (1, 3 & 6) correspond to point defects. The electronic features for point defects are very similar to that of pristine black phosphorus. The two curves in shades of red (2 & 8) correspond to peanut defects. In addition to the BP spectral characteristics they exhibit a broad bump at -0.5 V. The curves in blue shade correspond to peanut defects (4, 5 & 7) and are identified with peaks at -1.2 V and -0.8 V. The difference in the STS for peanut defects are somewhat observed in the STM topography, as well, upon careful examination. It is clear that the peanut defects can be identified with localized peaks in the tunneling spectra. The spectra corresponding to sub-surface defects show similar features but with larger broadening and shift in energy position.

More details on the peanut defects are shown through STM and STS data in fig-5.4(h)&(i), respectively. Here, spectra taken at different various positions around the defect are shown. The zig-zag arrangement of phosphorus atoms can be clearly seen around the bright central spot. The atomic rows here appear to be distorted around the vicinity of the defect. The small dark patch between the center appears as missing phosphorus atom/s, however, it is difficult to assert that these are purely structural in nature from STM topography image.

A line scan profile along the armchair direction (red dotted line) for this peanut defect (5.4h) is shown in the inset of fig-5.4(i). On this graph, we use vertical lines to mark the center of atomic rows. Clearly the bright spot is off centered, and is therefore located on one sublattice of BP. The observed differences in height can be due to the spatial rearrangement of phosphorus atoms, or due to redistribution of charge density around the peanut defect modifying the LDOS in that area. The fact that at positive bias the atomic lines are straight over the defect seems to indicate that the features observed at negative bias are due to electronic effects.

The combined STS for numbers 1 - 11 in fig-5.4(h) is presented in fig-5.4(i), in the energy range -0.3 V to 0.4 V. The idea of this short range spectra is to identify features in STS close to the fermi level with improved resolution as compared to a wide range observation (-1.5 V to 1.0 V) such as fig-5.4(g). The STS on different sites are grouped in three categories: (1) on high contrast areas of defect, (2) close to defect but with lower contrast, and (3) away from defect and regular BP lattice. The spectra taken away from defect (top curves) is very similar to the STS shown for pristine black phosphorus (fig-5.2b), and this serves as a reference.

The spectra taken on bright regions of the defect (1,2,5,6,7,8 & 11) show no sharp peaks in the observed energy range but there appears to be a small "bump" near the fermi level which is repetitively present in all these spectra. The intensity is quite small but noticeable with a broadening of around 20 mV. It is clear that this feature is observed on the bright regions of the peanut defect. This *state* is present above E_F and appears in the band gap. STS on sites close to defect and with lower contrast (3,4 & 8) show this state at the same energy position but the intensity has further reduced for these positions. It is reasonable to argue that these *defect states* created in the band gap due to peanut defects and are highly localized.

Origin of defects

Two interpretations have been presented for the origin of peanut defects based on STM related observations.[129,130]

- **Vacancy :** The first one identifies these defects as a monovalent vacancy in the BP lattice. Here, the peanut shape of the defects is described as electronic effects resulting due to missing phosphorus atom. The vacancy at sub-lattice positions P1 or P2 (fig-5.1(b)) leads to anisotropic charge density, along the zigzag direction, which resembles the two lobe feature of peanut defect. Thus, it explains the mirror image shapes of A and B peanut defects in fig-5.3(b)

- **Dopant :** In this interpretations, a hole bound to negatively charged acceptor impurity can lead to Rydberg-like bound states which manifests as elliptical and dumb bell (peanut) shapes in the STM topography image. These shapes are associated with the ground and excited bound hole states which can be accessed depending on the polarity of the STM tip. The probable cause of this unintentional p-doping is attributed to Sn related impurities used in the synthesis.

So far, these two interpretations partially explain some of the observations particular to a peanut defect, yet a wholistic understanding for the origin and the electronic behavior of these defects is still missing. In our results, we have extensively characterized peanut defects based on the apparent shape and corresponding STS in narrow and wide energy range. In comparison with the results obtained previously, we see stark differences in the STS on the defects. A short summary of the results based on the two theories are presented in fig-**??**.

In our attempt to characterize the native defects of black phosphorus, we extend the study on to point defects and is presented in the next section.

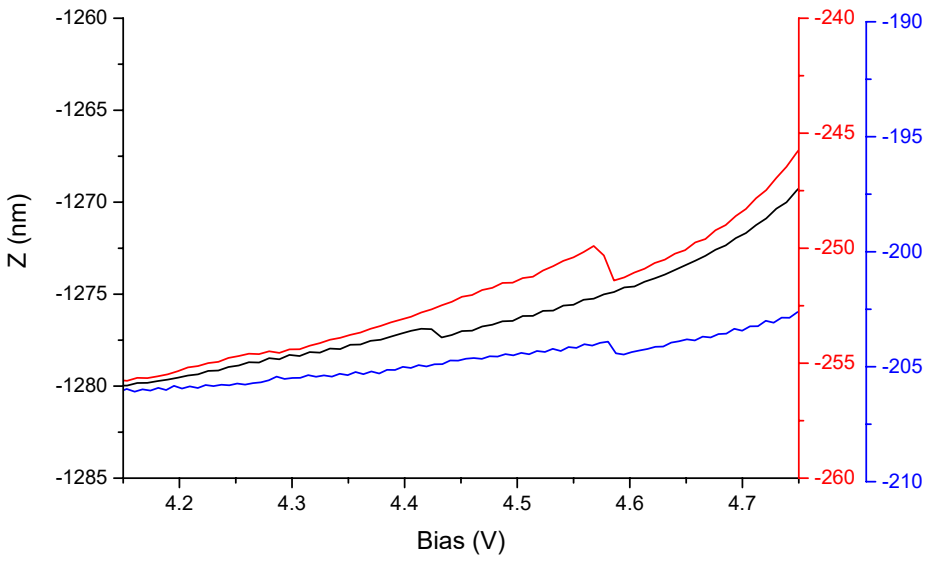

Figure 5.5: Z(V)spectra shown for three defects that switch during the measurement and identified as abrupt change in the curve.

5.4 Manipulation of point defects

Few point defects on the top surface have been found to undergo an irreversible transformation into a peanut defect. This conversion takes place while performing a Z-V (work function) measurement on the point defect.

It is observed that some point defects are susceptible to change into a peanut type defect usually when the bias at the tip is usually between 4 to 5 volts. This phenomena can be observed in the collection of spectra performed on three point defects shown in fig-5.5 for the energy range 4.2 V to 4.8 V. In the plot, we observe sudden transitions that correspond to the switching of defects. The mean value of the tip bias where this transition occurs is around 4.5 V.

The topographic images showing the change in defect shape (point to peanut) is presented in fig-5.6. In this figure, (a) and (c) are STM images recorded before and after the Z-V measurement. The point defect is identified within blue and red ellipses in the two images, respectively.

The STM image taken during the measurement is shown in (b). The energy range chosen for the Z-V measurement is from 1.0 V to 8.0 V. Thus, imaging parameters were set to 1.0 V for this purpose and then STM tip was parked over the defect for the measurement. The imaging of the area continues and we clearly see the change in the contrast for the defect, now appearing as dark which is similar to peanut defects.

The STS for the point defect is presented in fig-5.6(d) and compared with a reference peanut defect spectrum marked by green arrow in fig-5.6(a). In this figure, the top curve (black) is taken on pristine surface away from defects and marked by a cross in fig-5.6(c) and the curve below

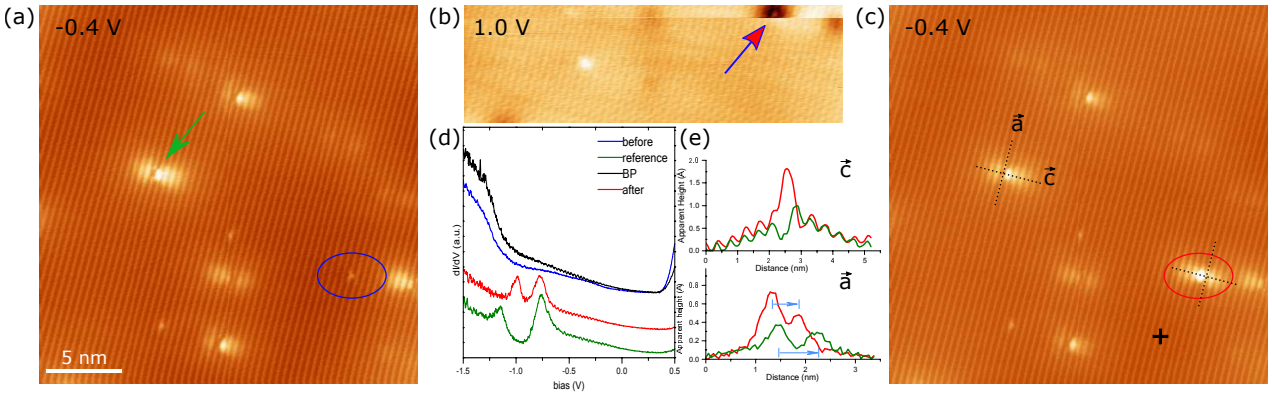

Figure 5.6: Manipulating defect states: (a) Topography image of an area on BP with point-type defect (encircled in blue) before being transformed along with other defects for reference (green arrow), taken at -0.4 V and 100 pA. (b) Positive bias image (1.0 V, 100 pA) of (a) where the point defect changes to another state identified by blue arrow. (c) Topography image after transformation (-0.4 V, 100 pA), point defect encircled in red (d) The STS on point defect (before and after) is compared with reference peanut defect (green) and pristine BP spectra (black cross in (c)), curves shifted vertically for clarity. (e) Line scan profile comparison of switched point defect with a typical peanut defect in arm-chair and zig-zag direction, centered at their respective bright spot.

(blue) is for the point defect before the switching has taken place. The spectra taken after the voltage pulse is shown in red curve. Comparing the STS for the switched point defect with that of a reference peanut defect we find similar characteristics between them. Both curves have two sharp peaks deep in the valence band. The peanut defects have resonance states at -0.8 and -1.2 V, as seen earlier, whereas for the switched defect the peaks are at -0.8 V and -1.0 V (shift towards the fermi level).

The right shift in STS for the switched point defect is consistently observed over other instances whenever a point defect is manipulated in the above mentioned fashion. After switching, the apparent shape is almost similar to the commonly found peanut defects yet there are few subtle differences that can be observed in the line profile comparison presented in fig-5.6(e). The top subfigure shows the comparison in the armchair direction ($\vec{c}$) while the bottom one shows for the zigzag direction ($\vec{a}$) as marked by dotted lines in fig-5.6(c). In the armchair direction, the apparent height of the switched (point) defect (red curve) at the central bright spot is almost twice that of the reference peanut defect (green curve). In the sub-figure below, the line profile comparison in the zigzag direction shows that the small dark patch near the central bright spot is smaller for switched defect. The separation is measured as the distance between the two peaks and are identified by blue arrows in this figure.

Interpretation of the origin of these defects is still needed. One proposition is that they correspond to peanut defects that may include a vacancy. This vacancy be initially filled with some *adatom* and the tip pulse may remove it revealing the peanut shape. In an another inter-

pretation, the switching of defect can be observed as rearrangement of P-atoms which is in less stable configuration. The voltage pulse then provides excitation to reorganize atoms for this less stable configuration forming stable peanut defects.

5.5 Air induced changes

Black phosphorus is known to degrade upon exposure to air, moisture and in solvents. Degradation of BP under these conditions are limiting factors for device fabrication and its use in ambient conditions. Due to high chemical reactivity of phosphorus with oxygen and water, a variety of chemical pathways exist under different conditions of exposure as well as the time duration. In a PES measurement, performed over 2 days of exposure time, the BP flakes showed sub-nanometer (0.4 nm) oxide growth which were identified as P_2O_5.[159] Pure oxygen alone has strong interaction with black phosphorus. The formation of oxide on BP surface (P_xO_y) also protects the layer underneath by oxidising few layers on the top which prevents further oxidation. However, under a constant flux of oxygen plasma, the layers underneath can be etched away after the oxide layer has formed.[160] In this case, the reaction rate of the etching of oxidized phosphorus from the top is balanced by the oxidation of layers exposed below, thus having constant rate of layer reduction over time.

The interaction of black phosphorus with water (in a solvent) is different than what is observed with oxygen. Usually, solvolysis of phosphorus takes place which is mediated by the formation of P-O-P bonds due to dissolved oxygen and resulting in the formation of various phosphor based compounds like phosphinic and hypophosphoric acid.[161] These compounds are identified with different oxidation states on phosphorus and may range from +1 to +5 depending upon various factors like exposure time[162] and light illumination.

It is observed that the degradation of black phosphorus proceeds with a rather higher rate when exposed to air and moisture, at the same time.[163]

With STM, it is possible to observe the changes that take place at the atomic level due to the oxidation of black phosphorus upon exposure to air. A recent study showed some measurements in this direction but the results offer little comfort due to poor resolution of the topography images.[150] We perform controlled cycles of STM measurements to identify the surface modification of black phosphorus that place when exposed to oxygen and ambient (air).

In the first step, the UHV cleaved sample was introduced to low dosages of oxygen molecules to an exposure corresponding to 30L , 120L and 1200L (all at pressure of 10^{-6} mbar while the exposure time was varied) at room temperature. Each exposure was directly followed by imaging of the surface at 4.5 K to observe changes, if any. In the first three trials with oxygen molecules, we do not see any change on BP surface that may hint towards a new chemical species bonded

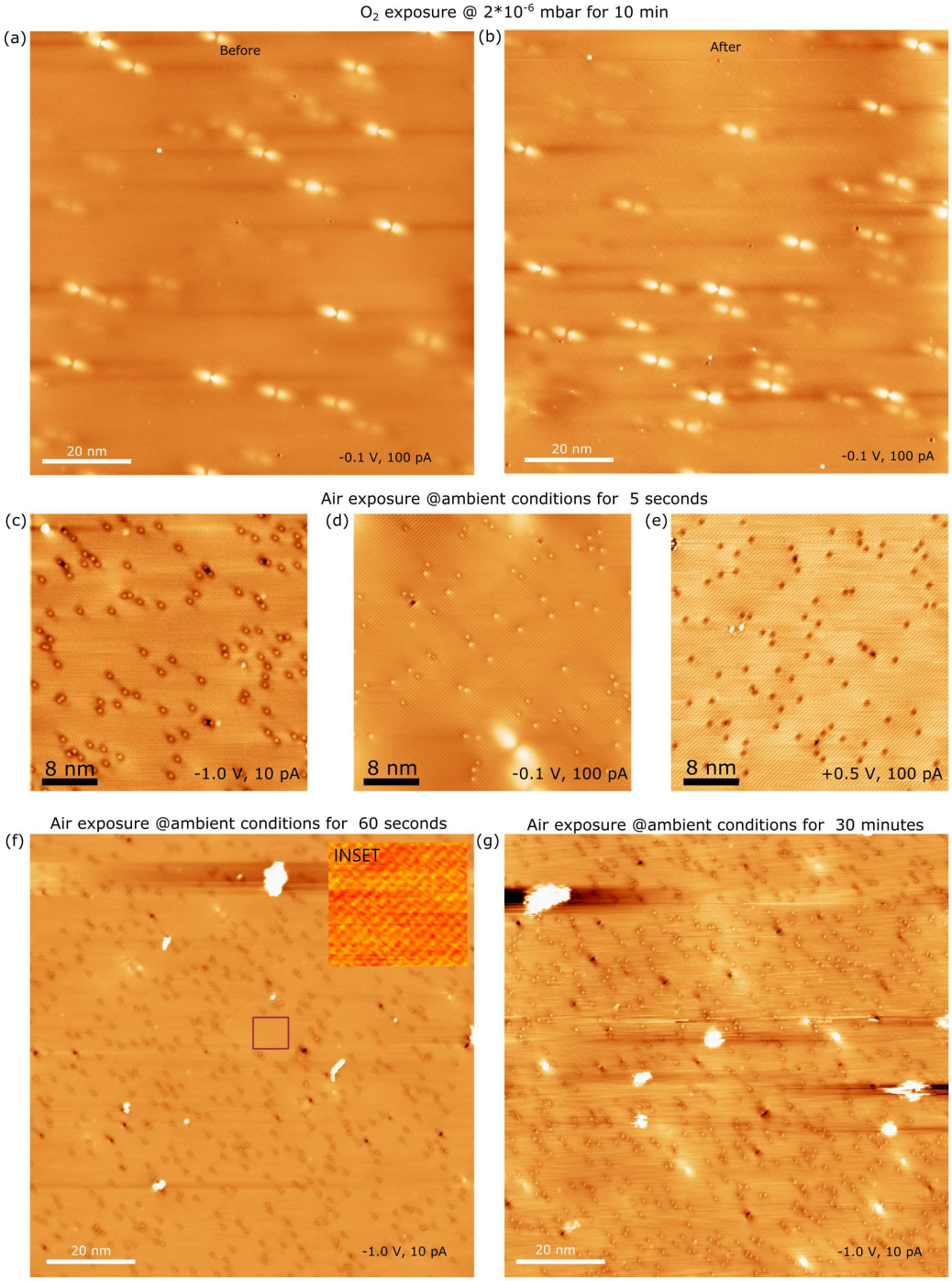

Figure 5.7: Air exposure Before (a) and after (b) topography image of UHV cleaved black phosphorus sample exposed to 1200 L of oxygen molecules. (c)-(e) Same sample exposed to ambient air for 5 seconds and imaged at different bias voltages. Further exposure to air under ambient conditions for (f) 60 sec and (g) 30 minutes. Samples were annealed upto 125 deg C in case of (f) and (g).

to the surface. The before and after topography images for 1200L exposure is shown in fig-5.7(a) and (b). In both of these images, we clearly see peanut and point defects along with few dark spots that are most probably groups of phosphorus atoms missing in the lattice. For such a large exposure dose, the influence of oxygen molecules on black phosphorus surface seems negligible.

Consequently, we move on to the second stage of experiments where the sample has been exposed to ambient air at normal temperature and pressure. In the first air exposure, the sample was kept in ambient conditions for 2-3 seconds.[(c)]In fig-5.7(c), (d) and (e), the STM topography on different areas of the sample are presented that clearly show new features on the surface. The peanut defects can be seen in fig-5.7(c) at the top left corner as a bright spot while in fig-5.7(d) it is clearly visible at the bottom. These new features that appear like circular spots have a higher areal density as compared to peanut defects. For peanut defects, the surface density lies typically in the range of $10^{10}cm^{-2}$ which is equivalent to 10 defects in an area of 100 nm $\times$ 100 nm. On the other hand, the air induced defects or adsorbates have surface density which is two orders magnitude higher than peanut defects. In fig-5.7(d), the surface density of adsorbates is around $4 \times 10^{12}cm^{-2}$ (68 defects in an area of 40 nm $\times$ 40 nm).

The adsorbates are observed as bright spots in negative bias STM images (fig-5.7(c) and (d)) and dark in the positive polarity (fig-5.7(e)). They can also be identified with a dark halo around the bright spot at negative bias (-1.0 V in fig-5.7(c)). In fig-5.7d, we also find some irregular dark patches that appear as a cluster of phosphorus atoms missing from the lattice. The characteristic features of this missing islands are that they appear dark in both polarity of STM images. They are seen on UHV cleaved sample as well, so we rule out the possibility that they are formed as a result of exposure to air.

In the third stage of experiment, these samples were exposed to ambient conditions for prolonged duration. In fig-5.7(f), a large scale image is shown after the sample has been exposed for 1 minute. After the exposure, the sample is transferred to the UHV preparation chamber where it is annealed at 125 deg Celsius, followed by STM measurement at 4.5 K. The previously exposed samples (as presented in fig-5.7(c),(d) and (e)) were used for this measurement. After the exposure, we find some impurities on surface along with induced adsorbates appearing as bright with dark halo around. As such, there is no noticeable difference between few second exposure and 1 minute exposure. The adsorbate surface density in this image is approximately $5.5 \times 10^{12}cm^{-2}$ which is very close to the previous exposure. Finally, this sample is exposed to air for 30 minutes followed by an annealing upto 130 deg Celsius. The topography image is shown in fig-5.7(g). The defect density for the adsorbates is calculated to be around $7.2 \times 10^{12}cm^{-2}$ for this area. Considering the fact that the exposure time had been increased by 20 times (5 sec to

[(c)]The entire operation was performed in the load lock of the instrument wherein the outlet valve was opened completely for air exposure.

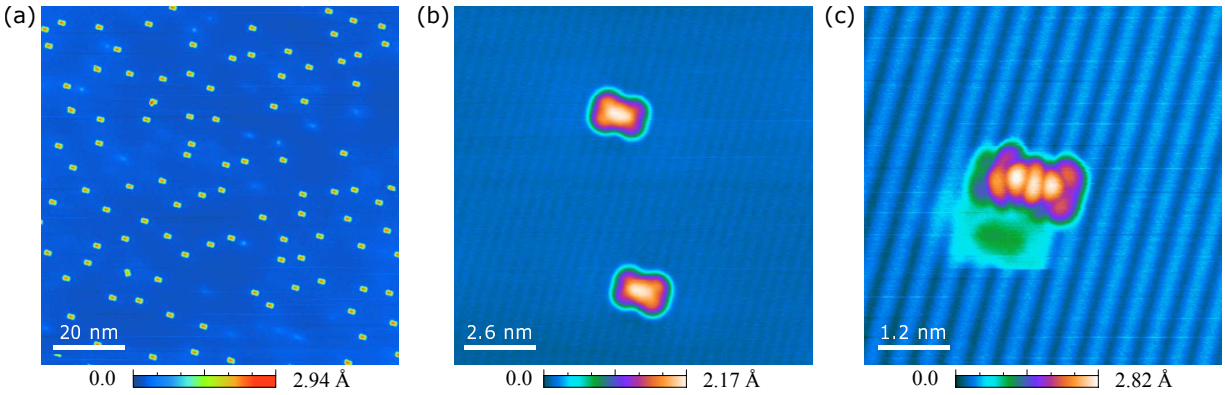

Figure 5.8: F_4TCNQ on BP: (a) STM topography image of single F_4TCNQ molecules on black phosphorus taken at -2.0 V and 10 pA, (b) Two equivalent adsorption sites for F_4TCNQ in the BP sub-lattice (-2.0 V, 10 pA), and (c) Molecular shape of F_4TCNQ obtained with a functionalized tip (-2.0 V, 10 pA).

60 sec in 5.7f)and 600 times (5 sec to 1800 sec in 5.7g), the corresponding effect on the surface is negligible since the defect density stays in the same order of magnitude ($\approx 10^{12} cm^{-2}$) which hints towards a saturation effect taking place in the first few seconds or less.

It is interesting to observe that surface density of adsorbates reaches saturation when exposed to ambient conditions. The effect of exposure has been the presence of spot sized adsorbates. From the perspective of surface atomic density, by a rough estimate, one adsorbate is present for every 200 atoms of P-atoms. This is far from the formation of layered oxide structure. Earlier in PES measurement, researchers found a growth of 0.4 nm oxide over the BP surface. It can be argued that the mechanism for the chemical modification of BP surface is much more complicated than proposed. In our experiment, we find flat areas of BP lattice similar to the cleaved surface where the atomic rows can be clearly seen. The changes are not very dramatic as has been predicted though the transport on the top surface will be affected since these adsorbates can act as scattering centers for charge carriers. We have provided one of the first atomic level measurement on the topic of surface degradation for BP. However, it is still necessary to perform more experiments in this direction with longer exposure times to see the evolution of surface modification.

5.6 F4TCNQ on Black phosphorus

In this section, we study the behavior of organic molecules adsorbed on black phosphorus surface. For this purpose, highly electrophilic F_4TCNQ molecules have been evaporated onto black phosphorus at very low concentrations. This enables us to study single molecules that are situated far apart so that inter-molecular interaction can be neglected.

In a large scale STM topography image shown in fig-5.8(a), F_4TCNQ molecules can be observed scattered on the surface. In this image, the two closest molecules are around 3.5 nm apart with the average surface coverage of 100 $nm^2/molecule$. From the orientation of the molecules on the BP lattice, we observed that the long axis of the molecule is *always* aligned in the arm-chair direction. This adsorption behavior is similar to an earlier DFT based theoretical work on TCNQ-BP system.[164] In this work, the most stable adsorption site for TCNQ is the *top site*, where the P-atom lies in the center of the hexagonal ring of TCNQ molecule. Thus there are two equivalent sites corresponding to sublattice of BP, molecules can sit on top of P1 or P2 atoms. In STM topography for F_4TCNQ on BP, we also observe two equivalent adsorption sites which is identified by an asymmetry in the apparent shape of the molecule. In fig-5.8(b), the two configurations can be seen in the small scale. The bottom molecule has smaller lobe size on the left side while the molecule on top has smaller lobes on the right side. It is clear that TCNQ and F_4TCNQ have similar nature for adsorption on BP lattice. The asymmetry in the molecular shape can be understood as bending or tilt of the molecule. This could happen because when it is adsorbed in top site configuration, one side of the molecule lies directly above phosphorus atomic row while the other side lies between the middle of atomic rows.

For F_4TCNQ-BP system, stable images are obtained when the sample bias has negative polarity. Thus, all STM measurements have been perfomed in negative polarity. Also, it is convenient to observe atomic resolution for black phosphorus in similar conditions. In fig-5.8(c), we could clearly see the orbital structure of the molecule when imaged at -2V, the molecular shape here resembles to LUMO orbitals commonly observed for F_4TCNQ which is filled in this case. This suggests that there is some amount of charge transfer between black phosphorus and the LUMO of the molecule. This image has some ghost shadows in the vicinity of the molecule owing to a functionalised multiple tip. Due to multiple tip effect, the long axis of the molecule seems to appear below the molecule in green shade. However, we observe the same shape with otherwise calibrated STM tip but with poor resolution as in fig-5.8(b). So we chose this particular image only for representative purposes to help understand its orbital shape.

These samples have been warmed up to room temperature and we still find single physisorbed molecules on BP surface. Also, the molecules are observed to be stable during imaging which indicates significant molecule-substrate coupling.[(d)]Since F_4TCNQ is strongly electrophilic in nature, it is expected for the molecules to adsorb on BP sub-lattice having higher electron charge density. We correlate this argument with the adsorption behavior of molecules in the large scale area shown in fig-5.8(a). Taking a closer look on the distribution of molecules with respect to the native peanut defects on the BP surface, we find that the F_4TCNQ molecules *always avoid* the defect areas such as peanut defects that can be seen in this image.

Using these molecules as charge sensor probe, we can make a prediction for the peanut

defects to have a lower charge density as compared to pristine black phosphorus regions. In the dopant interpretation explained earlier, peanut defects are identified as negatively charged acceptors which can act as preferred adsorption site for electron-philic F_4TCNQ molecules. In our experiment, we observe an opposite trend and here the molecules avoid the peanut defects. This suggests that peanut defects don't have any negatively charged character. Observing charged states for peanut defects could be explained by presence of impurity atoms below the top layer. In pristine BP samples free from foreign contaminants, it is more likely that peanut defects are devoid of any negative charge.

We further investigate the properties of F_4TCNQ on black phosphorus by means of tunneling spectroscopy and the results are presented in section below.

5.6.1 Activated molecules

Concerning energy level alignment of F_4TCNQ on black phosphorus, we note that F_4TCNQ LUMO energy level is close to the valence band edge of BP, and the HOMO level lies much deeper. In a simple approximation, we expect to probe the LUMO level near the fermi level and higher unoccupied orbitals (LUMO+1) in the positive bias. When performing *I-V* spectroscopy, it is found that molecules become unstable in the energy range from -2.0 V to 2.0 V, even with low tunnel current setpoint of 10 pA. In the topography image that followed, it was found that the corresponding F_4TCNQ molecule had become mobile, and was moving under the influence of STM tip. Interestingly, the I-V measurement also had effects on some neighboring molecules as well. These molecules, situated few nanometers away, showed similar mobility on BP just like the molecules on which spectrum was taken. This implies that effect of bias voltage on tip is spread over certain distance around the tip position.

Since we record STM images in negative sample bias, it is believed that this unstable behavior of molecules are due to positive bias conditions. To verify this, we systematically made voltage pulses in the range +0.5 V to +2.0 V (for 0.1 second) near F_4TCNQ molecules. Beyond 1.5 V, molecules can be excited locally and the specific number may depend on the proximity to the spot of the spectroscopy. At +2.0 V, the charged behavior of molecules are repeatedly observed having an influence for radial distance up to 5 nm. In order to *activate* a molecule, we adopt this technique of making a voltage pulse of 2.0 V.

In fig-5.9(a) & (b), an example of such molecular activation is demonstrated. In 5.9(a) two molecules can be seen on BP lattice. The tip is parked at the position marked by green spot and 2.0 V pulse is applied. In the next topography image shown in 5.9(b), we see that the molecule close to this green spot has been activated and follows the STM tip. We can identify

[(d)] Compared with F_4TCNQ-Graphene system (chaper-4), the molecule-susbtrate interaction is definitely higher for black phosphorus.

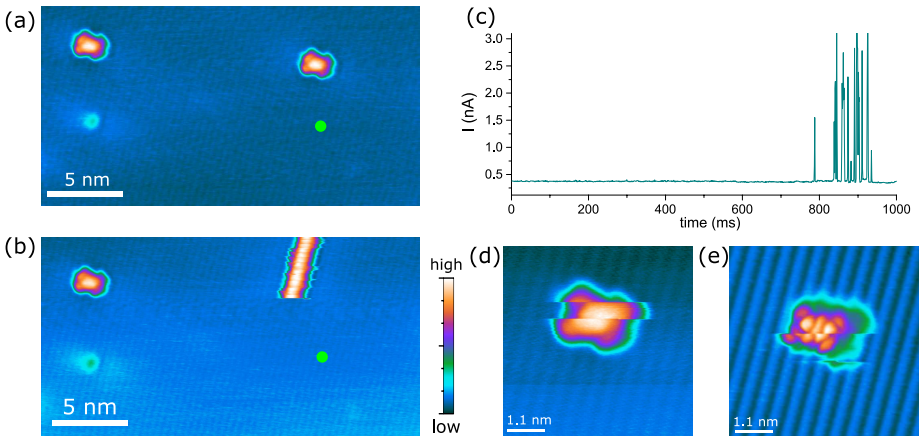

Figure 5.9: Induced mobility of F_4TCNQ on Black Phosphorus : Topography image showing (a) before and (b) after image of an area on BP, with two molecules, where a voltage pulse of 2.0 V is applied at the spot marked by green dot (-2.0 V, 10 pA). (c) Current v/s time plot for an activated (mobile) F_4TCNQ molecule measured at constant bias voltage of 2.0 V. (d) STM image of an activated F_4TCNQ molecule perturbed by tip while imaging (-1.6 V, 10 pA), and (e) STM image showing highly resolved intr-molecular shape of molecule in (d), observed with a sharp tip (-1.6 V, 10 pA)

the instability of an activated molecule through a time dependent measurement of (constant) tunneling current on the molecule, such as shown in fig-5.9(c). The spike in the current v/s time implies that molecule is unstable below the tip. For a stable molecule, the current would be constant over time, but here the relative position of molecule changes randomly because of which the tip records drastic changes in tunneling current.[(e)]

These effects indicate that the induced mobility is a local effect of the applied electric field from the STM tip. In the present case with F_4TCNQ on BP, the measured samples are stable upto room temperature without any observable loss of molecular concentration. Mobility of molecules are specifically observed when spectroscopy measurements are performed. Therefore, the motion of molecules seems to be coulombic interaction which implies that the molecules are *permanently* charged by the electric field.

Another explanation could be that the chemical integrity of F_4TCNQ maybe destroyed by the electric field of the STM tip which makes it charged and/or unstable on BP surface. Therefore, it is important to obtain information on the *moving* molecules or somehow image these molecules. So, we first investigate the chemical frame of the charged molecules and then study the motion of these species. Given the fact that the molecules constantly follow the tip while scanning, it is difficult to image them and resolve their shape/structure. With sufficiently low tunnel current and slower scans, we were able to optimize scanning parameters to keep the *charged* molecule relatively stable while imaging. The corresponding images are shown in fig-5.9(d) and (e).

[(e)]The feedback loop is open during the measurement.

The difficulty presented by the mobile nature of molecules can be observed in fig-5.9(d). After multiple scans, the STM tip gets modified showing a multiple tip phenomena and getting functionalised as well. This functionalised tip then provides well defined sub-molecular resolution for the charged molecule. The orbital shape for the molecule can be clearly seen in fig-5.9(e) which undoubtedly resembles to a neutral molecule (as shown in fig-5.8(c)). Since the structure is intact, we are led to believe that F_4TCNQ molecules get charged permanently without undergoing any physical or chemical transformation.

5.6.2 Dynamics of charged molecules

To understand the dynamics of charged F_4TCNQ molecules, we make series of observation by making voltage pulse around molecules in a large scale area. A representative dataset is presented in fig-5.10 that shows the effects of two voltage stimulus marked by red dots in the images through. It is to be noted that in the absence of any positive bias voltage pulse or STS measurement, the molecules are completely stable and show no mobility on the surface. Here, we start from an area where some molecules are already activated due to earlier STS measurements.

The first image (5.10a) is taken before two voltage pulse have been applied at the spots indicated by red circles. As we observe in the subsequent images, 5.10b&c, different molecules surrounding the spot of pulse get activated. The induced effects are discussed systematically in the following subsections-

Electric field: Location and Effects

After the voltage pulse, most of the molecules in the vicinity get activated or charged. A rough estimate for the influence of the electric field is illustrated by the dashed elliptical areas through (a)-(c). Further, the activated molecules are marked by numbers in the image to help follow their motion in these images.

There two regions-A and B in 5.10(a) that shows the influence of tip pulse on surrounding molecules. We can also see two mobile molecules (4 & 5) on the upper part of the image that are active due to previous activity. The motion of three molecules in area A, marked as 1, 2& 3, can be followed in the three images (a)-(c). These three molecule show different type of behavior on BP surface. Molecule-1 after excitation starts following the tip and is stopped by a stationary molecule. We will discuss this *inter-molecular interaction* later in this section. Molecule-2 also starts following the tip during scanning and stops on its own on a homogeneous area in fig-5.10(b) and then moves ahead from this position in fig-5.10(c). Finally, this molecule goes out of the scanning area. Molecule-3 seems to have moved from its original position in the direction away from the pulse position, and stays in its new position. It appears that the molecule got charged for a very short period of time which couldn't be observed in STM time scales.

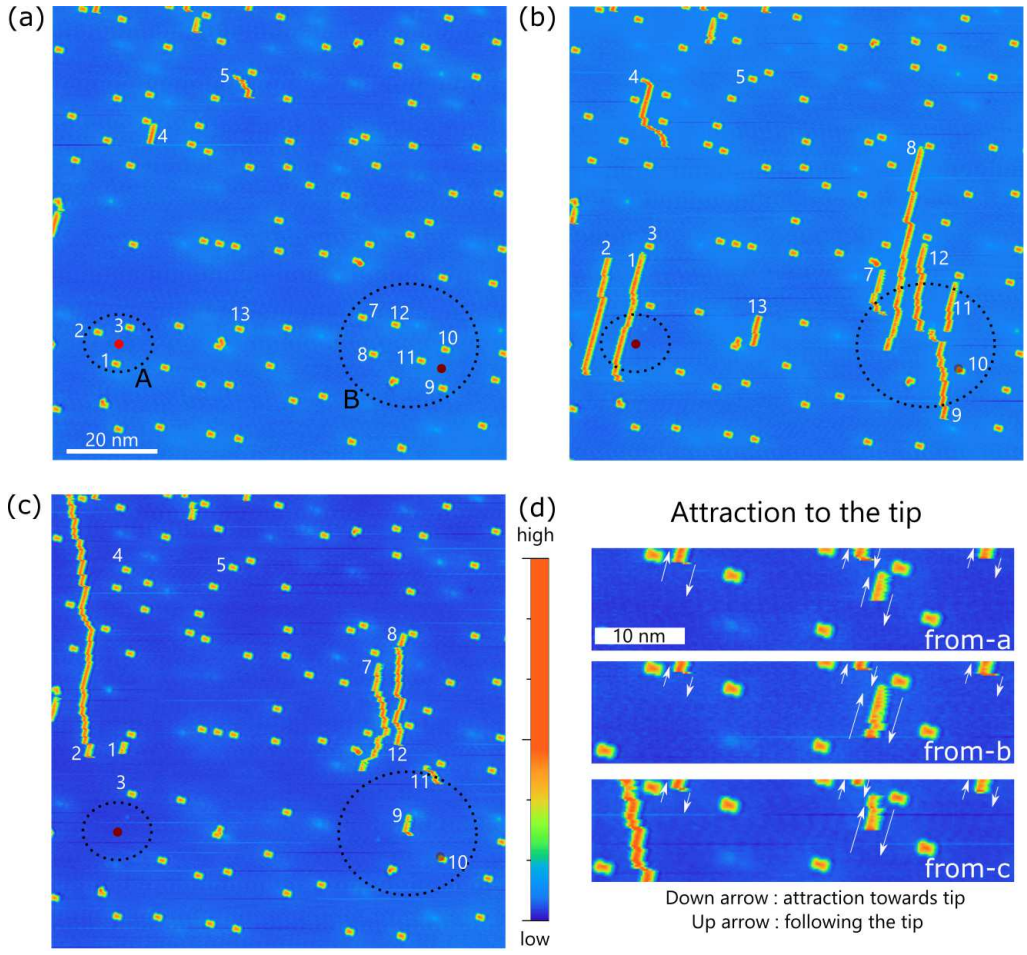

Figure 5.10: Activating F_4TCNQ by controlled voltage pulse: (a) A large scale area showing F_4TCNQ molecules on black phosphorus where two voltage pulse are made identified in red dots. After the pulse, (b) and (c) show the effects on the nearby molecules. All image taken at -2.0 V, 10 pA (Scale = 20 nm)

The behavior of molecule in region-B is very similar to A, with more molecules getting activated this time. Molecules 7, 8, 9, 11 & 12 get activated and move with the tip. Molecule-10 shows the same short lived state like molecule 3 and jumps closer to the position of voltage pulse. Between the regions A and B, we have a molecule marked as 13 which is far from the pulse spots. This one also gets activated, starts to move upwards in 5.10(b) but somehow goes out of the scanning area in 5.10(c). It is interesting to observe such long distance effects for the voltage pulse.

The effect of the voltage pulse is seen to have asymmetric effects with the same STM tip and bias voltage. The electric field lines from the tip can be assumed to have a symmetric profile in three dimensions which fall perpendicular onto the BP surface. The magnitude of electric field depends on the radial distance from the pulse position, assuming the tip apex is symmetric.

Molecules are getting charged by the effect of applied electric field from the tip. The strength of this external electric field passing perpendicularly through the molecule varies depending on the radial distance from the pulse spot. Asymmetrical distribution of charged molecules implies that the energy cost for charging the molecule is different, and maybe influenced with local environment and interaction with the substrate underneath.

It is also possible that the atomic structure of tip apex is asymmetric leading to charging of molecules according to its shape. However, this doesn't explain the behavior of molecule 13 which is far off but gets activated while the closer ones are still stationary.

Hopping of molecules

In this section, we focus on the motion of activated molecules on BP lattice. By comparing the initial position of activated molecules in successive images, we always find that there exists an offset of few nanometers in the images. It seems they first move downwards towards the tip and then follow the tip in upward direction. The up-down arrows in fig-5.10(d) illustrate this behavior for several activated molecules from figures (a)-(c).

This can be explained on the basis of attractive coulombic forces acting between the tip and charged molecules. The topography images are all obtained at -2.0 V bias on the sample which actually is a positive bias (+2.0 V) to the STM tip since the sample is electrically grounded. The negatively charged molecules are then attracted to the approaching STM tip with positive polarity. This attraction leads to a downwards movement when the tip is within a threshold distance. After this shift, the molecules stay with the tip as it scans progressively in the upward direction. In this way, we see the long streaks of molecules following the tip in the topography images.

The hopping of activated molecules is guided along the zig-zag direction of the BP lattice, as observed in the images-5.10(a-c). The molecules diffuse along the phosphorus atoms in zig-zag direction or rows and occasionally take a left or right.

Inter-molecular interaction: Along the motion path following the STM tip, activated molecules on BP lattice are influenced by the presence of neighboring stable molecules. To illustrate the interaction taking place between these two types of molecules, a collection of topography image is presented in fig-5.11.

In closer proximity with (stable) molecules, the activated ones maintain an equilibrium distance when encountered head-on while in few cases they are also deflected sideways. Eventually, the activated molecules are stopped by the stable ones as we typically observe in successive scans. The nature of interaction here is repulsive and results from the coulombic forces acting between them. In order to understand this, we recall that the physisorbed F_4TCNQ molecules withdraws electrons from the substrate underneath due to its strong electro-positive nature making them

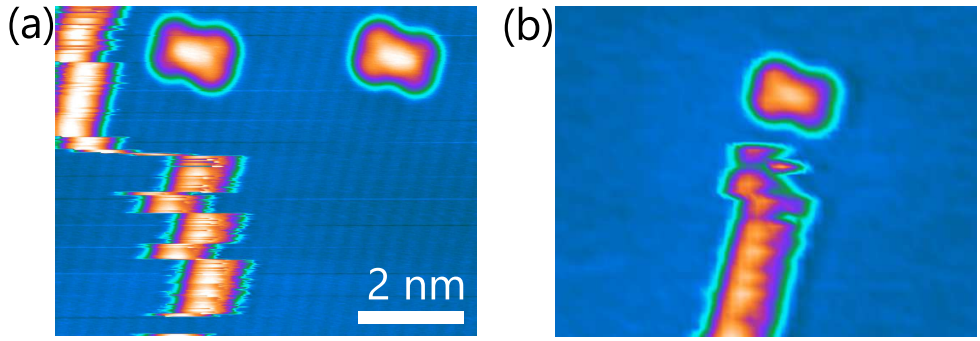

Figure 5.11: Intermolecular interaction between mobile and stable F_4TCNQ molecules on BP. STM topography image taken at -2.0 V and 10 pA for (a) an activated molecule that hops onto neighboring P-atomic rows avoiding adsorbed molecules, and (b) an activated molecule stopped by a stable adsorbed molecule on BP.

negatively charged. The activated molecules are further negatively charged which is facilitated by tip induced electric field. Presence of similar charge on the two types of molecule explain the repulsive interaction.

5.7 Conclusion

In this chapter, we have studied the surface properties of black phosphorus with particular focus on the molecular functionalization using electrophilic F_4TCNQ molecule. The important aspects of our results can be summarized into two main themes. In the first part, we obtain a deeper understanding on the nature of defects present on BP surface, and in the second, we study the electronic interaction of the physisorbed molecules using black phosphorus as substrate.

The electronic properties of the native defects have been extensively investigated by STM and STS where some of them shows deep resonance states inside the valence band. These defects are then characterized based on their shape, size and appearance in topography images. Among these defects, the most commonly studied is the one with two dumb bell shapes, called as peanut defects. The apparent shape in STM images and the corresponding electronic spectra are observed to be different from what has been reported in the literature. Further, we find some meta-stable point defects that can be manipulated, by voltage pulse from tip, to transform into a peanut defect and can be identified with similar tunneling spectra. The structural origin of these defects remains a topic of further investigation.

Molecular functionalization of black phosphorus with F_4TCNQ has been studied at low concentrations to understand interface properties related to molecules. A strong electron acceptor F_4TCNQ adsorbs as single molecules on flat black phosphorus substrate and avoids any type of defects, including peanut defects. This result gives an important clue regarding the electronic

nature of peanut defects, more specifically, if these defects possess anionic character or not. Further, we were able to activate F_4TCNQ molecules in a way that they become negatively charged and are mobile on the black phosphorus lattice. The polarity of the activated molecules is determined by the fact these molecule get attracted to the positive bias on tip. The movement of the activated molecules selectively takes place along the zig-zag direction of P-atoms.

Chapter 6

Conclusion

In this thesis, we have studied the assembly and electronic properties of organic molecules on graphene and Black phosphorus by scanning tunneling microscopy and spectroscopy at 5K. The interaction of electron acceptor and donor molecules, H_2TPP and F_4TCNQ, have been studied with multilayer pristine and nitrogen-doped graphene substrate. For black phosphorus, the defects on the surface were studied in detail first, followed by functionalization with F_4TCNQ.

Porphyrin (H_2TPP) exhibits tautomerism, i.e. switching of H-atoms in its macrocycle, which imparts distinct electronic properties to the corresponding tautomers. In the gas phase, the two tautomers are very similar and can be reproduced with 90◦ rotation around the central molecular axis, and also for the aromatic π electron distribution in the molecule. When physisorbed on a graphene surface, the molecular conformation changes and the two tautomers can be identified with significant differences in the molecular LDOS. Corresponding to high and low conductance, the molecules appear as bright and dark, respectively, in the topography image. The switching between tautomers is observed in time dependent current measurements (at constant bias) as two level plot similar to a telegraph signal.

The switching rate increases with the bias voltage as well as the tunneling current setpoint. To decouple these effects, we have measured switching rate per electron,or *yield*, as a function of bias voltage, and current while keeping the other parameter constant. The yield for tautomerism starts to increase for the bias voltage close to the position of molecular energy levels. On further increasing the bias voltage, the yield is observed to saturate around the energy position for HOMO and LUMO states. On the other hand, the yield is almost constant in a current dependent measurement for a given bias voltage. We perform similar experiments with porphyrin on N-doped graphene since the molecular energy levels are shifted HOMO -LUMO states. Here also, we find similar behavior for yield which suggests that the intra-molecular switching is coupled to the substrate interaction and offers a unique way to tune the properties of such molecules. The pinning of yield value suggests that the tautomerisation is activated by the resonant tunneling

of electrons in contrast to the inelastic activation mechanism for similar compounds that exhibit tautomerism, and are usually studied on metallic substrates.

We have also demonstrated the ability to manipulate the tautomeric state of individual molecule that can potentially be used as a single molecule switch. Since the yield is dependent on the molecular energy levels, various strategies can be employed to tune these properties from its derivatives which can eventually modify the switching behavior. Further, graphene proves to be a useful substrate to observe these phenomena, possibly due to weaker substrate-molecule coupling compared to metals.

The interaction of strong p-dopant molecule F_4TCNQ is quite different than H_2TPP. The F_4TCNQ molecules adsorb as single molecules avoiding any closed pack assembly. Due to their strong electrophillic nature, the molecules are sensitive to the periodic electronic properties of moiré superstructure. On graphene moiré these molecules selectively adsorb in an intermediate site. In the STS measurements, we find energy states very close to the Fermi level which possibly arise from the splitting of the LUMO into SOMO and SUMO states of the molecule. By increasing the molecular coverage, we find that molecular condense into linear chains and also being sensitive to the moiré regions. However, in this 1D phase, the STS shows sharp resonance peaks in negative bias that can be explained as the charging of the LUMO state, in the double barrier tunneling model. Consequently, it appears that the LUMO has been pushed higher in energy in the linear stacking. This demonstrates that the electronic properties of F_4TCNQ are strongly affected by their local environment . These measurements help to understand the parameters that influence the intrinsic properties of molecules.

We have studied the surface properties of black phosphorus to gain insights into its electronic properties. On surface, we find dumble shaped defect structures (peanut defects) and they have been characterized by STM and STS. We find that the apparent shape as well as the contrast of the peanut defect changes contrast with polarity. These findings are the first reports for this material. Through STS measurements, it is observed that these defects have electronic features almost 1 eV below the Fermi level. On the surface, there exists a point type meta-stable defect which is different than a peanut defect, in terms of shape as well as STS. These point defects can be irreversibly transformed into a peanut defect by applying a voltage pulse around 4.2 V. The origin and the atomic structure of these defects are poorly understood and still an active area of research. From our experiments, we find common features in different types of defects which helps us understand the intrinsic properties of black phosphorus. We do emphasize that these results require complementary input from other measurement techniques. For example, functionalized non-contact atomic force microscopy can help resolve the atomic arrangement around the defects.

The effects of ambient exposure on the surface modification of black phosphorus has also

been investigated. From measurements with upto 30 minutes of exposure, we still find intact rows of P-atoms along with some dark adsorbates throughout the surface of the crystal. This suggests that degradation of black phosphorus is not as dramatic as often predicted. Since the surface is relatively smooth and any mobile adsorbates can be removed by gentle annealing (upto 120∘ C), it is possible to make photoemission measurements like ARPES that can identify the modification in its band structure due to ambient exposure.

Further, we functionalize black phosphorus with F_4TCNQ molecules and study the substrate-molecule interactions. Comparing the energy levels of gas phase F_4TCNQ with band structure of black phosphorus, we find that the LUMO is deeper than the valence band edge which can lead to increased charge transfer to the molecule. The single molecules that are adsorbed on black phosphorus have been found to be quite stable. An interesting finding from this system has been the charging of the molecules by voltage pulse form the tip. We observe that the molecules are charged by the excitation from the STM tip and become mobile on the surface. The nature of charge on the molecule is understood by the attraction towards the positive polarity on the tip. It is well known the F_4TCNQ (and TCNQ) can exist in stable anionic forms in the presence of donor entities. Here, we expect the same behavior with black phosphorus being the donor. Eventually we find some of the charged or activated molecules to relax back to the neutral state but mostly they are in this charged state.

Bibliography

[1] Wallace, P. R. The band theory of graphite. *Phys. Rev.* **71**, 622–634 (1947).

[2] Geim, A. K. & Novoselov, K. S. The rise of graphene. *Nature Materials* **6**, 183 (2007).

[3] Allen, M. J., Tung, V. C. & Kaner, R. B. Honeycomb carbon: A review of graphene. *Chem. Rev.* **110**, 132–145 (2010).

[4] Gupta, A., Sakthivel, T. & Seal, S. Recent development in 2d materials beyond graphene. *Progress in Materials Science* **73**, 44 – 126 (2015).

[5] Song, X., Hu, J. & Zeng, H. Two-dimensional semiconductors: recent progress and future perspectives. *J. Mater. Chem. C* **1**, 2952–2969 (2013).

[6] Miró, P., Audiffred, M. & Heine, T. An atlas of two dimensional materials. *Chem. Soc. Rev.* **43**, 6537–6554 (2014).

[7] Bhimanapati, G. R. *et al.* Recent advances in two-dimensional materials beyond graphene. *ACS Nano* **9**, 11509–11539 (2015). PMID: 26544756.

[8] Mak, K. F., Lee, C., Hone, J., Shan, J. & Heinz, T. F. Atomically thin mos_2: A new direct-gap semiconductor. *Phys. Rev. Lett.* **105**, 136805 (2010).

[9] Gong, C. *et al.* Electronic and optoelectronic applications based on 2d novel anisotropic transition metal dichalcogenides. *Adv. Sci.* **4**, 1700231 (2019).

[10] Ling, X., Wang, H., Huang, S., Xia, F. & Dresselhaus, M. S. The renaissance of black phosphorus. *Proceedings of the National Academy of Sciences* (2015).

[11] Tran, V., Soklaski, R., Liang, Y. & Yang, L. Layer-controlled band gap and anisotropic excitons in few-layer black phosphorus. *Phys. Rev. B* **89**, 235319 (2014).

[12] Mannix, A. J. *et al.* Synthesis of borophenes: Anisotropic, two-dimensional boron polymorphs. *Science* **350**, 1513–1516 (2015).

[13] Matusalem, F., Koda, D. S., Bechstedt, F., Marques, M. & Teles, L. K. Deposition of topological silicene, germanene and stanene on graphene-covered sic substrates. *Scientific Reports* **7**, 15700 (2017).

[14] Deng, J. *et al.* Epitaxial growth of ultraflat stanene with topological band inversion. *Nature Materials* **17**, 1081–1086 (2018).

[15] Zhao, J. *et al.* Rise of silicene: A competitive 2d material. *Progress in Materials Science* **83**, 24 – 151 (2016).

[16] Dean, C. R. *et al.* Boron nitride substrates for high-quality graphene electronics. *Nature Nanotechnology* **5**, 722 (2010).

[17] Zhang, J., Chen, Y. & Wang, X. Two-dimensional covalent carbon nitride nanosheets: synthesis, functionalization, and applications. *Energy Environ. Sci* **8**, 3092–3108 (2015).

[18] Kalantar-zadeh, K. *et al.* Two dimensional and layered transition metal oxides. *Applied Materials Today* **5**, 73 – 89 (2016).

[19] Ko, M., Mendecki, L. & Mirica, K. A. Conductive two-dimensional metal–organic frameworks as multifunctional materials. *Chem. Commun.* **54**, 7873–7891 (2018).

[20] Jin, E. *et al.* Two-dimensional sp2 carbon–conjugated covalent organic frameworks. *Science* **357**, 673–676 (2017).

[21] Tan, C. *et al.* Recent advances in ultrathin two-dimensional nanomaterials. *Chemical Reviews* **117**, 6225–6331 (2017). PMID: 28306244.

[22] Duong, D. L., Yun, S. J. & Lee, Y. H. van der waals layered materials: Opportunities and challenges. *ACS Nano* **11**, 11803–11830 (2017).

[23] Wang, F. *et al.* 2d library beyond graphene and transition metal dichalcogenides: a focus on photodetection. *Chem. Soc. Rev.* **47**, 6296–6341 (2018).

[24] Wang, X., Song, J. & Qu, J. Antimonene: From experimental preparation to practical application. *Angew. Chem. Int. Ed.* **58**, 1574–1584 (2019).

[25] Britnell, L. *et al.* Electron tunneling through ultrathin boron nitride crystalline barriers. *Nano Letters* **12**, 1707–1710 (2012). PMID: 22380756.

[26] Liu, H. *et al.* Phosphorene: An unexplored 2d semiconductor with a high hole mobility. *ACS Nano* **8**, 4033–4041 (2014). PMID: 24655084.

[27] Wilson, J. & Yoffe, A. The transition metal dichalcogenides discussion and interpretation of the observed optical, electrical and structural properties. *Advances in Physics* **18**, 193–335 (1969).

[28] Chhowalla, M. *et al.* The chemistry of two-dimensional layered transition metal dichalcogenide nanosheets. *Nature Chemistry* **5**, 263 (2013).

[29] Ba, K. *et al.* Chemical and bandgap engineering in monolayer hexagonal boron nitride. *Scientific Reports* **7**, 45584 (2017).

[30] Xu, Y. & Liu, J. Graphene as transparent electrodes: Fabrication and new emerging applications. *Small* **12**, 1400–1419 (2016).

[31] Koh, W. S., Gan, C. H., Phua, W. K., Akimov, Y. A. & Bai, P. The potential of graphene as an ito replacement in organic solar cells: An optical perspective. *IEEE Journal of Selected Topics in Quantum Electronics* **20**, 36–42 (2014).

[32] Geim, A. K. & Grigorieva, I. V. Van der waals heterostructures. *Nature* **499**, 419 (2013).

[33] Cheng, R. *et al.* Electroluminescence and photocurrent generation from atomically sharp wse2/mos2 heterojunction p-n diodes. *Nano Lett.* **14**, 5590–5597 (2014).

[34] Wang, F. *et al.* Tunable gate-mos2 van der waals p-n junctions with novel optoelectronic performance. *Nano Lett.* **15**, 7558–7566 (2015).

[35] Liu, X. *et al.* Ultrahigh vacuum self-assembly of rotationally commensurate c8-btbt/mos2/graphene mixed-dimensional heterostructures. *Chem. Mater.* **31**, 1761–1766 (2019).

[36] Deng, Y. *et al.* Black phosphorus-monolayer mos2 van der waals heterojunction p-n diode. *ACS Nano* **8**, 8292–8299 (2014).

[37] Amet, F. *et al.* Tunneling spectroscopy of graphene-boron-nitride heterostructures. *Phys. Rev. B* **85**, 073405 (2012).

[38] Mishchenko, A. *et al.* Twist-controlled resonant tunnelling in graphene/boron nitride/graphene heterostructures. *Nature Nanotechnology* **9**, 808 (2014).

[39] Britnell, L. *et al.* Field-effect tunneling transistor based on vertical graphene heterostructures. *Science* **335**, 947–950 (2012).

[40] Georgiou, T. *et al.* Vertical field-effect transistor based on graphene-ws2 heterostructures for flexible and transparent electronics. *Nature Nanotechnology* **8**, 100 (2012).

[41] Lee, K.-C. *et al.* Analog circuit applications based on all-2d ambipolar rese2 field-effect transistors. *Adv. Funct. Mater.* **29**, 1809011 (2019).

[42] Britnell, L. *et al.* Strong light-matter interactions in heterostructures of atomically thin films. *Science* **340**, 1311–1314 (2013).

[43] Withers, F. *et al.* Light-emitting diodes by band-structure engineering in van der waals heterostructures. *Nature Materials* **14**, 301 (2015).

[44] Parzefall, M. *et al.* Light from van der waals quantum tunneling devices. *Nature Communications* **10**, 292 (2019).

[45] Binder, J. *et al.* Upconverted electroluminescence via auger scattering of interlayer excitons in van der waals heterostructures. *Nature Communications* **10**, 2335 (2019).

[46] Roy, K. *et al.* Graphene-mos2 hybrid structures for multifunctional photoresponsive memory devices. *Nature Nanotechnology* **8**, 826 (2013).

[47] Wang, J., Mu, X., Sun, M. & Mu, T. Optoelectronic properties and applications of graphene-based hybrid nanomaterials and van der waals heterostructures. *Applied Materials Today* **16**, 1 – 20 (2019).

[48] Vikraman, D. *et al.* Fabrication of mos2/wse2 heterostructures as electrocatalyst for enhanced hydrogen evolution reaction. *Applied Surface Science* **480**, 611 – 620 (2019).

[49] Mao, S. *et al.* Two-dimensional nanomaterial-based field-effect transistors for chemical and biological sensing. *Chem. Soc. Rev.* **46**, 6872–6904 (2017).

[50] Meng, Z., Stolz, R. M., Mendecki, L. & Mirica, K. A. Electrically-transduced chemical sensors based on two-dimensional nanomaterials. *Chemical Reviews* **119**, 478–598 (2019).

[51] Panchakarla, L. S. *et al.* Synthesis, structure, and properties of boron- and nitrogen-doped graphene. *Adv. Mater.* **21**, 4726–4730 (2009).

[52] Ci, L. *et al.* Atomic layers of hybridized boron nitride and graphene domains. *Nature Materials* **9**, 430 (2010).

[53] Lv, R. & Terrones, M. Towards new graphene materials: Doped graphene sheets and nanoribbons. *Materials Letters* **78**, 209 – 218 (2012). 30th Anniversary Special Issue.

[54] Zhang, S. J. *et al.* Opening the band gap of graphene through silicon doping for the improved performance of graphene/gaas heterojunction solar cells. *Nanoscale* **8**, 226–232 (2016).

[55] Suvansinpan, N. *et al.* Substitutionally doped phosphorene: electronic properties and gas sensing. *Nanotechnology* **27**, 065708 (2016).

[56] Rigosi, A. F., Hill, H. M., Rim, K. T., Flynn, G. W. & Heinz, T. F. Electronic band gaps and exciton binding energies in monolayer $Mo_xW_{1-x}S_2$ transition metal dichalcogenide alloys probed by scanning tunneling and optical spectroscopy. *Phys. Rev. B* **94**, 075440 (2016).

[57] Elias, D. C. *et al.* Control of graphene's properties by reversible hydrogenation: Evidence for graphane. *Science* **323**, 610–613 (2009).

[58] Karlický, F., Kumara Ramanatha Datta, K., Otyepka, M. & Zbořil, R. Halogenated graphenes: Rapidly growing family of graphene derivatives. *ACS Nano* **7**, 6434–6464 (2013).

[59] Karlický, F. *et al.* Adsorption of organic molecules to van der waals materials: Comparison of fluorographene and fluorographite with graphene and graphite. *Journal of Chemical Theory and Computation* **13**, 1328–1340 (2017). PMID: 28145699.

[60] Arra, S., Ramya, K. R., Babar, R. & Kabir, M. Photocatalytic activity of phosphorene derivatives: Coverage, electronic, optical, and excitonic properties. *J. Phys. Chem. C* **122**, 7194–7202 (2018).

[61] Daukiya, L. *et al.* Covalent functionalization by cycloaddition reactions of pristine defect-free graphene. *ACS Nano* **11**, 627–634 (2017). PMID: 28027437.

[62] Tang, C. W. Two-layer organic photovoltaic cell. *Applied Physics Letters* **48**, 183–185 (1986).

[63] Koezuka, H., Tsumura, A. & Ando, T. Field-effect transistor with polythiophene thin film. *Synthetic Metals* **18**, 699 – 704 (1987). Proceedings of the International Conference of Science and Technology of Synthetic Metals.

[64] Burroughes, J. H. *et al.* Light-emitting diodes based on conjugated polymers. *Nature* **347**, 539–541 (1990).

[65] Peisert, H. *et al.* Full characterization of the interface between the organic semiconductor copper phthalocyanine and gold. *Journal of Applied Physics* **91**, 4872–4878 (2002).

[66] Ohtani, H., Wilson, R. J., Chiang, S. & Mate, C. M. Scanning tunneling microscopy observations of benzene molecules on the rh(111)-(3by3) (c6h6 and 2co) surface. *Phys. Rev. Lett.* **60**, 2398–2401 (1988).

[67] Lippel, P. H., Wilson, R. J., Miller, M. D., Wöll, C. & Chiang, S. High-resolution imaging of copper-phthalocyanine by scanning-tunneling microscopy. *Phys. Rev. Lett.* **62**, 171–174 (1989).

[68] Möller, R., Coenen, R., Esslinger, A. & Koslowski, B. The topography of isolated molecules of copper–phthalocyanine adsorbed on gaas(110). *Journal of Vacuum Science & Technology A* **8**, 659–660 (1990).

[69] Kanai, M. *et al.* Scanning tunneling microscopy observation of copper-phthalocyanine molecules on si(100) and si(111) surfaces. *Surface Science* **329**, L619 – L623 (1995).

[70] Chiang, S. Scanning tunneling microscopy imaging of small adsorbed molecules on metal surfaces in an ultrahigh vacuum environment. *Chem. Rev.* **97**, 1083–1096 (1997).

[71] Strohmaier, R., Petersen, J., Gompf, B. & Eisenmenger, W. A systematic stm study of planar aromatic molecules on inorganic substrates: I. submolecular image contrast. *Surface Science* **418**, 91 – 104 (1998).

[72] Repp, J., Meyer, G., Stojković, S. M., Gourdon, A. & Joachim, C. Molecules on insulating films: Scanning-tunneling microscopy imaging of individual molecular orbitals. *Phys. Rev. Lett.* **94**, 026803 (2005).

[73] Wang, Q. H. & Hersam, M. C. Room-temperature molecular-resolution characterization of self-assembled organic monolayers on epitaxial graphene. *Nature Chemistry* **1**, 206 (2009).

[74] Pollard, A. J. *et al.* Supramolecular assemblies formed on an epitaxial graphene superstructure. *Angewandte Chemie International Edition* **49**, 1794–1799 (2010).

[75] Cho, J. *et al.* Structural and electronic decoupling of c60 from epitaxial graphene on sic. *Nano Lett.* **12**, 3018–3024 (2012).

[76] Barja, S. *et al.* Self-organization of electron acceptor molecules on graphene. *Chem. Commun.* **46**, 8198–8200 (2010).

[77] Lauffer, P., Emtsev, K. V., Graupner, R., Seyller, T. & Ley, L. Molecular and electronic structure of ptcda on bilayer graphene on sic(0001) studied with scanning tunneling microscopy. *Phys. Status Solidi B* **245**, 2064–2067 (2008).

[78] Kumar, A. *et al.* Charge-transfer-driven nonplanar adsorption of f4tcnq molecules on epitaxial graphene. *ACS Nano* **11**, 4960–4968 (2017). PMID: 28467831.

[79] Tsai, H.-Z. *et al.* Molecular self-assembly in a poorly screened environment: F4tcnq on graphene/bn. *ACS Nano* **9**, 12168–12173 (2015).

[80] Abellán, G. *et al.* Noncovalent functionalization of black phosphorus. *Angew. Chem. Int. Ed.* **55**, 14557–14562 (2016).

[81] Wang, C. *et al.* Charge transfer at the ptcda/black phosphorus interface. *The Journal of Physical Chemistry C* **121**, 18084–18094 (2017).

[82] Wang, C. *et al.* Electronic structures at the interface between cupc and black phosphorus. *The Journal of Chemical Physics* **147**, 064702 (2017).

[83] Wang, C. *et al.* Energy level evolution and oxygen exposure of fullerene/black phosphorus interface. *J. Phys. Chem. Lett.* **9**, 5254–5261 (2018).

[84] Wang, C. *et al.* Interface energy-level alignment between black phosphorus and f16cupc molecular films. *J. Phys. Chem. C* **123**, 10443–10450 (2019).

[85] He, Y., Xia, F., Shao, Z., Zhao, J. & Jie, J. Surface charge transfer doping of monolayer phosphorene via molecular adsorption. *The Journal of Physical Chemistry Letters* **6**, 4701–4710 (2015). PMID: 26545168.

[86] Cavaleiro, J. A. S. *et al.* Porphyrin derivatives: Synthesis and potential applications. *Journal of Heterocyclic Chemistry* **37**, 527–534 (2000).

[87] Roger Guilard, K. S., Karl Kadish (ed.) *The Porphyrin Handbook* (Academic Press, 2000), 1-20 edn.

[88] Cárdenas-Jirón, G., Borges-Martínez, M., Mera-Adasme, R. & Pino-Rios, R. Quantum chemical studies of porphyrin- and expanded porphyrin-based systems and their potential applications in nanoscience. latin america research review. *Int J Quantum Chem* **119**, e25821 (2019).

[89] Jurow, M., Schuckman, A. E., Batteas, J. D. & Drain, C. M. Porphyrins as molecular electronic components of functional devices. *Coordination Chemistry Reviews* **254**, 2297 – 2310 (2010). Supramolecular approaches to nano and molecular electronics.

[90] Boyle, N. M., Rochford, J. & Pryce, M. T. Thienyl—appended porphyrins: Synthesis, photophysical and electrochemical properties, and their applications. *Coordination Chemistry Reviews* **254**, 77 – 102 (2010).

[91] Merz, K. M. & Reynolds, C. H. Tautomerism in free base porphyrins: the porphyrin potential energy surface. *J. Chem. Soc., Chem. Commun.* 90–92 (1988).

[92] Pham, V. D. *et al.* Electronic interaction between nitrogen-doped graphene and porphyrin molecules. *ACS Nano* **8**, 9403–9409 (2014). PMID: 25187965.

[93] Liljeroth, P., Repp, J. & Meyer, G. Current-induced hydrogen tautomerization and conductance switching of naphthalocyanine molecules. *Science* **317**, 1203–1206 (2007).

[94] Liljeroth, P. Flipping a single proton switch. *Nature Nanotechnology* **7**, 5 (2011).

[95] Kügel, J., Sixta, A., Böhme, M., Krönlein, A. & Bode, M. Breaking Degeneracy of Tautomerization-Metastability from Days to Seconds. *ACS Nano* **10**, 11058–11065 (2016).

[96] Kügel, J., Klein, L., Leisegang, M. & Bode, M. Analyzing and Tuning the Energetic Landscape of H2Pc Tautomerization. *Journal of Physical Chemistry C* **121**, 28204–28210 (2017).

[97] Kügel, J. *et al.* Remote single-molecule switching: Identification and nanoengineering of hot electron-induced tautomerization. *Nano Letters* **17**, 5106–5112 (2017).

[98] Dou, K. P. & Kaun, C. C. Conductance switching of a phthalocyanine molecule on an insulating surface. *Frontiers of Physics* **12**, 10–13 (2017).

[99] Schaffert, J. *et al.* Imaging the dynamics of individually adsorbed molecules. *Nature Materials* **12**, 223 (2012).

[100] Krönlein, A., Kügel, J., Kokh, K. A., Tereshchenko, O. E. & Bode, M. Energetic and Spatial Mapping of Resonant Electronic Excitations. *Journal of Physical Chemistry C* **120**, 13843–13849 (2016).

[101] Ladenthin, J. N. *et al.* Hot carrier-induced tautomerization within a single porphycene molecule on cu(111). *ACS Nano* **9**, 7287–7295 (2015). PMID: 26057840.

[102] Novko, D., Tremblay, J. C. & Blanco-Rey, M. On the tautomerisation of porphycene on copper (111): Finding the subtle balance between van der Waals interactions and hybridisation. *Journal of Chemical Physics* **145** (2016).

[103] Böckmann, H. *et al.* Direct observation of photoinduced tautomerization in single molecules at a metal surface. *Nano Letters* **16**, 1034–1041 (2016). PMID: 26796945.

[104] Novko, D., Blanco-Rey, M. & Tremblay, J. C. Intermode coupling drives the irreversible tautomerization in porphycene on copper(111) induced by scanning tunnelling microscopy. *The Journal of Physical Chemistry Letters* **8**, 1053–1059 (2017). PMID: 28198627.

[105] Böckmann, H. *et al.* Near-Field Enhanced Photochemistry of Single Molecules in a Scanning Tunneling Microscope Junction. *Nano Letters* **18**, 152–157 (2018).

[106] Kumagai, T. *et al.* Thermally and vibrationally induced tautomerization of single porphycene molecules on a cu(110) surface. *Phys. Rev. Lett.* **111**, 246101 (2013).

[107] Kumagai, T. *et al.* Controlling intramolecular hydrogen transfer in a porphycene molecule with single atoms or molecules located nearby. *Nature Chemistry* **6**, 41 (2014).

[108] Ladenthin, J. N. *et al.* Force-induced tautomerization in a single molecule. *Nature Chemistry* **8**, 935 (2016).

[109] Pham, V. D. *et al.* Tuning the electronic and dynamical properties of a molecule by atom trapping chemistry. *ACS Nano* **11**, 10742–10749 (2017). PMID: 28960959.

[110] Ferraris, J., Cowan, D. O., Walatka, V. & Perlstein, J. H. Electron transfer in a new highly conducting donor-acceptor complex. *J. Am. Chem. Soc.* **95**, 948–949 (1973).

[111] Epstein, A. J., Etemad, S., Garito, A. F. & Heeger, A. J. Metal-insulator transition and antiferromagnetism in a one-dimensional organic solid. *Phys. Rev. B* **5**, 952–977 (1972).

[112] Coleman, L. B. *et al.* Superconducting fluctuations and the peierls instability in an organic solid. *Solid State Communications* **12**, 1125–1132 (1973).

[113] Ma, L. *et al.* Single photon triggered dianion formation in tcnq and f4tcnq crystals. *Scientific Reports* **6**, 28510 (2016).

[114] Abrahams, B. F., Elliott, R. W., Hudson, T. A., Robson, R. & Sutton, A. L. X4tcnq2 dianions versatile building blocks for supramolecular systems. *CrystEngComm* **20**, 3131–3152 (2018).

[115] Chen, W., Chen, S., Qi, D. C., Gao, X. Y. & Wee, A. T. S. Surface transfer p-type doping of epitaxial graphene. *Journal of the American Chemical Society* **129**, 10418–10422 (2007). PMID: 17665912.

[116] Tian, X., Xu, J. & Wang, X. Band gap opening of bilayer graphene by f4-tcnq molecular doping and externally applied electric field. *The Journal of Physical Chemistry B* **114**, 11377–11381 (2010). PMID: 20690622.

[117] Yang, S., Jiang, Y., Li, S. & Liu, W. Many-body dispersion effects on the binding of tcnq and f4-tcnq with graphene. *Carbon* **111**, 513 – 518 (2017).

[118] Javadi, N., Najafi, M. & Yourdkhani, S. On the role of substituent in noncovalent functionalization of graphene and organophosphor recognition: Iqa and sapt perspective. *Int J Quantum Chem* **117**, e25379 (2017).

[119] Pham, V. D. *et al.* Selective control of molecule charge state on graphene using tip-induced electric field and nitrogen doping. *npj 2D Materials and Applications* **3**, 5 (2019).

[120] Stradi, D. *et al.* Controlling the spatial arrangement of organic magnetic anions adsorbed on epitaxial graphene on ru(0001). *Nanoscale* **6**, 15271–15279 (2014).

[121] Han, X., Han, J., Liu, C. & Sun, J. Promise and challenge of phosphorus in science, technology, and application. *Adv. Funct. Mater.* **28**, 1803471 (2018).

[122] Zhang, S. *et al.* Extraordinary photoluminescence and strong temperature/angle-dependent raman responses in few-layer phosphorene. *ACS Nano* **8**, 9590–9596 (2014). PMID: 25188827.

[123] Castellanos-Gomez, A. *et al.* Isolation and characterization of few-layer black phosphorus. *2D Materials* **1**, 025001 (2014).

[124] Castellanos-Gomez, A. Black phosphorus: Narrow gap, wide applications. *The Journal of Physical Chemistry Letters* **6**, 4280–4291 (2015). PMID: 26600394.

[125] Li, L. *et al.* Direct observation of the layer-dependent electronic structure in phosphorene. *Nature Nanotechnology* **12**, 21 (2016).

[126] Hultgren, R., Gingrich, N. S. & Warren, B. E. The atomic distribution in red and black phosphorus and the crystal structure of black phosphorus. *J. Chem. Phys.* **3**, 351–355 (1935).

[127] Shirotani, I. Growth of large single crystals of black phosphorus at high pressures and temperatures, and its electrical properties. *Molecular Crystals and Liquid Crystals* **86**, 203–211 (1982).

[128] Zhang, J. L. *et al.* Epitaxial growth of single layer blue phosphorus: A new phase of two-dimensional phosphorus. *Nano Lett.* **16**, 4903–4908 (2016).

[129] Qiu, Z. *et al.* Resolving the spatial structures of bound hole states in black phosphorus. *Nano Letters* **17**, 6935–6940 (2017). PMID: 29035538.

[130] Kiraly, B., Hauptmann, N., Rudenko, A. N., Katsnelson, M. I. & Khajetoorians, A. A. Probing single vacancies in black phosphorus at the atomic level. *Nano Letters* **17**, 3607–3612 (2017). PMID: 28481547.

[131] Ospina, D. A., Duque, C. A., Mora-Ramos, M. E. & Correa, J. D. Theoretical study of phosphorene multilayers: optical properties and small organic molecule physisorption. *Journal of Materials Science* **53**, 5103–5113 (2018).

[132] Du, L. *et al.* Novel electronic structures and enhanced optical properties of boron phosphide/blue phosphorene and f4tcnq/blue phosphorene heterostructures: a dft + negf study. *Phys. Chem. Chem. Phys.* **20**, 28777–28785 (2018).

[133] Aspect, A. & Villain, J. The birth of wave mechanics (1923-1926). *Comptes Rendus Physique* **18**, 583–585 (2017).

[134] Binnig, G., Rohrer, H., Gerber, C. & Weibel, E. Surface studies by scanning tunneling microscopy. *PRL* **49**, 57–61 (1982).

[135] Bardeen, J. Tunnelling from a many-particle point of view. *PRL* **6**, 57–59 (1961).

[136] Joucken, F. *et al.* Localized state and charge transfer in nitrogen-doped graphene. *Phys. Rev. B* **85**, 161408 (2012).

[137] Pham, V. D. *et al.* Control of Molecule-Metal Interaction by Hydrogen Manipulation in an Organic Molecule. *Journal of Physical Chemistry Letters* **7**, 1416–1421 (2016).

[138] Lewis, J. P. *et al.* Advances and applications in the fireball ab initio tight-binding molecular-dynamics formalism. *Phys. Status Solidi B* **248**, 1989–2007 (2011).

[139] MAITY, D. K. & TRUONG, T. N. Status of theoretical modeling of tautomerization in free-base porphyrin. *Journal of Porphyrins and Phthalocyanines* **05**, 289–299 (2001).

[140] Lv, R. *et al.* Nitrogen-doped graphene: beyond single substitution and enhanced molecular sensing. *Scientific Reports* **2**, 586 (2012).

[141] de Oliveira, I. S. S. & Miwa, R. H. Organic molecules deposited on graphene: A computational investigation of self-assembly and electronic structure. *The Journal of Chemical Physics* **142**, 044301 (2015).

[142] Pavliček, N., Swart, I., Niedenführ, J., Meyer, G. & Repp, J. Symmetry dependence of vibration-assisted tunneling. *Physical review letters* **110**, 136101 (2013).

[143] Zhang, Y. *et al.* Enhanced performance of perovskite solar cells with p3ht hole-transporting materials via molecular p-type doping. *RSC Adv.* **6**, 108888–108895 (2016).

[144] Uchida, K., Furuya, S., Iwata, J.-I. & Oshiyama, A. Atomic corrugation and electron localization due to moiré patterns in twisted bilayer graphenes. *Phys. Rev B* **90**, 155451 (2014).

[145] Wu, S. W., Nazin, G. V., Chen, X., Qiu, X. H. & Ho, W. Control of relative tunneling rates in single molecule bipolar electron transport. *Phys. Rev. Lett.* **93**, 236802 (2004).

[146] Bridgman, P. W. Two new modifications of phosphorus. *Journal of the American Chemical Society* **36**, 1344–1363 (1914).

[147] Yau, S.-L., Moffat, T. P., Bard, A. J., Zhang, Z. & Lerner, M. M. Stm of the (010) surface of orthorhombic phosphorus. *Chemical Physics Letters* **198**, 383 – 388 (1992).

[148] Zhang, C. D. *et al.* Surface structures of black phosphorus investigated with scanning tunneling microscopy. *The Journal of Physical Chemistry C* **113**, 18823–18826 (2009).

[149] Liang, L. *et al.* Electronic bandgap and edge reconstruction in phosphorene materials. *Nano Letters* **14**, 6400–6406 (2014). PMID: 25343376.

[150] Riffle, J. V. *et al.* Impact of vacancies on electronic properties of black phosphorus probed by stm. *Journal of Applied Physics* **123**, 044301 (2018).

[151] Kumar, A. *et al.* Stm study of exfoliated few layer black phosphorus annealed in ultrahigh vacuum. *2D Materials* **6**, 015005 (2019).

[152] Xia, F., Wang, H. & Jia, Y. Rediscovering black phosphorus as an anisotropic layered material for optoelectronics and electronics. *Nature Communications* **5**, 4458 (2014).

[153] Chen, Z. *et al.* Band gap renormalization, carrier multiplication, and stark broadening in photoexcited black phosphorus. *Nano Letters* **19**, 488–493 (2019).

[154] Das, S. *et al.* Tunable transport gap in phosphorene. *Nano Letters* **14**, 5733–5739 (2014). PMID: 25111042.

[155] Kim, J. *et al.* Observation of tunable band gap and anisotropic dirac semimetal state in black phosphorus. *Science* **349**, 723–726 (2015).

[156] Villegas, C. E. P., Rocha, A. R. & Marini, A. Anomalous temperature dependence of the band gap in black phosphorus. *Nano Lett.* **16**, 5095–5101 (2016).

[157] Han, C. Q. *et al.* Electronic structure of black phosphorus studied by angle-resolved photoemission spectroscopy. *Phys. Rev. B* **90**, 085101 (2014).

[158] Reinert, F. & Nicolay, G. Influence of the herringbone reconstruction on the surface electronic structure of au(111). *Applied Physics A* **78**, 817–821 (2004).

[159] Edmonds, M. T. *et al.* Creating a stable oxide at the surface of black phosphorus. *ACS Applied Materials & Interfaces* **7**, 14557–14562 (2015). PMID: 26126232.

[160] Pei, J. *et al.* Producing air-stable monolayers of phosphorene and their defect engineering. *Nature Communications* **7**, 10450 (2016).

[161] Plutnar, J., Sofer, Z. & Pumera, M. Products of degradation of black phosphorus in protic solvents. *ACS Nano* **12**, 8390–8396 (2018). PMID: 30106272.

[162] Kuntz, K. L. *et al.* Control of surface and edge oxidation on phosphorene. *ACS Applied Materials & Interfaces* **9**, 9126–9135 (2017). PMID: 28218508.

[163] Huang, Y. *et al.* Interaction of black phosphorus with oxygen and water. *Chemistry of Materials* **28**, 8330–8339 (2016).

[164] Zhang, R., Li, B. & Yang, J. A first-principles study on electron donor and acceptor molecules adsorbed on phosphorene. *The Journal of Physical Chemistry C* **119**, 2871–2878 (2015).